Mapping the surface water storage variation in densely impounded semi-arid NE Brazil with satellite remote sensing approach

A Dissertation

Submitted in Partial Fulfilment of the Requirements for the Degree of Doctor of Natural Sciences (Dr. rer. nat.)

to the Department of Earth Sciences

of Freie Universität Berlin

by

Shuping Zhang

Berlin, July 2018

Supervisor: Prof. Dr. Björn Waske

Second examiner: Prof. Dr. Axel Bronstert

Date of defense: November 14th, 2018

Abstract

Surface water bodies provide vital support to the society and fundamentally affect ecosystems in various manners. Precise knowledge of the spatial extent of surface water bodies (e.g. reservoirs) as well as of the quantity of water they store is necessary for efficient water deployment and understanding of the local hydrology. Remote sensing provides broad opportunities for surface water mapping. The main objectives of this thesis are: 1) delineating surface water area of partly vegetated water bodies only from remote sensing data without field data input; 2) obtaining the surface water storage, and 3) analyzing its spatio-temporal variations for northeastern (NE) Brazil as a representative for a densely dammed semi-arid region.

At first, I investigated the potential of digital elevation models (DEMs) generated from TanDEM-X data, which were acquired during the low water level stage, for reservoirs' bathymetry derivation. I found that the accuracy of such DEMs can reach one meter, both in the absolute and relative respects. It has shown that DEMs derived from TanDEM-X data have great potentials for representing the reservoirs' bathymetry of temporally dried-out reservoirs.

Subsequently, I targeted at developing a method for mapping the water surface beneath canopy independent of field data for further delineation of the effective water surface. Instead of the commonly used backscattering coefficients, I investigated the capability of the Gray-Level Co-Occurrence Matrix (GLCM) texture index to distinguish different types of Radar backscattering taking place in (partly) vegetated reservoirs. This experiment demonstrated that different types of backscattering at the vegetated water surface show distinct statistical characteristics on GLCM variance derived from TerraSAR-X satellite time series data. Furthermore, with the threshold established based on the statistics of the sub-populations dominated by different types of backscattering, the vegetated water surfaces were effectively mapped, and the effective water surface areas were further delineated with an accuracy of 77% to 95%.

Based on the investigation of the DEMs generated from TanDEM-X data, I derived the formerly unknown bathymetry for 2 105 reservoirs of various sizes in four representative regions of an overall area of 10 000 km^2. The spatial distributions of surface water storage capacities in the four regions were subsequently extracted from the combination of the reservoir bathymetry and the water surface extents provided by RapidEye satellite time series. Furthermore, the spatio-temporal variations of surface water storage were derived for the four representative regions on an annual basis in the period of 2009-2017. This study showed that 1) The density of reservoirs in NE Brazil amounts to 0.04-0.23 reservoirs per km^2, the corresponding water surface and surface water storage are 1.18-4.13 ha/km^2 and 0.01-0.04 hm^3 m/km^2, respectively; 2) On the spatial unit of 5×5 km^2, the surface water storage in the region constantly decreased due to a prolonged drought with a rate of 10^5 m^3/year from 2009 to 2017, with a slight increase from 2016 to 2017 in a few reservoirs; 3) Local precipitation deficit controls the variation of the overall surface water storage in the region. In this thesis I demonstrated the great potential of the great potential of SAR and optical satellite time series data for hydrological applications. The method I developed for delineating the effective water extent from the vegetated reservoirs has shown high potential transferability for other similar regions. The data gaps of bathymetry and surface waters storage capacity were filled for 2 105 reservoirs in NE Brazil. The results of the spatio-temporal variations of surface water storage in four representative regions from 2009-2016 can support future water management and improve hydrological prediction in NE Brazil.

Zusammenfassung

Oberflächengewässer haben einen hohen Wert für die Gesellschaft und beeinflussen Ökosysteme grundlegend und in verschiedenster Weise. Kenntnisse der genauen Ausdehnung der Wasseroberfläche und des Volumens der Gewässer (z.B. von Stauseen) sind wichtig für eine effiziente Wassernutzung sowie für das Verständnis der lokalen Hydrologie. Für die Kartierung von Oberflächengewässern bietet die Fernerkundung sehr gute Möglichkeiten. Die Hauptziele dieser Dissertation sind 1) die Bestimmung der Wasserflächenausdehnung von teilweise mit Vegetation bedeckten Gewässern unter ausschließlicher Nutzung fernerkundlicher Daten ohne lokal erfasste Beobachtungen, 2) die Ableitung der Gewässervolumina, sowie 3) die Analyse ihrer raumzeitlichen Variation am Beispiel vom semi-ariden Nordostbrasilien, das eine hohe Dichte an Stauseen aufweist.

Zunächst untersuchte ich das Potenzial von aus TanDEM-X-Daten erstellten digitalen Geländemodellen (DGM) für die Ableitung der Bathymetrie von Stauseen. Solche DGMs können eine Genauigkeit von bis zu einem Meter erreichen, sowohl absolut als auch relativ. Die aus den TanDEM-X-Daten während der Niedrigwasserperiode abgeleiteten DGMs haben damit ein großes Potenzial für die zuverlässige Abbildung der Bathymetrie von zeitweilig trocken fallenden Stauseen.

Anschließend entwickelte ich eine Methode zur Kartierung der effektiven Gewässerflächenausdehnung von teilweise vegetationsbedeckten Stauseen unabhängig von Felddaten. Anstelle der häufig verwendeten Streuungskoeffizienten untersuchte ich die Eignung des Grauwertematrix (GLCM)-Texturindexes zur Unterscheidung zwischen verschiedenen Arten der Radarsignalstreuung, die bei bewachsenen Stauseen auftreten. Dieses Experiment verdeutlichte, dass unterschiedliches Streuverhalten der bewachsenen Wasseroberfläche eindeutige statistische Merkmale der GLCM-Varianz in TerraSAR-X Satellitenzeitreihendaten aufweist. Desweiteren wurden mittels Schwellwerten, die basierend auf statistischen Kennwerten für jede Art von Rückstreuverhalten festgesetzt wurden, die bewachsene Gewässerfläche kartiert und die effektive Ausdehnung der Wasseroberfläche mit

einer Genauigkeit von 77 bis 95% bestimmt.

Basierend auf dem von TanDEM-X-Daten abgeleiteten DGM habe ich für 2 105 Stauseen unterschiedlicher Größe in vier repräsentativen Regionen mit einer Gesamtfläche von 10 000 km^2 die bislang weitestgehend unbekannte Bathymetrie abgeleitet. Mit Hilfe der Wasserflächen, die aus RapidEye-Zeitreihen bestimmt wurden, und der genannten Bathymetrien wurde die räumliche Verteilung der Speicherkapazitäten in Stauseen in den vier Regionen berechnet. Weiterhin wurden raum-zeitliche Variationen der Wasservolumina für die vier repräsentativen Regionen jährlich für den Zeitraum 2009-2017 analysiert. So konnte gezeigt werden, dass 1) die Dichte an Stauseen in Nordostbrasilien bei 0,04-0,023 Stauseen pro km^2 liegt, mit einer entsprechenden Wasserfläche von 1,18-4,13 ha/km^2 und einem Wasservolumen von 0,01-0,04 hm^3 m/km^2; 2) dass bei einer räumlichen Auflösung von 5×5 km^2 in den Jahren durch eine langanhaltende Dürre gekennzeichneten Jahren 2009-2017 das Wasservolumen in der Region kontinuierlich gesunken ist mit einer Rate von 10^5 m^3/Jahr mit einer leichten Zunahme von 2016 bis 2017 in wenigen Stauseen; 3) dass ein lokales Niederschlagsdefizit die Variation des gesamten Oberflächenwasservolumens in der Region kontrolliert. In trockenen Jahren beschleunigte die Wasserentnahme aus großen Stauseen die Wasserverluste in diesen Gewässern.

In dieser Dissertation habe ich das Potenzial von SAR- und optischen Satellitendatenzeitreihen für hydrologische Anwendungen aufgezeigt. Die Methode, die ich zur Kartierung der Gewässerfläche von teilweise vegetationsbedeckten Stauseen entwickelt habe, ist potentiell übertragbar auf andere ähnliche Regionen. Die Bathymetrie und die Speicherkapazitäten für 2 105 Stauseen schließen eine Datenlücke für die untersuchten Regionen in Nordostbrasilien. Die abgeleitete raum-zeitliche Variation des Wasservolumens kann zukünftig das Wassermanagement unterstützen und die hydrologische Modellierung und Vorhersage in Nordostbrasilien verbessern.

Table of Contents

List of Figures

List of Tables

List of Abbreviations

DEM	Digital elevatiom model
Radar	radio direction and ranging
SAR	synthetic aperture radar
InSAR	Interferometric synthetic aperture radar
TDX DEM	TanDEM-X derived DEM
LiDAR	air borne light detection and ranging
DGPS	Differential global positioning system
COSSC	co-registered single look slang range complex
HoA	height of ambiguity
SRTM DEM	Shuttle Radar Topography Mission DEM
ICESat	Ice, Cloud,and land Elevation Satellite
GLAS 14	Geoscience Laser Altimetry System 14
NSIDC	National Snow and Ice Data Center
DNs	digital numbers
SNR	signal noise ratio
MCF	minimum cost flow
TSX	TerraSAR-X
EEC	Enhanced Ellipsoid Corrected
dB	decibel
GLCM	Gray-Level Co-Occurrence Matrix
TRMM	Tropical Rainfall Measuring Mission
SR	specular reflection
DB	double bounces
MB	Multiple bounces
VS	volumetric scattering
PCA	Principal component analysis
DOY	Day of year
LAI	Leaf area index
GLDAS	Global Land Data Assimilation System
GRACE	Gravity Recovery and Climate Experiment
NDVI	normalized differential vegetaion index
NDWI	normalized differential water index
mNDWI	Modified normalized differential water index

1. Introduction

1.1 Motivation

Surface water bodies, including lakes, reservoirs, wetland, flood plains, river etc. provide vital support to the society and the ecosystem, affect local hydrology, and interact with local/global climate. They supply water for domestic use, power generation, and agricultural irrigation (Postel, 2000). From ecological perspective, surface water maintaining the local ecosystem and ecological habitats. Water bodies of large number/density also interfere the local hydrological transportation by changing the volume and time of rivers discharge to the oceans (Biemans et al., 2011). By altering the green house emission (Rosenqvist et al., 2002), changing the transporting pathway and varying the amount of carbon and nitrogen in the hydrological systems (Bastviken et al., 2011; Tranvik et al., 2009), water bodies like reservoirs pose subtle impact on the climate. Water bodies like lakes in semi-arid area are very sensitive to climate condition, and their variation also indicate the climate change.

Knowledge on precise water surface and storage in water scarce area can improve the efficiency of local water management. This knowledge also helps to understanding the local and regional hydrology and its response to human activities like damming etc. Moreover, in regions characterized by water redundancy or deficit, e.g. flooding or droughts, precise information on water surface area and storage on real time scale can assist analyzing, predicting and preventing water related hazards, and help to study the interaction between surface water, climate condition and human interferences (Alsdorf and Lettenmaier, 2003; Koltun, 2001).

1.2 State of art in surface water mapping with remote sensing

Remote sensing images acquired by ground-, air- and space- borne instruments capture the physical characteristic of ground objects of vast distribution. Given traditional in-situ water body monitoring is labor- and time-costly, remote sensing data have provided broad opportunities for studying water bodies of difficult access and/or wide spread. Along with the increases in the temporal spatial and spectral resolutions, the ease in access, and the variety of

remote sensing data, the application of remote sensing data and relevant approaches in water body mapping have developed significantly (Lettenmaier et al., 2015; Palmer et al., 2015). As a matter of fact, water environment mapping has entered a new era when remote sensing data and techniques provide the mainstream approaches (Alsdorf et al., 2007; Hall et al., 2011; Lettenmaier et al., 2015; Palmer et al., 2015; Van Dijk and Renzullo, 2011).

Water mapping is based on the characteristics of water environment captured by the remote sensing images. The data commonly used for surface water mapping were provided by sensors capturing the ground reflected solar light in the range of visible, infrared and microwave windows (Figure 1.1).

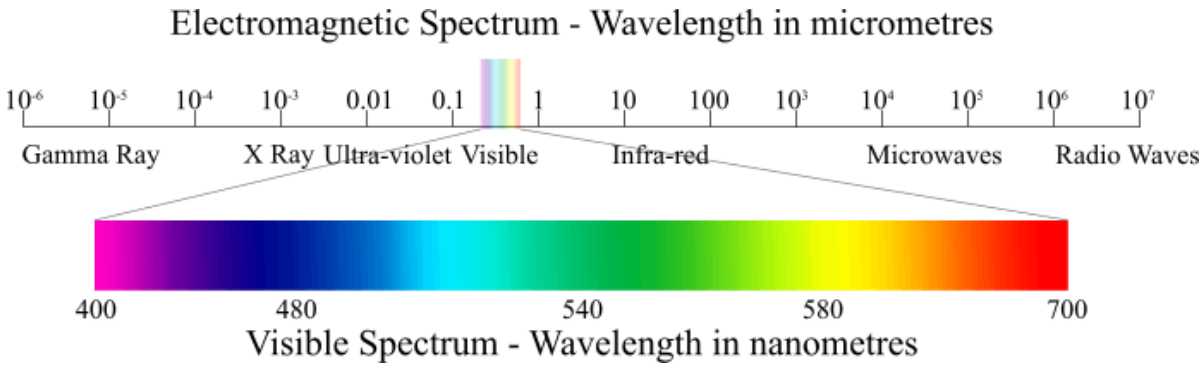

Figure 1.1 The electromagnetic spectrum, image courtesy http://www.sat.dundee.ac.uk/spectrum.html

1.2.1 Physical characteristics of water environment in remote sensing data and relevant technique

Images acquired by optical sensor receiving solar light in visible and infrared range and the images acquired with instrument receiving microwave signals are the commonly used data in current remote sensing mapping. Therefore, in this study I mainly focused on investigating the data acquired by optical sensors and microwave instruments for precise mapping of water surface and surface water storage.

1.2.1.1 Water environment on Radar images

Microwave imagers map the ground surface with the received microwave pulses whose wavelengths are on the order of centimeter to decimeter (Figure 1.1). A radio direction and ranging (Radar) sensor is an active system which transmits microwave pulses towards the

targets and receives the returned signals. Thus, mapping with Radar instruments is independent of external illumination, for example from the sun. A SAR system synthesizes the effect of a very long antenna from a single antenna, using the Doppler effect caused by the motion of the platform which the SAR antenna mounts (Lillesand et al., 2008). SAR sensor usually provide images of much higher spatial resolution than real aperture radars which constrained by the length of the antenna.

Microwave pulses transmitted by a radar system can penetrate through the clouds, smoke and haze. Therefore, the image acquisition with Radar sensors can take place at all weather conditions (Ulaby and Long, 2014). Radar systems are side-looking system (Figure 1.2). The backward reflection of the incident Radar pulses is called backscattering. The brightness of a Radar image indicates the amplitude of pulses returned by ground objects. The amplitude of a SAR image depends on the dielectric constant of the ground objects and the geometric relation between the incident Radar pulses and the ground objects (Cover and Chris Oliver, 2004). Usually, ground objects of large dielectric constants return more energy than that of small dielectric constant. The amplitude component of Radar image is often converted to backscattering coefficient for further mapping and analysis. In addition to the backscattering amplitude, a Radar system also records the distance between the antennae and the mapped ground objects by measuring the time of the returned signals (Lillesand et al., 2007). The antenna–ground distance is recorded as the phase component of SAR data and expressed as the times of the microwave's wavelength.

The microwave pulses transmitted by a Radar sensor travel in the panel normal to the ground surface, and this panel is called incidence panel. The geometrical relation between the incidence panel and the panel along which the electric field vectors are distributed determines the polarization of the microwave. A wave is horizontally polarized (also known as perpendicularly polarized and denoted with H) if its electrical vector is perpendicular to the incidence panel and vertically polarized (parallel polarized and denoted with V) if its electric field vector is distributed in the incidence panel (Ulaby and Long, 2014). Radar pulses are often

transmitted and received in single, dual or quadratic channels.

Figure 1.2 illustrates the interaction between the transmitted Radar signals and mapped water environment. Three types of scattering take place on a vegetated water surface: specular reflection, diffusive/volumetric scattering and double bounces, with their backscattering amplitudes in the ascending order (Cohen et al., 2016; Ferrazzoli and Guerriero, 1995; Horritt et al., 2003; Ormsby et al., 1985; Ramsey, 1995). Open water surface presents specular reflection (SR) and barely returns any transmitted signals to the Radar sensors. On the water surface vegetated by tree or features alike, the incident Radar pulses are reflected away from the open water surface towards the tree trunk or similar features, and then returned to the antenna with little attenuation. This process is so-called double bounces (Richards et al., 1987) and allows for high backscattering from the water surfaces vegetated by plants like tree and large emergent macrophytes (Hess et al., 1990; Richards et al., 1987). Volumetric scattering (VS) takes place on the rough surfaces covered by plants of dense or closed canopy, for instance, floating macrophytes.

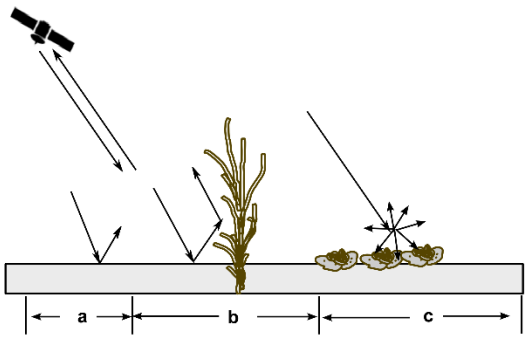

Figure 1.2 The interaction between surface water environment with transmitted SAR pulses. a: specular reflection; b: double bounces, and c: diffusive/volumetric scattering

1.2.1.2 InSAR technique

Interferometric SAR (InSAR) is a recent technique in the remote sensing domain which employs SAR images pairwise and requires the image pair to map the same area with nearly identical configurations (Bamler and Hartl, 1998; Rosen et al., 2000). Instead of the amplitude

component, InSAR uses the phase component of SAR images (Bamler and Hartl, 1998; Rosen et al., 2000) (Figure 1.3 A).

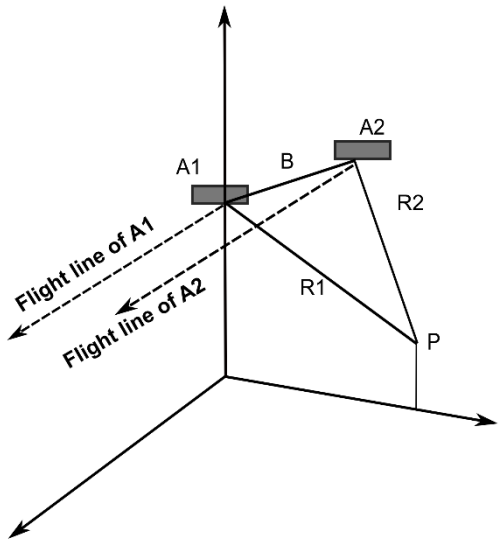

Figure 1.3 Illustration of an InSAR system, after Lillesand et al. (2008). A1 and A2 indicate the platforms of the SAR sensors. B is the distance between the two sensors, R1 is the distance between the sensor on A1 and the ground object P, so is the relation between R2, A2 and P. The two sensors on A1 and A2 can map the ground surface simultaneously or with time lag of days

The phase component of a SAR image expresses the distance between SAR sensors and the mapped ground objects in the cycle of 2π. Usually, the phase is wrapped, and only shows the fractional components in the range of $-\pi$ to π. It is later recovered to the complete cycles of 2π with a processing called unwrapping (Rosen et al., 2000) to express the phase difference between adjacent pixels or the phase difference at the same location caused by ground displacements. The wrapped phase (ϕ) comprises of the phase contribution from the topography of the mapped area (ϕ_{topo}), atmospheric inconsistency in the signal paths in the two acquisitions (ϕ_{atm}), and orbital inaccuracy of the involved sensors (ϕ_{orb}) and noise (ϕ_{noise}) as shown in equation (1.1) (Bamler and Hartl, 1998; M.Kampes, 2006; Rosen et al., 2000):

$$\phi = \phi_{topo} + \phi_{dis} + \phi_{atm} + \phi_{orb} + \phi_{noise} \tag{1.1}$$

Among all the components, the mostly frequently adopted ones are the phased of the

topography and ground displacement. DEMs can be generated from those SAR image pair by converting the topography phase to the elevation with height of ambiguity (HoA) defined in equation (1.2) (E et al., 2004; Small, 1998; Wegmüller et al., 2009):

$$HoA = \frac{R_d \lambda sin\theta}{2B_\perp} \Delta\varphi \tag{1.2}$$

Where HoA is the height of ambiguity, indicating the height of the ground corresponding to the phase difference $\Delta\varphi$; λ is the wavelength of SAR pulses, θ is the incidence angle; R_d is the distance between the mapped ground and the sensors; $B_\perp$ is the distance between the two sensors in the direction perpendicular to the path of SAR pulses.

In the case of surface deformation, e.g. earthquake, the displacement component is explicitly extracted and converted to the surface motion magnitude with displace ambiguity defined in equation *(1.3)* (Bamler and Hartl, 1998; M.Kampes, 2006; Rosen et al., 2000)

$$\Delta D = -\frac{4\pi}{\lambda} \Delta\varphi \tag{1.3}$$

ΔD is the displacement of the ground, and $\Delta\varphi$ is the difference between the phases contained in the image pair mapping the same area.

InSAR requires the signals from the pair of the image be consistent at the local scale. The signal consistency is indicated by coherence (γ), expressed as the local correlation coefficient as defined with equation (1.4) (Bamler and Hartl, 1998; Rosen et al., 2000):

$$\gamma = \frac{< g_1 \, g_2{}^* >}{\sqrt{< |g_1|^2 >< |g_2|^2 >}} \tag{1.4}$$

Where g_1 is the SAR signal returned to the i^{th} antenna, and angular brackets represent the averaging over the window where the coherence is calculated. The ground objects which return identical SAR pulses to the SAR sensors will present coherence $\gamma = 1$, and the objects which fails to return similar pulses to the two sensors will present $\gamma = 0$ (Rosen et al., 2000) The

quality of an interferogram is determined by the coherence derived from the image pairs used to generated the interferogram.

In a water environment, open water surface usually does not return (consistent) SAR pulse to the sensors, and present coherence nearly 0. However, in the water surface vegetated by woody plants or large emergent macrophyte, the double bounces between the water surface and the tree trunks or similar features return strong and consistent SAR pulses back to the SAR sensors thus present highly coherent. The ground displacement in equation (1.1)in this circumstance is caused by the water level changes beneath the canopy (Alsdorf et al., 2000).

1.2.1.3 Water environment on optical spectral images

Optical sensors map the earth surface by capturing the visible and infrared solar light reflected from the ground objects. In the light of wavelength in the range of 0.4-2.6 μm, clear open water shows distinct spectrum in comparison to other objects (Figure 1.1). The majority of the light in the range of 0.4-0.7μm which is transmitted to the open water surface is absorbed, and very minimal proportion of it is reflected (Curran., 1985) (Figure 1.4). Open water absorbs nearly all of the near infrared (0.7-1.3 μm) and middle infrared (1.3-3.0 μm) light transmitted to it. In thermal infrared light, water presents dark. In contrast, green vegetation and soil reflect more visible, near infrared and middle infrared light transmitted toward them (Figure 1.4). Green plants present low reflectance in the visible light. The reflectance from green vegetation significantly increases in the light of wavelength approximately 700 nm (red edge) (Weichelt et al., 2014), and remain high in the near infrared light (Figure 1.4). Due to the strong absorption of water in the vegetation (Szekielda, 1988), the reflectance from green vegetation decreases in middle infrared light. The absorption of green leaves is positively related to the water content in the vegetation and basal soil. The reflectance of soil and similar round object increases along with the wavelength of the transmitted light in the range of 0.4-3.0 μm (Figure 1.4).

Atmospheric components (e.g. water vapor) whose molecule diameters are on the order of the wavelength of optical light interfere the transmitting of the energy and alter the signals travel

toward the optical sensors. Therefore, atmospheric correction is a very critical step in remote sensing mapping with optical images (Gholizadeh et al., 2016; Lillesand et al., 2008). Similarly, clouds, smoke and haze are additional factors that undermine the applicability of optical images in terms of temporal continuity and spatial coverage.

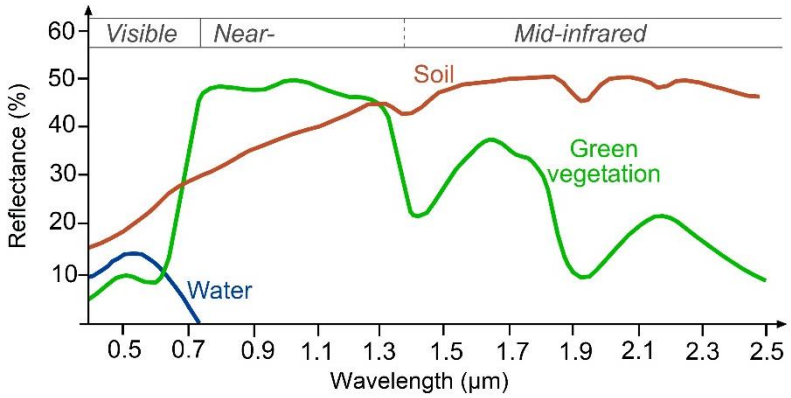

Figure 1.4 The optical spectrum of water environment, after Hoffer (1978).

1.2.2 Missions and instruments

The data used for ground objects mapping can be provided by mapping instruments mounted on ground-, air-, and space-platforms. However, this study only focuses on images acquired by space-borne sensors, because space-borne data are acquired on routine schedules and operational plans, while ground and airborne data are obtained mostly for experimental purposes and constrained to specific sites.

1.2.2.1 SAR missions

Table 1.1 lists the main satellite SAR systems employed in water environment mapping.

Table 1.1 Space-borne SAR missions that provide commonly used data for surface water environment mapping

Mission	Operator	Operation period	Wavelength	Resolution	Polarization	Revisit
ERS-1& 2	ESA	1991-2011	C-	30 m	HH	35 d
ENVISAT	ESA	2002-2008	C-	30 m	HH	35 d
RadarSat 1&2	CAS	1995- present	C-	30 m	HH	24d
JERS -1 &2	JAXA	1992-1999	L-	26 m	HH	44d
TerraSAR-X/ TanDEM-X	DLR	2011-present	X-	1.5/3/6m	HH, VV, HH-VV	11d
COSMO-SkyMed	ASI	2007-present	X-	5 m	HH	1-15 d
Sentinel-1(A & B)	ESA	2014-present	C-	10/	HH, VV-VH	6-12d

TanDEM-X is a novel mission conceived to generate global DEM of high accuracy and resolution with InSAR technique. The global TanDEM-X DEMs are expected to be of resolution of 12 m, and accuracy of 10 m and 2 m, for absolute and relative, respectively (Fritz, 2012; Wessel et al., 2018). The data used for the mission ware acquired in bistatic cooperation mode. During the data acquisition mode, the X- band SAR sensors mounting on two nearly identical satellites simultaneously receive the echoes of SAR signals transmitted to the ground by one of these satellites (Bamler and Hartl, 1998). As the two satellites fly less than one kilometer apart, the signal paths are nearly identical, which emilinates the chance for the phase controbution of atmospheric heterogeneity. The simultaneous mapping with the two satellites does not allow for any contribution of ground deformation in the interferogram in equation (1.1) (Krieger et al., 2007). In the TanDEM-X mission for global DEM generation, the same area on the earth was mapped two to three time with TanDEM-X data acquired, with different satellite flight distances, so as to secure the high accuracy of the final global DEM (Krieger et al., 2007). As open water surface barely returns any SAR signals to the sensors, they often present incoherent in the interferogram. This renders invalid the elevation of the areas covered by open water in any acquisition of the TanDEM-X data mapping the region (TanDEM-X ground segment, 2013).

1.2.2.2 Optical missions

Currently, the widely used optical images for land surface mapping are provided by sensors that map the earth surface with multiple and hyperspectral instruments. The data are determined by

the spectral span they cover and the number of bands of the images. The spectral range of multi-spectral images already cover the water spectrum and the characteristic bands (Figure 1.4) and provide enough spectral information for distinguishing open water surfaces from other ground objects. Therefore, water surface mapping in terms of quantity has engaged mainly multi-spectral images. The most commonly used multi-spectral sensors for water mapping and their satellite platforms are listed in Table 1.2.

Table 1.2 Space-borne optical missions that provide commonly used data for surface water mapping

satellites	Sensors	Operation period	No. band	Wavelength range	Resolution	Revisit
NOAA/TIROS	AVHRR	1978–present	5	0.58 - 12.50 µm	1 km/0.5km	1 d
Terra	MODIS	1999- present	36	0.44 -14.4 µm	200/500/1000 m	1-2 d
Landsat (1-8)	MSS	1972–1993	4-6	0.500 – 1.0 µm 0.450 – 2. 35 µm	60	16 d
	TM	1982–1999	8	0.45 - 2.35 µm	30/15m	
	ETM	1993–present	8	0.435 - 12.51 µm	30/15m	
	OLI	2015- present	11	0.433-12.5µm	30/15m/100m	
CBERS-1/2	CCD	1999-present	5	0.510 – 0.890 µm	80/120m	26 d
TERRA	ASTER	1999-present	15	0.2-11.65 µm	15/30/90m	16 d
IKONOS	Pan/MSI	1999-present	4	0.440 – 0.900 µm	1/4m	3 d
RapidEye	Multispectral	2008-present	5	0.440 – 0.850 µm	5 m	5 d
SPOT	Pan/MS/SWI Multispectral	1986-present	5	0.450 – 0.890 m	5/10/20m	1 d
Sentinel-2 (A & B)	MSI	2015-present	13	0.43-2.19 µm	12 m	5 d

1.2.3 Mapping water surface

1.2.3.1 Open water surface

Based on the distinct characteristics of open water presented in the optical spectrum (Figure 1.4), the near infrared bands of optical images have been applied for open water surface mapping. Indices like normalized differential water index (NDWI) (McFeeter, 1996), modified NDWI (MNDWI) (Xu, 2006) and water index (WI) (Ouma and Tateishi, 2006) have been developed, and widely applied to derive water masks on various spatial and temporal scale (Birkett, 2000; Jain et al., 2006; Pekel et al., 2016; Pope et al., 1992; Smith, 1997; Song et al., 2013; Verpoorter et al., 2014; Wolski et al., 2017). With the supports of recent supercomputing

cloud platforms like Google Earth Engine (Gorelick et al., 2017), the change trends of each pixel in open water surface in the decadal span have been depicted with Landsat archive (Donchyts et al., 2016; Pekel et al., 2016).

On a SAR image, the areas occupied by calm open water often present dark due to the specular reflection (Figure 1.2) and can be easily distinguished from other ground objects. Algorithms like Otsu or minimum error algorithm were used to delineate open water surface from SAR images (Kittler and Illingworth, 1986; Otsu, 1979). Based on these algorithms, methods like splitting and segmentation of SAR image were developed for flooding mapping with both the amplitude and backscattering coefficient of SAR image (Martinis et al., 2015; Schlaffer et al., 2015). A number of global water masks have been established from different SAR data sets (Santoro et al., 2015; Westerhoff et al., 2013). Further approaches for open water delineation from SAR image include the automatic method developed by Horritt et al. (2001) and the fast processing algorithms developed by Gstaiger et al. (2012) and Martinis et al. (2015). In addition to backscattering coefficient derived from the amplitude of SAR images, the potential of InSAR coherence for open water surface mapping was demonstrated by Dellepiane et al. (2000a) and Refice et al. (2014), based on the coherence loss over open waters (Alsdorf, 2002; Dellepiane et al., 2000b; Kim et al., 2017). The TanDEM-X mission even yielded a global open water mask based on the InSAR coherence (Wendleder et al., 2013).

Besides, combining SAR data from ERS and optical images from AVHRR, Prigent et al. (2007) and Papa et al., (2010) revealed the inter-annual variability of global surface water on monthly scale from 1993-2004, at the resolution of 25 km^2 and 0.25 degree. Like mapping open water with optical remote sensing data, mapping open water surfaces from SAR images has evolved to the operational level.

1.2.3.2 Water surface beneath canopy

Water is the key constitution of wetland, marshland and mangrove etc., and a large portion of water surfaces there underlies the vegetation canopy. Therefore, in these landscapes open water

often could not express the complete water surface. Using open water surface to represent the inundated area can cause underestimate of the actual water surface (Li et al., 2015b, 2015a). Therefore, mapping the water surface under canopy is another important part of water surface mapping (Alsdorf and Lettenmaier, 2003). Image acquired by both SAR and optical sensors were investigated and applied in mapping the water surface beneath the vegetation canopy.

Since 1990s, massive studies have investigated the performance of different SAR images mapping in large flood plains, coastal wetlands, marsh lands and mangrove (Hess et al., 1990, 1995; Lucas et al., 2007; O'Grady and Leblanc, 2014; Pope et al., 1997; Ramsey, 1995; Wang et al., 1995). Significant findings have been drawn as follows: 1) Three types of scattering take place in vegetated water surfaces, namely, specular reflectance from calm open water, double bounce between the water surface and the trees truck or features alike (Richards et al., 1987), and diffusive/volumetric scattering transmitted SAR impulses on canopy of the dense vegetation (Cohen et al., 2016; Wang et al., 1995); 2) The smaller the incidence angle the SAR pules are transmitted, the stronger the SAR signals ,i.e. higher backscattering, returned are (Lang et al., 2008).The images acquired with incidence angle between 20-50 degree can distinguish the water surface beneath the canopy (Lang et al., 2008); 3) The images acquired with HH-polarization are more efficient than images of VV- polarization in detecting water surface beneath canopy (Hess et al., 1995; Pope et al., 1992; Wedler and Kessler, 1981). SAR pulses of VV- polarization mostly interact with the canopy of the vegetation (Bourgeau-Chavez et al., 2001; Henry et al., 2006; Hess et al., 1995; Lang and Kasischke, 2008; Wang et al., 1995); 4). The penetration depth is positively related to the SAR pulses wavelength. Images acquired in C- and X- band are more suitable for mapping the water surface in herbaceous wetland and marshland. The images acquired in L- band data are more suitable for mapping flood plains which are often covered by woody plants or forests (Hess et al., 1995; Novo et al., 1998); 5) Canopy closure and plant height determine the amplitude of the backscattering from vegetation (Cohen et al., 2016; P. A. Townsend, 2001; Zalite et al., 2013); 6) The backscattering in the non-forested wetlands is negatively related to the water level (Kasischke et al., 2009); 7) In the

wetlands dominated by herbaceous plants, the backscattering is positively related to the moisture of basal soil (Kasischke et al., 2009).

In addition to the above findings, many studies investigated the temporal evolution of the vegetated waters with SAR images. Hydrological cycles on multi-temporal, seasonal and annual frequencies were revealed for flood plains of large rivers like Amazon, Nile and Roanoke River (Hess et al., 2003; P. A. Townsend, 2001; Townsend, 2002; Wilusz et al., 2017) and coastal wetlands in Florida etc. (Kasischke et al., 2003); Betbeder et al. (2015) established that late winter, spring and beginning of summer are the most relevant seasons for mapping the wetland vegetation. With multiple temporal RADARSAT-2 data of full polarimetry, Zhao et al., (2014) mapped the season inundation and vegetation dynamics in a flood plain in northeastern China, and demonstrated the importance of quad-polarimetric information for floodplain monitoring. Wilusz et al. (2017) used the training data from published studies, and classified the flooded forest in Sudd wetland on multiple time stamps.

Similarly, in the mapping of landscape like wetlands and flood plains with optical data which were mainly oriented to mapping the vegetation condition in these landscapes, water surface beneath canopy were also yielded as part of the output (Dronova et al., 2015; Wang et al., 2012; Ward et al., 2014). In addition, models were developed from optical images or by integrating auxiliary data like the Lidar measurements or DEM (Feng et al., 2012; Lang and McCarty, 2009; Rosenqvist et al., 2002), and subsequently applied to obtain the inundation at different times in the same sites (Huang et al., 2014; Jin et al., 2017; O'Connell et al., 2017; Ordoyne and Friedl, 2008). The modelling methods can be transferred to different time stamps, but only for the sites where the mode was established.

SAR and optical images (Table 1.1 and Table 1.2) were often combined to map vegetated waters. For example, Bwangoy et al. (2010a) mapped the wetlands in Congo basin with combined JERS-1 and Landsat data, and proved the usefulness of multi-source data in characterizing wetland land cover. Ward et al., (2014) mapped the seasonal inundation patterns

of Alligator River flood plain by combining ALOS PALSAR and Landsat images. In the inundation mapping with the combination of RadarSat-1 & 2 and SPOT, Toeyrae et al. (2001) found that the SAR data acquired in small incidence angle yield better classification results; Gala and Melesse (2012) proved that the combination of Landsat, Radarsat-1 and Lidar data can improve the mapping results of wet area in prairie.

However, those studies above were conducted mainly with supervised classification approaches with field data as input (Arnesen et al., 2013; Dronova et al., 2015; Hess et al., 1995; Kasischke et al., 2003; Martinez and Letoan, 2007; P. Townsend, 2001; Wang et al., 2012, 1995; Ward et al., 2014);. The methods used include random forest, support vector machine, maximum likelihood or object orientated approaches (Dronova et al., 2015; Kasischke et al., 1997; Wang et al., 2012; Ward et al., 2014). Nearly all these studies employed training data acquired from the field at approximately the same time as the image acquisitions. Often substantial field data are necessary for high credibility of the results. As these flooded landscapes are difficult to access for field data collection or classes identifications, the classification-based inundation mapping is rather labor-expensive and limited to a few time stamps. In addition, a priori classes of landscapes are also required for the classification. Moreover, the water conditions and vegetation status in these landscapes often change along the seasons. Therefore, the prerequisites of field data and a priori classes render the classification-oriented approaches site–specific, training data constrained, and not transferable to other sites or time.

At present, there are few field data independent approaches available for the detection of water surface beneath the canopy along time series. As the green plants on land and in water present similar spectrum on multiple spectral images (Figure 1.4), spectrum based approaches with the assistance of field data often fail to distinguish these two types of vegetation (Toeyrae et al., 2001). However, Carter (1982) suggested that the flood extent can be efficiently detected with optical images acquired during the leaf-off season when the terrestrial plants show less green vegetation spectrum. Therefore, it is possible to map the inundations in wetlands using the vegetation spectrum in optical images (Domenikiotis et al., 2003; Feng et al., 2012; Powell et

al., 2014; Zhao et al., 2011, 2014). However, the gaps in the leaf-on season still remain open, and there is often a latent between the real time water extent and the vegetation response (Powell et al., 2014).

Texture indices derived from SAR images shows the structure properties of ground objects on a SAR image, and were proved to be efficient for mapping urban area which is characterized by double bounces (Ban et al., 2014; Dell'Acqua and Gamba, 2003; Stasolla and Gamba, 2008). Only a few studies have investigated the potential of texture of SAR images for mapping vegetated water surface. Pulvirenti et al. (2011) applied morphological processing on multi-temporal COSMO-SkyMed images to obtain structure elements of the data, and further mapped the inundation evolution at a flooding event concerning water surface beneath canopy. This study demonstrated the potential of texture (structure properties) of SAR images for mapping water surface beneath the canopy without field data.

1.2.3.3 Summary

Overall, mapping global and/or regional open water with remote sensing data has been efficient. Due to the weather independent acquisition and the canopy penetration of the SAR images, it is more efficient to map water surface beneath canopy with SAR data than with optical data. The performance of the SAR data is jointly determined by the data properties (e.g. wavelength, polarization, and incidence angle) and the condition of vegetation (i.e. species, canopy structure, phenology stage) and water (i.e. water depth). Mapping vegetated water surface with the combination of optical and SAR data can yield results of improved accuracies. However, the majority of current methods heavily reply on the field data, thus are site-specific and of low transferability (Bwangoy et al., 2010; Gala and Melesse, 2012; Ward et al., 2014). Therefore, there is a need for methods of high transferability along time and study sites. Moreover, majority of the study engaging SAR data adopted backscattering coefficients of the SAR images. The potential of texture indices for mapping water surface beneath canopy are not adequately investigated.

1.2.4 Surface water storage extraction and bathymetry derivation

Surface water storage is the amount of surface water stored in lakes, river, reservoirs and wetland etc. Surface water storage of these hydrological units can provide important input for the regional water management, hydrological modelling optimization, predicting and warning water related hazards. However, surface water storage is difficult to obtain from remote sensing images, as it usually requires the depth or morphology of the water body which are challenging to obtain. Up to now, studies on deriving the surface water volumetric variation and storage from remote sensing are rather rare, particularly for the latter one (Lettenmaier et al., 2015).

1.2.4.1 Water volumetric variation

Radar altimetry mission were originally designed to monitor the sea level and ice/glacier, by obtaining their surface elevation in point wise measurements distributed along the flight tracks on the ground (Vignudelli et al., 2009; Zwally et al., 2002). However, the altimetry measurement along tracks over inland water can also provide valid surface elevation and reflect the inland water level variations. In addition to the in-situ gauge of water levels, altimetry instruments can also virtually gauge large river and lakes (Birkett, 1998, 1994). For example, water level variations were derived for large rivers from the altimetry measurements from missions like TOPEX/POSEIDON (T/P), ERS-2 ENVISat, and ICESat (Birkett, 1998, 1994; Birkett et al., 2002; da Silva et al., 2010; Hall et al., 2011; Koblinsky et al., 1993; Maillard et al., 2015; Medina et al., 2008; Michailovsky and Bauer-Gottwein, 2014; Morris et al., 1994; Phan et al., 2012; Wang et al., 2013). Furthermore, synergizing the altimetry measurements of water levels and the surface areas derived from optical and/or SAR images can yield the water storage variation in large lakes etc. (Duan and Bastiaanssen, 2013; Frappart et al., 2005; Gao, 2015; Gao et al., 2012; Jiang et al., 2017; Munyaneza et al., 2009; Singh et al., 2012; Song et al., 2014, 2013; Zhang et al., 2006). However, the point-wise altimetry measurements are only reliable when averaged over the entire open water surface. Therefore, the application of altimetry data for water level derivation requires wide open water surface. In addition, the footsteps of altimetry measurement are often on the order of hundred meters to kilometers

(Vignudelli et al., 2009; Zwally et al., 2002). As a result, altimetry measurements often fail to provide water levels for small water bodies, and this fact constrains the application of altimetry data on large water bodies.

Double bounces taking place in the water surface vegetated by woody wetland or flooded forest can return consistent SAR signals to the antenna. Based on this, water level variation in these landscapes can be derived with InSAR from the images mapping the area of interest at different water levels (Alsdorf et al., 2000). Therefore, water level/depth variation in floodplain, wetland/ marsh land and mangrove have been obtained with InSAR from SAR images acquired with different sensors listed in Table 1.1 (Kim et al., 2014, 2009, 2017; Lee et al., 2015; Wdowinski et al., 2008; Xie et al., 2015; Yoon et al., 2013; Yuan et al., 2017). Furthermore, Yuan et al. (2017) intergrated the InSAR derived water levels to estimate the water storage capacity of Congo floodplain. However, for the water level retrieval with InSAR technique, reasonably large area of the water body should be vegetated to produce strong double bounces (Alsdorf et al., 2000). Another shortage of applying InSAR in water level derivation is that InSAR technique can only derive relative water levels. Therefore, attributing the absolute values for the water levels with contemporary altimetry or gauge measurements is necessary. In the case of employing altimetry measurements, wide open water surface should be simultaneously available for credible altimetry measurements (Yuan et al., 2017). As a result, only large wetlands and floodplains meet these requirements.

In addition, integrating water level measurements and surface water area is only capable of estimating partial water volume variation, but not waters storage estimation, as the large water bodies rarely fall empty and become available for mapping the least water status of the landscapes.

1.2.4.2 Mapping bathymetry with remote sensing

Bathymetry can assist estimating the surface water storage. However, obtaining bathymetry in field surveys with acoustic instruments, Lidar sensors and Ground penetrating radars is

labor-costly, particularly when the study is on regional scale and covers a large number of water bodies (Feurer et al., 2008). Various mechanisms and data sets have been investigated to derive bathymetry. Majority of those investigations were conducted in coastal areas, and some of them were experimentally transferred to study inland water bodies (Feurer et al., 2008).

Shallow submarine topography was found to be visible on real aperture radar and SAR images acquired under moderate wind (De Loor and Loor, 1981). Strong tidal currents formed under this weather condition interact with the submarine topography. This varies the currents velocities in return, and further causes modulated local Bragg scatters which determine the sea surface backscatters on SAR images (Alpers and Hennings, 1984). Based on this mechanism, bathymetry have been investigated and successfully mapped for some coastal areas (Alpers and Hennings, 1984; Bell, 1999; Brusch et al., 2011; Vogelzang et al., 1992). However, the application of this mechanism relies on the strong currents in open sea under certain wind condition (wind speed > 3 m/s) (Reichert et al., 1998), and requires some external depth measurements (Brusch et al., 2011). But inland water bodies often could not form strong tides due to the interferences of surrounding terrestrial landscapes. Therefore, this mechanism and its variants are not applicable for the bathymetry derivation for inland water bodies.

The reflectance of coastal substrate in the range of optical spectrum is attenuated by water when the light travels through the water columns (Legleiter et al., 2004; Lyzenga, 1985; Philpot, 1989). The deeper the substrate lies, the longer the travel path of the light is, and the more reflectance is attenuated. Based on this theory, physical and analytical models were constructed to derive water depth and subsequently the bathymetry (Legleiter and Roberts, 2009)(Lee et al., 1999; Lyzenga, 1985; Philpot, 1989). Those models and their variants have been applied on multispectral (e.g. Landsat) and hyperspectral images (e.g. Hyperion) to primarily derive bathymetry for coastal waters (Ayana et al., 2015; Brando et al., 2009; Dekker et al., 2011; Lee et al., 2007; Pacheco et al., 2015; Sandidge and Holyer, 1998). However, those model-based methods for bathymetry retrievals prefer clear water (Pacheco et al., 2015), and are often constrained to shallow waters (< 20 m), as the reflectance of substrate situated deeper than that

are very likely completely absorbed by the water column. Moreover, the presence of vegetation and sun glint are the crucial factors that impede the application of these methods (Feurer et al., 2008).

Because inland waters are usually of higher turbidity than coastal waters turbid, due to the frequent recharge, discharge and human disturbance, and of high chances being vegetated. These substrate optics based approaches do not show high applicability in inland water bodies (Feurer et al., 2008). However, Sneed and Hamilton, (2007) adapted the physical model which was originally constructed by Philpot (1989) for coastal waters, derived water depth and the water volume for the super glacier lakes in Greenland on multi-temporal scale using ASTER. Their study were followed by Williamson et al., (2017) developed a fast algorithm for such study using MODIS data. Their studies addressed the importance of sediments absence in the water and the homogeneous substrate (Sneed and Hamilton, 2007; Williamson et al., 2017). In addition, the water depths derived for the super glacier lakes are less than 10 meters. Moreover, the potentials of the optical spectrum of river bed for the stream bathymetry derivation were also investigated (Legleiter et al., 2004; Legleiter and Overstreet, 2012; Legleiter and Roberts, 2009, 2005). It was found that deriving bathymetry for rivers from optical images (mainly hyperspectral data) is feasible, but the accuracy of the estimated depth is affected by the channel morphology and the spatial resolution of the optical images adopted (Legleiter and Roberts, 2005). On average, the bathymetry derived for rivers with gravel base are approximately at one meter (Legleiter and Overstreet, 2012), with maximal depth at five meters (Legleiter and Overstreet, 2012).

Other studies on the inland lake bathymetry recovery include attributing elevations to lake contours derived from MODIS images at different levels, and interpolated those isoclines to the lake bathymetry (Feng et al., 2011). But this approach requires existing elevation/depth measurements of the lake bottom at least along a few transactions to attribute the water extents yielded from the image data. In addition, the water surface areas should be delineated with high accuracy. However, in many inland water bodies, the vegetation covers a reasonably large area

of the water surface, purely adopting open water can caused underestimated water surfaces.

1.2.4.3 DEMs representing bathymetry and assisting surface water body storage estimation

As the bathymetry of a water body is determined by the substrate morphology, the DEM covering under water topography can represent lake/reservoir bathymetry, and subsequently assist estimating the surface water storage. For example, Avisse et al. (2017) assumed inaccessible lakes in Syria were empty during the acquisition of SRTM DEM in February 2002, and obtained the water level-area-volume relations for these water bodies with this DEM. Based on these water level-area-volume relations and the water surfaces provided by Landsat images mapping areas in the last 30 years, they further derived the surface water storage in these water bodies on temporal scale (Avisse et al., 2017). However, this application works under the condition that the water bodies were empty during the mission of SRTM DEM in 2002. Furthermore, assuming the surrounding topography is determinant to lakes' bathymetry, Messager et al. (2016) built up statistic models from the surrounding topography on SRTM DEM and the geometries of the water bodies, and estimated the water storage in the global natural lakes. However, the water bodies they studied are limited to the natural lakes of size > 10 km^2. Moreover, the storage functions they derived for small water bodies are overall of poor accuracies (Messager et al., 2016).

1.2.4.4 Potentials of single-pass TanDEM-X for reservoir bathymetry derivation and surface water storage extraction

In addition to the global DEM generation, the data acquired by the TanDEM-X constellations were used to generate DEM with single-pass interferometry, and applied for biomass estimation (Schlund et al., 2013), volcanos variation investigation (Kubanek et al., 2015; Rossi et al., 2016), and rice paddies mapping (Rossi and Erten, 2015) etc. The high qualities of such DEMs and the prominent performance of their applications have demonstrated the capability of such-derived DEMs in morphological representation (Kubanek et al., 2015; Rossi et al., 2016; Rossi and Erten, 2015; Schlund et al., 2015), and also suggested their great potentials for

deriving bathymetry for reservoirs of various size and large number.

1.3 Study area

Among the global dryland, NE Brazil is a typical example of regions suffering from long-term water scarcity, poor water management, vulnerable water supply and inadequately knowledge on regional hydrology.

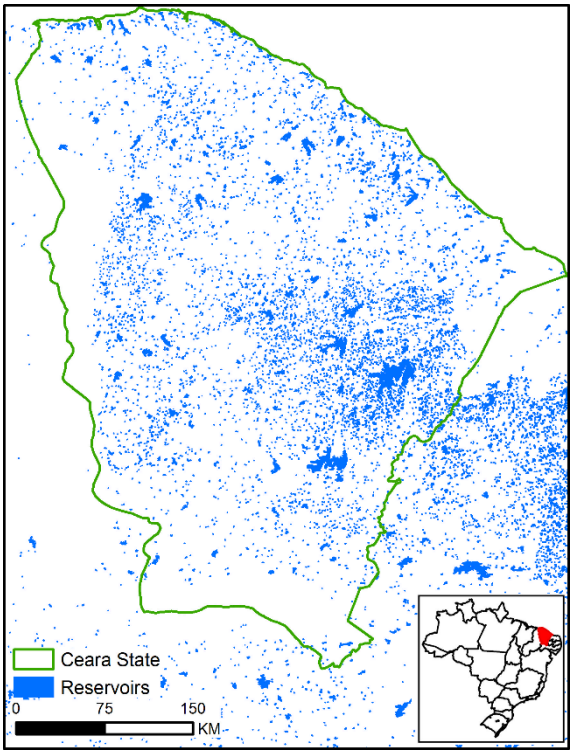

Figure 1.5 The location and the reservoir distributions in NE Brazil

The climate in NE Brazil is characterized with pronounced wet and dry seasons. Most of the precipitation takes place from January to June, indicating this time period as the wet season; the dry season spans from July to December. The average annual precipitation is approx. 600 mm, and the potential evapotranspiration exceeds 2000 mm per annum (INMET, 2018). Since the 19th century, over 30 000 reservoirs have been constructed in NE Brazil to support the local water supply (SIRH/Ce, 2015) (Figure 1.5). Overall, about 100 large reservoirs in this region undergo regular in-situ monitoring (SIRH/Ce, 2015). In contrast, a large number of small to medium reservoirs and those at remote areas are poorly managed and most of them do not have

any inventory data (SIRH/Ce, 2015). Meanwhile, poor management results in severe eutrophication in the reservoirs, and many of them are vastly covered by various macrophytes. Despite the large number of reservoirs, the region is vulnerable to frequent droughts. Up to now, the surface water storage and its variation characteristics in this region are still little-known. However, this knowledge is critical for effective water management and understanding regional hydrology.

1.4 Objectives

As summarized above, water mapping with remote sensing data has evolved from 2D (i.e. water surface) to 3D (i.e. water depth and storage/volume). The temporal scale of water mapping has developed from a few timestamps to continuous time series. Simultaneously, the spatial scale of mapped water bodies expanded from discrete test sites to regional, continental and global scale. The complexity of mapped surface waters bodies has developed from open water surface to the vegetated waters. However, the major gaps in the available surface water mapping still exist and lie in transferable methods for the mapping of water surface beneath canopy and in the delineation of surface water storage.

In this thesis, I worked both on the mapping of water surface beneath canopy and water storage extraction. I chose NE Brazil as the study area, as it represents the regions suffering from long-term water scarcity, poor water management, vulnerable water supply and inadequately knowledge on regional hydrological characteristics. Moreover, many reservoirs were vastly covered by macrophytes, forming large water surface beneath the canopy.

This thesis aimed to investigate the above two aspects by following the guidance of the following research questions:

Based on the performance of TanDEM-X data for global DEM, is it possible to derive the reservoirs bathymetry with the DEM generated from TanDEM-X data acquired during the low water level? If yes, how is the performance of the data set in this aspect?

Is it possible to distinguish the different types of backscattering on the SAR images without

field data? If yes, can this help map vegetated water surface in reservoirs in a training data independent approach which can be transferred in different area and time?

Integrating the answers to the above two questions, how is the surface water storage distributed spatially in the region? How does the surface water storage vary along time? Is there any factors affecting the surface water storage distribution in NE Brazil?

1.5 Research outline

The above questions were answered in the following three studies:

The DEMs generated from single-pass TanDEM-X data were investigated for their potentials for reservoir bathymetry derivation. In this study, I found that the accuracies of such DEMs over the test site Madalena region can achieve one meter, both in the absolute and relative respects. The DEMs derived from the TanDEM-X data acquired during low water level stage have high potentials for representing the reservoirs bathymetry. (It is Chapter 2 and published as: ***Shuping Zhang*** *et al, 2016. Bathymetric survey of water reservoirs in north-eastern Brazil based on TanDEM-X satellite data. Science of the Total Environment, 571, pp. 575-593*)

Subsequently, I used time series of TerraSAR-X (TSX) data from 2014-2015 to investigate the capability of GLCM texture of distinguishing the different types of backscattering taking places in nine vegetated reservoirs in the Madalena catchment. This study demonstrated that different types of backscattering in the vegetated water surface show distinct statistical characteristics on GLCM variance of SAR images. In addition, I derived the abundance of individual types of backscattering in each reservoir with linear unmixing on a temporal scale. Furthermore, the water surfaces beneath vegetation were delineated by segmenting different types of backscattering, independent of field data. The accuracies of the delineated water surfaces are 77%-95%. (It is Chapter 3 and published as: ***Shuping Zhang*** *et al. (2018): Effective water surface mapping in macrophyte-covered reservoirs in NE Brazil based on TerraSAR-X time series. International Journal of Applied Earth Observation and Geoinformation, 69, pp. 41-55)*

In the last part of the thesis, with the DEMs generated from the TanDEM-X data acquired in

October-December 2015, I derived the bathymetry for 2 105 reservoirs of various sizes in four representative regions covering an overall area of 10 000 km^2. Based on this bathymetry data, I extracted the spatial distributions of surface water storage capacities in the four regions. Furthermore, the spatio-temporal variations of surface water storages in the four regions were revealed and analyzed on annual frequency in the period of 2009-2017. (It is Chapter 4, ***Shuping Zhang*** *et al. The spatial-temporal variation of surface water storage in reservoirs in NE Brazil using remote sensing approaches. Submitted to Remote Sensing of Environment*).

2. Bathymetric survey of water reservoirs in northeastern Brazil based on TanDEM-X satellite data

Abstract: Water scarcity in the dry season is a vital problem in dryland regions such as northeastern Brazil. Water supplies in these areas often come from numerous reservoirs of various sizes. However, inventory data for these reservoirs is often limited due to the expense and time required for their acquisition via field surveys, particularly in remote areas. Remote sensing techniques provide a valuable alternative to conventional reservoir bathymetric surveys for water resource management.

In this study single pass TanDEM-X data acquired in bistatic mode were used to generate digital elevation models (DEMs) in the Madalena catchment, northeastern Brazil. Validation with differential global positioning system (DGPS) data from field measurements indicated an absolute elevation accuracy of approximately one meter for the TanDEM-X derived DEMs (TDX DEMs). The DEMs derived from TanDEM-X data acquired at low water levels show significant advantages over bathymetric maps derived from field survey, particularly with regard to coverage, evenly distributed measurements and replication of reservoir shape. Furthermore, by mapping the dry reservoir bottoms with TanDEM-X data, TDX DEMs are free of emergent and submerged macrophytes, independent of water depth (e.g. >10 m), water quality and even weather conditions. Thus, the method is superior to other existing bathymetric mapping approaches, particularly for inland water bodies. The proposed approach relies on (nearly) dry reservoir conditions at times of image acquisition and is thus restricted to areas that show considerable water levels variations. However, comparisons between TDX DEM and the bathymetric map derived from field surveys show that the amount of water retained during the dry phase has only marginal impact on the total water volume derivation from TDX DEM. Overall, DEMs generated from bistatic TanDEM-X data acquired in low water periods constitute a useful and efficient data source for deriving reservoir bathymetry and show great potential in large scale application.

Keywords: Bathymetric mapping, TanDEM-X, semiarid area, northeastern Brazil

2.1 Introduction

Reservoirs play an important role in global water supply. They often serve power generation and water supply for industry, agriculture and domestic use (Agostinho et al., 2015). However, reservoirs also cause anthropogenic interference with the terrestrial water cycle and surrounding environments (Gunnison, 1985; Vörösmarty and Sahagian, 2000), and also reflect the human disturbance to the local water resources (Feng et al., 2014; Palanques et al., 2014). Reservoir monitoring is therefore crucial for assessing their effects on regional hydrology and for water management. While reservoirs of strategic importance, typically large ones, are in many cases regularly monitored, remote and/or small reservoirs often lack adequate attention and monitoring although they also play a relevant role in regional water supply, hydrology and the local ecology of semiarid areas (Agostinho et al., 2015; Češljar and Stevović, 2015). Networks of dense reservoirs can significantly contribute to hydrology, sedimentology, geochemistry, and ecology in regional drainage systems and thus impact local water availabilty (Lima Neto et al., 2011; Smith et al., 2002; Warnken and Santschi, 2004). Studying the characteristics of remote and/or small reservoirs is, therefore, essential for gaining knowledge about local water availability and regional hydrology, and for efficient water management.

The topography beneath water bodies, usually shown with bathymetric maps, is fundamental inventory data. Water body substrate can influence the reflectance from water surfaces, and is thus an important factor to consider in water quality related studies (Lee et al., 1998; Maritorena et al., 1994; Mouw et al., 2015). Conventionally, a bathymetric map is obtained in field surveys by measuring the underwater topography using sonar sensors or depth meters mounted on boats (Becker et al., 2009). Alternatively, the bathymetry of water bodies can be derived by measuring a series of GPS points when they are (partly) dried out. However, results from conventional field bathymetric surveys are point- or swath-based and require further processing, such as interpolation (Becker et al., 2009; Costa et al., 2009), which introduces

uncertainties in the bathymetry map (Wechsler, 2006). Field investigation is labor intensive, time consuming and thus expensive, and often not feasible for large scale investigations.

Remote sensing technologies have shown great potential for water body detection and monitoring (Alsdorf and Lettenmaier, 2003; Alsdorf et al., 2007; Palmer et al., 2015). Compared to widespread remote sensing applications for studies on water surface, quality and volume variation, remote sensing applications in bathymetry studies are relatively few, and they use various approaches. In real aperture radar images acquired under moderate wind and strong tidal current conditions, shallow submarine ground was found to be visible (Loor, 1981), which is the case in synthetic aperture radar (SAR) images as well. The velocities of strong tidal current vary as they interact with the sea bottom topography, and thus is modulated, which causes variation in the local Bragg scattering determining the sea surface roughness and backscatters on SAR images (Alpers and Hennings, 1984a). Based on simulated SAR data, experiments have been conducted and models were successfully developed to investigate the bathymetric characteristics of shallow coastal areas (Alpers and Hennings, 1984b; Vogelzang et al., 1992). However, some external depth measurements and minimum wind conditions are compulsory for this approach, e.g. wind speed > 3 m/s (Reichert et al., 1998). Moreover, complex image mechanism involves a variety of not well-known parameters in the reversion model, leading these methods into simple scenarios (Romeiser et al., 2000). The above interaction of strong sea currents and the underlying topography also changes the wavelength or velocity of the near-shore currents. From the simulated velocity or the wavelength of the currents and the current direction mapped by SAR images, the dispersion of the underwater topography, and thus the bathymetry, was retrieved for the studied coastal areas (Bell, 1999; Brusch et al., 2011). However, this approach requires knowledge about the frequency of the waves, which is usually estimated from SAR images or other data sources (Bell, 1999; Brusch et al., 2011). Relying on the strong currents in open sea under certain wind condition, the SAR based methods mentioned above are inadequate for deriving the bathymetry of inland water bodies. Airborne Light Detection and Ranging (LiDAR) is an effective tool for obtaining an

accurate bathymetry. The data so acquired have been used as ground-truth for validating bathymetric maps derived from spaceborne satellite images (Lyzenga, 1985; Pacheco et al., 2015). However, data acquisition with LiDAR is relatively costly and thus usually limited to small scale studies. Moreover, the turbidity of water bodies and submerged objects (e.g. macrophytes) pose an impact on the results (Guenther et al., 2000). Based on spectral reflectance from water bodies, empirical and modified semi-analytical models have been developed (Lee et al., 1999; Lyzenga, 1985). Bathymetric mapping of coastal areas using optical data such as Landsat, SPOT and airborne hyperspectral images yields bathymetric maps with accuracies in the order of one meter (Brando et al., 2009; Jay and Guillaume, 2014; Lafon et al., 2002; Lee et al., 1999; Pacheco et al., 2015; Sandidge and Holyer, 1998). Detectable water surface reflectance is the basis of these methods. However, atmospheric condition, substrate type, water depth, clearness, turbidity, constituents, etc. and the variations of these parameters have narrowed the range of waters in which to apply these approaches (Brando et al., 2009; Lafon et al., 2002; Lee et al., 1999; Philpot, 1989; Ustin, 2004), The methods are most suitable under cloud-free conditions as well as for clear and shallow water bodies (e.g. ten meters). Besides, most remote sensing methods for bathymetric mapping focus on coastal areas, while the number of studies targeting inland water bodies is relatively limited. Arsen et al. (2013) and Feng et al. (2011) derived bathymetric maps for large reservoirs from the water contours extracted for the reservoirs from the time series of Landsat images. They attributed the elevations of the water contour from satellite altimetry data or field elevation measurement along transects of these contours, and then interpolated the bathymetric maps of the studied lake from these isolines. The significantly changing inundation areas in the targeted lakes, the frequent mapping of these areas, and availability of precise elevation data are the major prerequisites of this approach. However, the long time series of cloud-free images are not always feasible to archive the changes in the inundation. Due to the large distance between footprints of altimetric measurements, only limited altimetry data are available for dense and/or small reservoirs. Taking ICESat data for example, its 150 m inter-footprint along the tracks and

about seven km inter-tracks distances make it insufficient for bathymetric mapping in areas with dense and small water bodies. In addition, clouds reduce the feasibility of using spaceborne optical images and altimetry data for ground mapping.

Interferometric SAR (InSAR) offers an alternative technique for bathymetric surveys of inland waters in semiarid areas, by generating a DEM over low-water-level reservoirs (Amitrano et al., 2014a, 2014b). InSAR is a powerful technique for DEM generation and land surface displacement investigations (Bamler and Hartl, 1998; Rosen et al., 2000). The Shuttle Radar Topography Mission (SRTM) DEMs generated from airborne C- and X- band SAR data are successful examples of DEM generation via InSAR (Farr et al., 2007). Regional DEMs have been derived via repeat-pass interferometry from SAR data, such as ERS data, and from a combination of ERS and ENVISAT ASAR data (E et al., 2004; Small, 1998; Wegmüller et al., 2009). However, DEMs generated from these data are characterized by relatively coarse resolutions and low accuracies (Wechsler, 2006). The removal of atmospheric disturbance and temporal decorrelation should be considered when applying repeat-pass interferometry (Crosetto, 2002).

TanDEM-X is a novel mission launched in June 2010 and conceived to generate consistent, high resolution DEMs with worldwide coverage. In this mission the two X-band SAR images used for DEM generation are acquired at slightly different incidence angles by two nearly identical satellites flying less than 1 km apart. In the bistatic cooperation mode, the SAR sensors mounted on the two satellites simultaneously receive the echoes of SAR signals transmitted to the ground by one of these satellites, the so-called master satellite. The paths of the signal obtained by the sensors on board the two satellites are nearly identical and the time lag between the two receivors are very slight resulting from the small distance between the two satellite (Krieger et al., 2007). Therefore, the interferograms generated from SAR data acquired in this mode are free of atmospheric disturbance and temporal decorrelation of the ground. Two to three global coverages with TanDEM-X data acquired with different satellite flight distances, so-called baselines, were employed to secure the high accuracy of the final global DEM,

particularly for areas characterized by difficult terrains (Krieger et al., 2007). As a result, areas covered by water which produced incoherencies in the interferogram in any of the global coverages are inconsistent in the multiple coverages and masked out from the final global DEM product (TanDEM-X ground segment, 2013). Nevertheless, the single pass TanDEM-X data acquired in bistatic mode are still of high orbital accuracy and resolution, allowing for their application in various land surface related studies (Karila et al., 2015; Kubanek et al., 2015; Moreira et al., 2004; Rossi and Erten, 2015; Schlund et al., 2013). DEMs generated from single pass TanDEM-X data for water-free areas in the reservoir have potential for recovering the corresponding topography. Having involved only single pass TanDEM-X data, the generated DEMs are expected to be more comparable to the intermediate TanDEM-X DEM (IDEM) rather than the final global TanDEM-X DEM, the former having been improved through inclusion of flood extents for flood modelling (Mason et al., 2016). Obtained from single pass TanDEM-X images acquired during low water level, these TDX DEMs will show much smaller water area than the global TanDEM-X DEM in this region does. Moreover, TDX DEM from single pass interferometry is expected to be free of seasonal changes that exist in the global TanDEM-X DEM due to the multiple coverages of TanDEM-X data involved.

This study aims to map the bathymetry of reservoirs in a study site in the federal state of Ceará, northeastern Brazil, and to compare the results with the bathymetric maps derived from field surveys. Numerous dams of various sizes have been constructed in NE Brazil to assure a water supply during the dry season (SIRH/Ce, 2015; Sugunan, 1997). In most cases, inventory data for these remote and/or small reservoirs are missing or out of date due to siltation (Lima Neto et al., 2011; SIRH/Ce, 2015). In this study, we generated DEMs from single pass bistatic TanDEM-X data acquired during the dry season, i.e., at low water level, to reveal the bathymetric information for the reservoirs of interest. DGPS data measured in the field were used to assess the accuracy of the output TDX DEMs. The TDX DEMs selected to reflect the reservoirs' bathymetry are further compared to the bathymetric maps derived from field survey.

2.2 Study area

Numerous reservoirs have been constructed in northeastern Brazil to supply water for both urban and rural communities. However, the water demand is not always met, especially in the drought spells. Different projects and organizations on the country, state and local municipality levels have resulted in inconsistent monitoring of these water bodies (SIRH/Ce, 2015). In general, reservoirs supported by the state or the nation are regularly monitored and maintained because of their strategic importance. But the numerous small and/or remote reservoirs constructed to support the population in rural areas are hardly monitored or studied (IBGE, 2015), thus little information is available about their parameters.

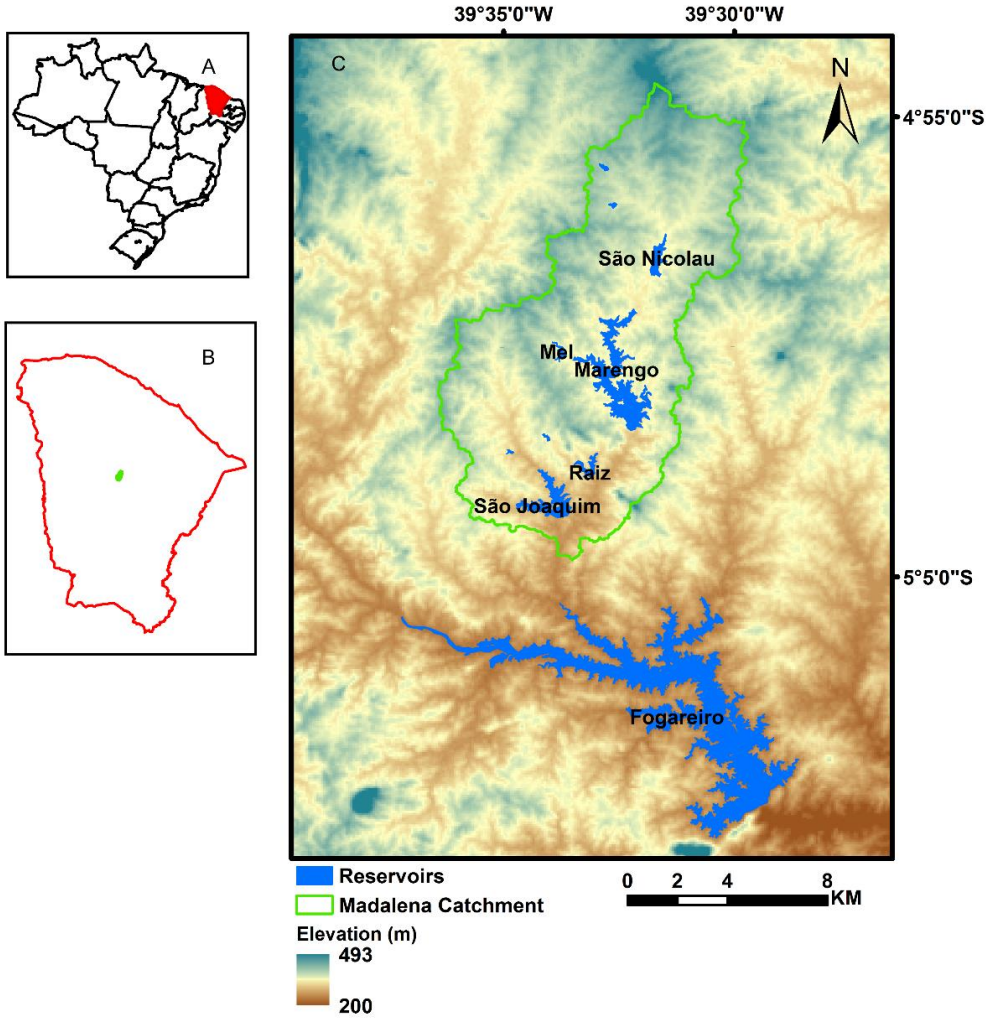

Figure 2.1 Location of the Madalena catchment and the studied reservoirs. A: Location of Ceará state in Brazil; B: Location of the Madalena catchment in Ceará state; C: Reservoirs of interest in the presented

study and the surrounding elevations.

The study site consists of the 124 km^2 Madalena catchment, located in the rural central Ceará (Figure 2.1). The climate is characterized by pronounced wet and dry seasons (Figure 2.1 A), putting this area in the drought polygon of northeastern Brazil. January to July is the wet season; the dry season extends from August to December (Figure 2.1 A). The average annual precipitation is ~ 600 mm and the potential evaporation exceeds 2000 mm per annum. The elevation of the catchment ranges from 100 to 700 m. Caatinga, an endemic seasonal shrubby forest landscape type in northeastern Brazil with very few trees (Bullock et al., 1995), is the dominant land cover. The crystalline bedrock does not have potentials for groundwater storage or supply. Since the 1930s, 13 reservoirs have been constructed in this catchment to support households in the adjacent settlements. All these reservoirs support the local inhabitants by supplying water for domestic consumption, livestock farming and irrigation. Throughout the year, water levels in the reservoirs fluctuate significantly. In dry years, such as 2012, 2013 and 2015, most reservoirs in this area are empty by the end of the dry season, as presented in Figure 2.2 B-F. The reservoirs in the Madalena catchment are not included in the regular state monitoring program. Reservoir monitoring in this catchment was started only recently by the Federal University of Ceará. So far, only Marengo, São Joaquim and São Nicolau reservoirs have been investigated in terms of bathymetry. This study focuses on five reservoirs in the Madalena catchment, namely Marengo, São Joaquim, São Nicolau, Raiz and Mel, and one large reservoir, Fogareiro, in the adjacent area (Figure 2.1).

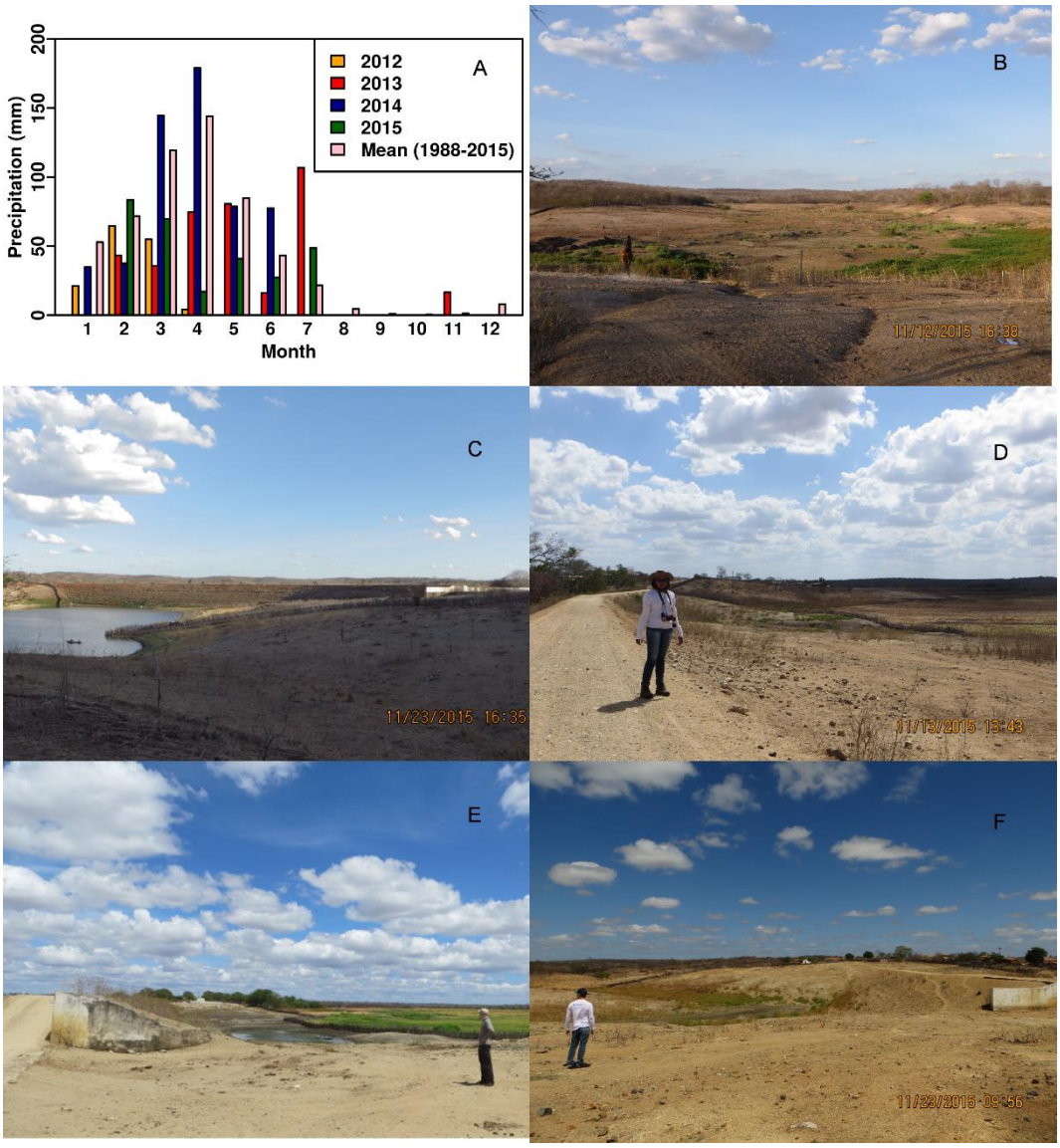

Figure 2.2 Precipitation at Madalena (A) and overview of reservoirs in the Madalena catchment in the dry season, B: Raiz, C: Marengo, D: São Joaquim, E: São Nicolau, F: Me

2.3 Data and method

Different remote sensing datasets and field data were employed in this study. TanDEM-X data were the basic data source for DEM generation. In addition, the SRTM DEM was included in the DEM generation after it was calibrated with ICESat data. Finally, multispectral RapidEye images served in the extraction of the water area-to-volume relationship. Various field data (e.g. DGPS data and field bathymetric measurements) were used to evaluate the performance of the proposed approach and the final results.

DEMs were generated from bistatic TanDEM-X data via single-pass interferometry. The coherence of the interferogram was investigated to study the real-time extent of the water retained in the reservoirs. The water area-to-volume relationship for several reservoirs was derived both from TDX DEM and bathymetric maps derived from field survey.

2.3.1 Data

2.3.1.1 TanDEM-X data

Three TanDEM-X stripmap data sets acquired from a descending orbit in bistatic mode with single polarization HH were used in this study (Table 2.1). The TanDEM-X data were supplied by the German Aerospace Center (DLR) in co-registered single look slang range complex (COSSC) format. The average coherence of the three data sets is above 0.80 (Table 2.1) and much higher than the overall coherence of TanDEM-X data for the generated global DEM (Martone et al., 2012). Each TanDEM-X scene covers an area of 50×30 km² (TanDEM-X ground segment, 2012).

Table 2.1 Parameters of the TanDEM-X data sets

	TanDEM-X 2011-07-05	TanDEM-X 2014-02-16	TanDEM-X 2014-03-21
Height of ambiguity (HoA) (m/2pi)	46.49	46.72	33.70
Effective baseline (m)	115.69	112.22	155.32
Average coherence	0.87	0.87	0.86
Scene center incidence angle	33.76	33.71	33.70

2.3.1.2 SRTM DEM V4.1

A void-filled and mosaicked SRTM DEM V4.1 with 90 m resolution was obtained from the Consortium for Spatial Information (CGIAR-CSI). The EGM86 geoid was subtracted from the

SRTM DEM, so the SRTM DEM employed is based on the WGS84 ellipsoid.

2.3.1.3 ICESat data

The Ice, Cloud, and land Elevation Satellite (ICESat) mission which was operated from 2003 to 2009, provides data for terrestrial and the oceanic studies. The data are available from the National Snow and Ice Data Center (NSIDC). Based on the consideration that C- band SRTM DEM and the X- band TanDEM-X data mostly express the surface elevation of the ground with shallow penetration, the Geoscience Laser Altimetry System 14 (GLAS 14) on board ICESat was chosen. GLAS 14 measured the elevation of the ground surface, with an accuracy of ~ 15 cm (Zwally et al., 2002). The ICESat data used in this study is from the Release 34.

2.3.1.4 RapidEye images

Two tiles of RapidEye images (level 3A) with resolution of five m acquired on 2009-11-11 over the study area were selected to derive the nominal maximal water extents of reservoirs. Exceptionally, RapidEye image acquired on 2014-08-02 presents the largest water extent for the Sao Nicola reservoirs. The RapidEye images (level 3A) acquired on 2014-01-23 were also employed to represent the real time status of the reservoirs in late January 2014. The RapidEye images were co-registered based on DGPS data within a locational accuracy of one pixel, i.e., five meters, before water extent delineation.

2.3.1.5 Field data

In May-June 2014, a total of 26 ground-truth points distributed throughout the TanDEM-X scene were measured in the field with differential GPS using the post-processing positioning method. Open and vegetation-free places, similar to the water-free reservoir bottom, were chosen for the measurement. The accuracies of the DGPS points are at 10 centimeter-level in the vertical direction and centimeter-level in the horizontal direction. The final geographic coordinate system is based on WGS84.

Bathymetric data from the field were available for Marengo (2012), São Joaquim (2011), and São Nicolau (2014) reservoirs. Bathymetric measurements in the field were obtained via a

depth-meter mounted on a boat, with the assistance of a handheld GPS contributing the coordinates of the measurements. Consequently, the field measurements are a series of points with horizontal five meters accuracy from the handheld GPS, and vertical decimeter accuracy from the depth meter. The point measurements were interpolated via ordinary Kriging methods using a spherical model, resulting in raster files with pixel spacing of 10 m. During the field campaign for the bathymetric survey, the water extents of the reservoirs were determined with a handheld GPS by walking along the shorelines. On 2014-02-23 the water extents of the reservoirs were acquired in the same way. Thus, the accuracy of the field water extents is approximately five meters. Currently, these field measurements are the only available bathymetric data for reference purposes

2.3.2 Methods

2.3.2.1 SRTM DEM calibration

In the global TanDEM-X DEM generation, the differential interferogram was obtained by removing the phase of earth represented by the ellipsoid, and the absolute phase was estimated via the radargrammetric measurements with the pair of TanDEM-X sensors (Rossi et al., 2012). In this study, the calibrated SRTM DEM was used.

In order to derive TDX DEMs of high absolute accuracy, the introduced SRTM DEM should be as reliable as possible. Due to the rolling baseline during data acquisition, SRTM DEM contain long wavelength shifts up to 10 m on the scale of a thousand kilometers, varying globally (Braun and Fotopoulos, 2007; Huber et al., 2009; Rodriguez et al., 2006). Eighty-four points at bare land were selected from GLAS 14 data of the ICESat mission to calibrate this offset. The area covered by a TanDEM-X scene is ~ 30 km wide, only a few percent of the spatial range of the offset in the SRTM DEM. The offset of the SRTM DEM is expressed in the form of $Y= aX+b$. At this 30-versus-10-thousand-km scale, the constant component b is regarded as more critical than component a, the linear gradient. Therefore, only b is calculated and removed here. The component b of the SRTM DEM offset calculated for the study area is 2.75 m, very close

to the results in Huber et al. (2009). After the offset removal, the calibrated SRTM DEM was then transformed from the cartographic coordinate system into the SAR slant coordinate expressed in column and row.

2.3.2.2 DEM generation with single pass interferometry

DEM generation from single pass bistatic TanDEM-X data was realized using the modules DIFF&GEO and ISP in GAMMA software (Werner et al., 2000). The procedures for DEM generation from bistatic TanDEM-X data were conducted in GAMMA. The workflow followed in this study is illustrated in Figure 2.3. The DEM generation starts with interferogram generation from TanDEM-X images, since the data were already co-registered before delivery. The TanDEM-X data were multi-looked by 6×5 or 4×5 to get a square pixel of 10 m spacing and a high signal-to-noise ratio (SNR).

Because the TanDEM-X data were acquired in bistatic mode, atmospheric disturbance is disregarded. The very short duration of data acquisition, 50-200 s, hardly allows any ground deformation. Thus the phase information in the interferogram only refers to the systematic characteristics of the instruments and the ground objects. With the orbit data of the TanDEM-X master image the unwrapped phase of the earth in this area was simulated from the calibrated SRTM DEM. During the simulation, the uncalibrated SRTM DEM was resampled to the same pixel spacing as the multi-looked TanDEM-X data. A differential interferogram was obtained by subtracting this simulated unwrapped phase from the interferogram derived from TanDEM-X data. The adaptive filter described by Goldstein and Werner (1998) was applied to remove the phase noise from the differential interferogram and to ensure a smoother interferogram. We applied the commonly used Minimum Cost Flow (MCF) procedure for phase unwrapping. A few unwrapping errors were produced at the marginal area of the scene due to the sharp terrain there, but they do not influence the overall phase unwrapping.

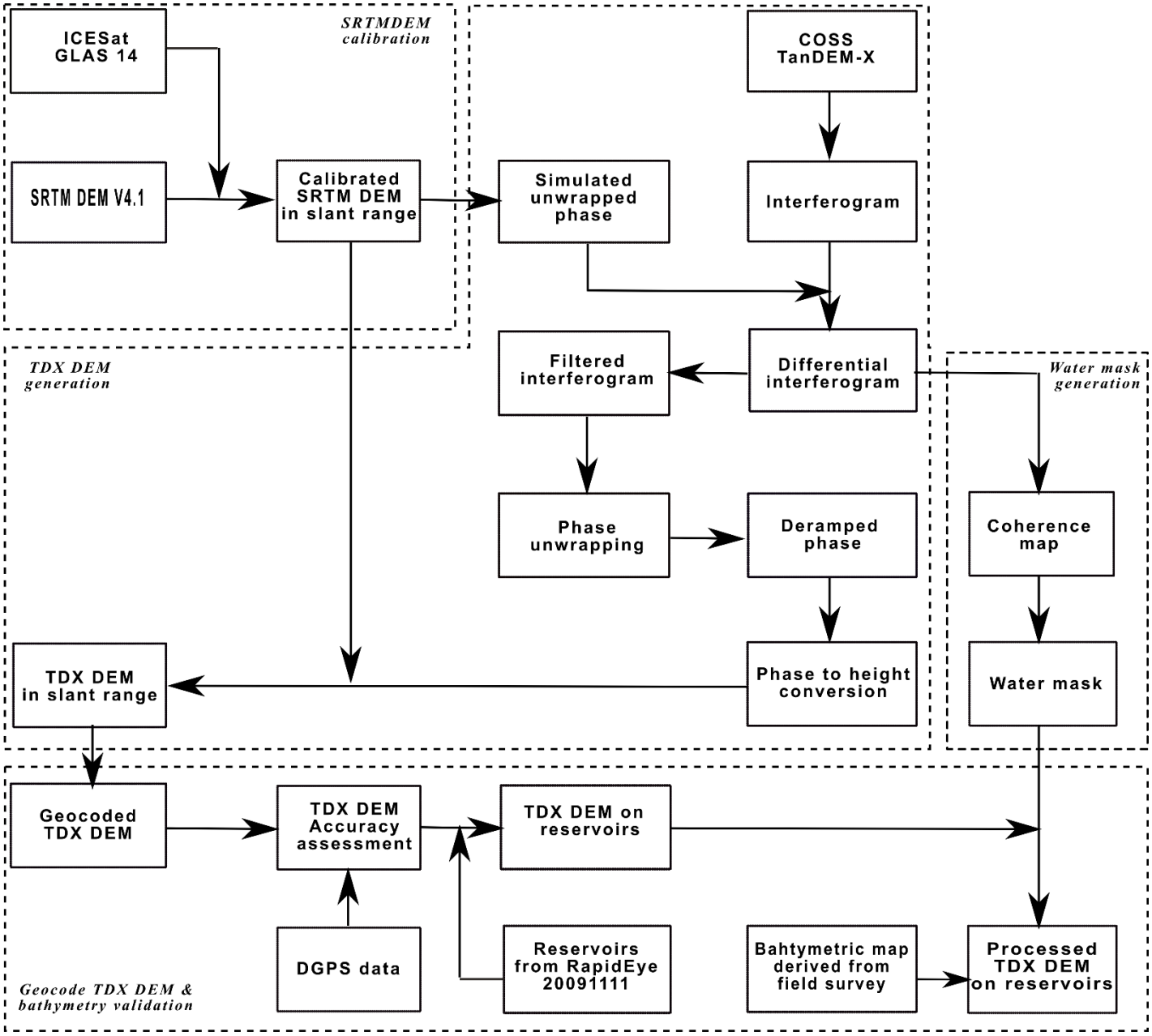

Figure 2.3 Workflow followed in this study. The blocks enclosed with dash line indicate the major steps undertaken in the study, i.e. the SRTM DEM calibration, the TDX DEM generation, water mask generation, geocoding of the TDX DEM and validations of reservoirs bathymetry.

During TanDEM-X data acquisition the bias in baseline estimation causes error in DEMs both in the across-track and azimuth directions (González and Bachmann, 2010; Gruber et al., 2012; Krieger et al., 2007). But only the component of cross track error in the line of sight matters, as it causes a noticeable displacement of a few meters and a tilt at the slope of a few cm/km in

range in the final DEM (González and Bachmann, 2010; Gruber et al., 2012). To remove this effect, a 2D linear surface was estimated using the least-squares error criterion (Werner et al., 2000), and subsequently subtracted from the unwrapped phase, resulting in the de-ramped phase in Figure 2.3 with the effect of bias in baseline estimation eliminated. Afterwards, the sum of the calibrated SRTM DEM and the height map which originated from the unwrapped phase via HoA was geocoded with Range Doppler methods defined in Goblirsch and Pasquali (1996). The path delay introduced by the troposphere was not considered in geocoding, which might cause an inaccuracy of around 2.6 m in the horizontal direction according to TanDEM-X payload ground segment (2012), but this was considered acceptable for a pixel spacing of 10 m.

2.3.2.4 Water area from coherence map

Due to the specular reflectance of open and still water surfaces, hardly any SAR pulses transmitted towards this type of water are reflected back to the sensors. Moreover, water usually decorrelates in a time lag of tens of ms (Bamler and Hartl, 1998; Wendleder et al., 2013), while the along-track lag of less than 50 ms between the two TanDEM-X receivers cooperating in bistatic mode is beyond this limit. Consequently, open and still water often presents low SNR in SAR images and small coherence in the interferogram derived from the bistatic TanDEM-X data. Coherence has been used to detect flooding and generate water masks (Nico et al., 2000; Wendleder et al., 2013). Thresholds of 0.2 on the coherence map, and 0.23 on the coherence map together with a threshold of 4 applied on digital numbers, have been used to extract masks for open water (Rossi and Erten, 2015; Wendleder et al., 2013), but the validation with real time field data was infeasible for these studies. However, rather than open water, it is effective water area that is of interest in this study. A few herbaceous plants growing along or in the waters could potentially lead to the increased coherence values of waters, which can alter the elevation on TDX DEM in these areas. Therefore, in order to achieve a more reliable DEM to represent the reservoir bathymetry, it is necessary to overestimate the area of open water. We did this by increasing the aforementioned thresholds which were used in the studies for open water mask. The coherence map of TanDEM-X data was derived from the

non-filtered differential interferogram, taking the slope of phase into consideration. After comparing the water extents acquired in the field on 2014-02-23 with the polygons derived from coherence of interferogram 2014-02-16 obtained with different thresholds (Figure 2.4 C), areas where coherence < 0.6 were regarded as water. This threshold is within the tolerance of the average coherence of the TanDEM-X scene list in Table 1. The threshold of coherence < 0.6 can efficiently overestimate the possible waters, even exclude the water free area outside of the reservoir as shown in Figure 2.4 C-D.

Introducing the coherence map derived from TanDEM-X interferograms into the workflow makes the retrieval of reservoirs' bathymetry less dependent on external field data of water extents. However, the threshold used for water mask should be accordingly adjusted for further application, depending on the vegetation presence and purpose of research, etc.

The RapidEye images on 2014-01-23 show that the terrestrial vegetation in this area is still dry, and green vegetation only grows along the waterlines (Figure 2.4 C), despite the fact that the wet season had already started and some rainfall was recorded in the three weeks before the image acquisition (Figure 2.4 C A).

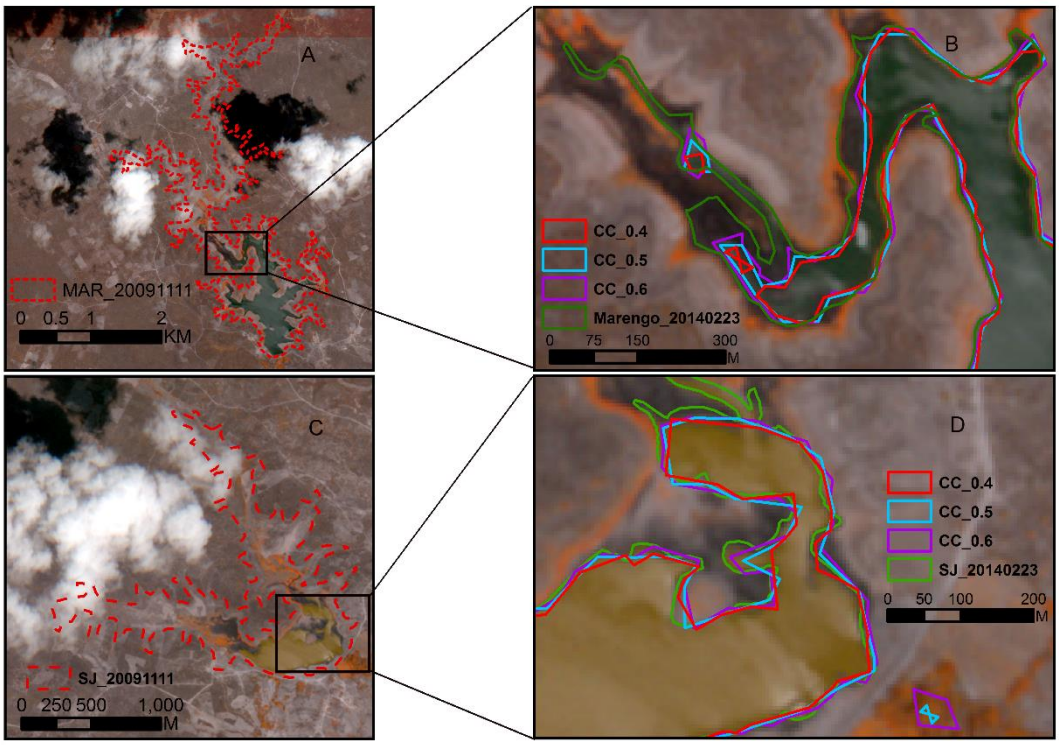

Figure 2.4 Comparisons of water extent in Marengo and São Joaquim. A) and C): water extent in Marengo and São Joaquim on 2009-11-11 overlaid on the RapidEye image acquired on 2014-01-23 (band combination: RGB: 543); B): and D): Subset of Marengo and São Joaquim in A and C. Water extent on 2014-02-23 from field, and polygons of water extents defined by different thresholds on coherence of TanDEM-X data 2014-02-16 overlaid on RapidEye image on 2014-01-23. CC stands for the coherence. The large discrepancy between the CC_0.6 and the SJ_20140223 located at the mudflat which is water free but cannot be accessed by walking, and the very narrow water way which is too narrow to be delineated from the coherence map.

2.3.2.5 Extraction of water area-to-volume relationship

The area-to-volume relationship expresses how the water volume in the reservoir varies with respect to the surface area of the water. Comparisons of the relationship shown in bathymetric maps derived from field survey and TDX DEM over the reservoir provide insights on the difference of the two approaches in bathymetric surveying. Before extracting the water area-to-volume relationship from TDX DEM 2014-02-16, the overestimated area of water in the reservoirs (coherence < 0.6) was attributed to the smallest surrounding elevation value. The flat terrain in the Madalena region barely introduces SAR shadows within the reservoir areas. The ten meters pixel spacing of the TDX DEMs is almost three times as wide as the dams. As a

result of averaging, the elevations of narrow dams shown on the DEMs, line C in Figure 2.5 was lower than their actual heights, line D in Figure 2.5. Due to the unavailability of spillway elevations, the upper limits of the water level for each reservoir were determined by the average elevation underlying the maximal water extents captured in RapidEye archive. Water extents were manually digitalized as polygons from the RapidEye images, considering the appearance of macrophytes floating on the water surface or emerging at the shorelines during data acquisition.

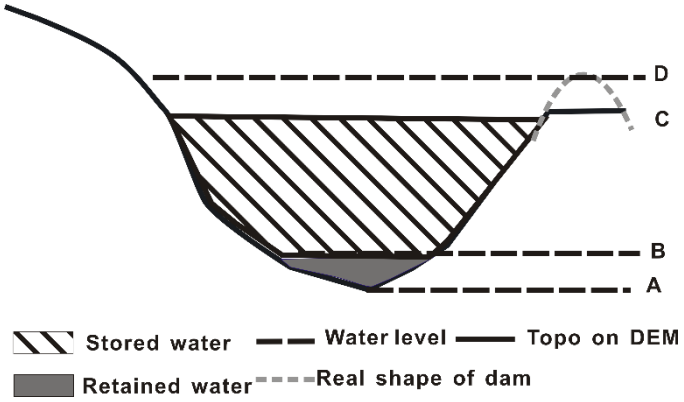

Figure 2.5 Illustration of reservoir profile in TDX DEM 2014-02-16. A, B, C and D stand for the possible water levels.

Water areas and volumes in the reservoirs were calculated with 0.5 m water level intervals using equation (2.1)

$$V_i = \sum_j^n (H_i - E_j) A_0 + V_0 \qquad (2.1)$$

where V_i is the volume of water stored in the reservoir when the elevation of water level is at H_i. The starting point of H_i is A in Figure 2.5 in the case of empty reservoirs, or B in Figure 2.5 in the case of reservoirs with retained water. The upper limit of H_i is D in Figure 2.5, and it is determined by water areas in RapidEye images on 2009-11-11. n is the number of pixels forming the water surface at water level H_i, E_j is the elevation of the j^{th} pixel in the TDX DEM. A_0 is the area of one pixel, 100 m^2 here with pixel spacing of 10 m. V_0 is the volume of retained water during the TanDEM-X data acquisition. When the water level changes from A in Figure 2.5 V_0 is 0 hm^3. In reservoirs where water was retained, the water level changed from B

in Figure 2.5; V_0 is calculated from bathymetric maps derived from field survey.

The accuracy of the volume at water level H_i was calculated based on the accuracies of the TanDEM-X derived DEM by summing up the errors of each water column represented by one pixel (equation (2.2)):

$$\Delta_i = \left(\frac{\sigma A_0 n}{V_i}\right) 100\% \qquad (2.2)$$

where Δ_i is the accuracy of the volume (%) at water level H_i, and σ is the absolute accuracy of the DEM in meters, established with DGPS data from field measurements.

2.4 Results

The three TDX DEMs were compared among one another and their accuracies were established with DGPS data. The areas of the water retained in the reservoirs were calculated from the coherence maps of the TanDEM-X data. The TDX DEM and bathymetric maps derived from field survey were compared at the following three aspects: the overall coverage, the distribution of measurements in the reservoir, profiles of bathymetric information for shape replication, and the water area-to-volume relationship derived from the two datasets.

2.4.1 Validation of the TDX DEMs

The TDX DEMs were compared to one another (Figure 2.6 A-C). In the two maps comparing the TDX DEMs in 2011 and 2014 (Figure 2.6 A-B), only at a few places was the elevation difference beyond the range of +2 to -2 m, which can be attributed to the land use changes, e.g. bushes degradation and the ground mass changes like new dam constructions. The remained areas show elevation differences within the range of -2 m and +2 m, with a standard deviation below 1 m and mean at zero meter. Most of the differences are in the range of -1 m to +1 m, particularly in the difference map for TDX DEM 2014-02-16 and TDX DEM 2014-03-21. The comparison map of TDX DEM 2011-07-05 and TDX DEM of 2014-03-21 (Figure 2.6 B) is slightly smoother than the one for TDX DEM 2011-07-05 and TDX DEM 2014-02-16. Acquired within an interval of 33 days, TDX DEM 2014-02-16 and TDX DEM 2014-03-21

have closer elevation overall, and the elevation differences are mostly in the range of -1 to +1 m (Figure 2.6 C) , smaller than the elevation difference in other two comparisons maps. Due to the flat terrain in this region, water bodies are the majority of the areas marked to be incoherent in Figure 2.6. The rest of the incoherent areas, i.e. hollow areas not overlaid by water bodies, indicate the locations where the terrain affects the TDX DEMs.

In the comparisons of the SRTM DEM with the TDX DEMs (Figure 2.6 D-F) similar spatial patterns are shown at the pixel size of 90 m. No obvious directional trend is noticed for the comparison between SRTM DEM and the TDX DEMs. The mean of the elevation differences are approximately -2.8 m (Figure 2.6 D-F), very close to the removed offset of -2.75 m, implying that the offset removal from the SRTM DEM is reasonable. The standard deviations of the differences reach 1.5 m, much larger than the values in the comparisons of the TDX DEMs, which might be evidence that the TDX DEMs have better relative accuracy than the SRTM DEM.

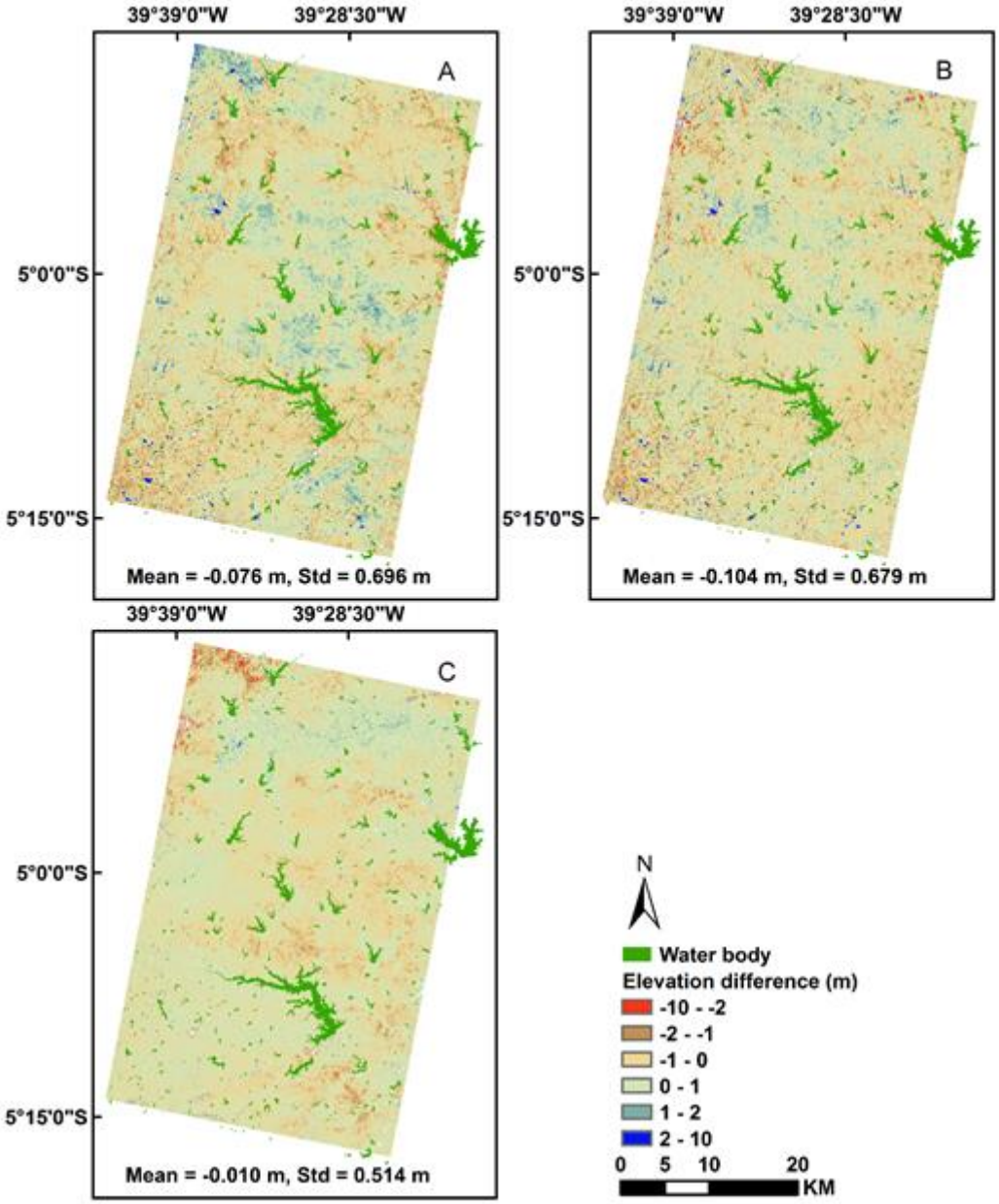
39°39'0"W
39°28'30"W
A
5°0'0"S
5°15'0"S
Mean = -0.076 m, Std = 0.696 m
39°39'0"W
39°28'30"W
B
5°0'0"S
5°15'0"S
Mean = -0.104 m, Std = 0.679 m
39°39'0"W
39°28'30"W
C
5°0'0"S
5°15'0"S
Mean = -0.010 m, Std = 0.514 m
N
Water body
Elevation difference (m)
-10 - -2
-2 - -1
-1 - 0
0 - 1
1 - 2
2 - 10
0 5 10 20
KM

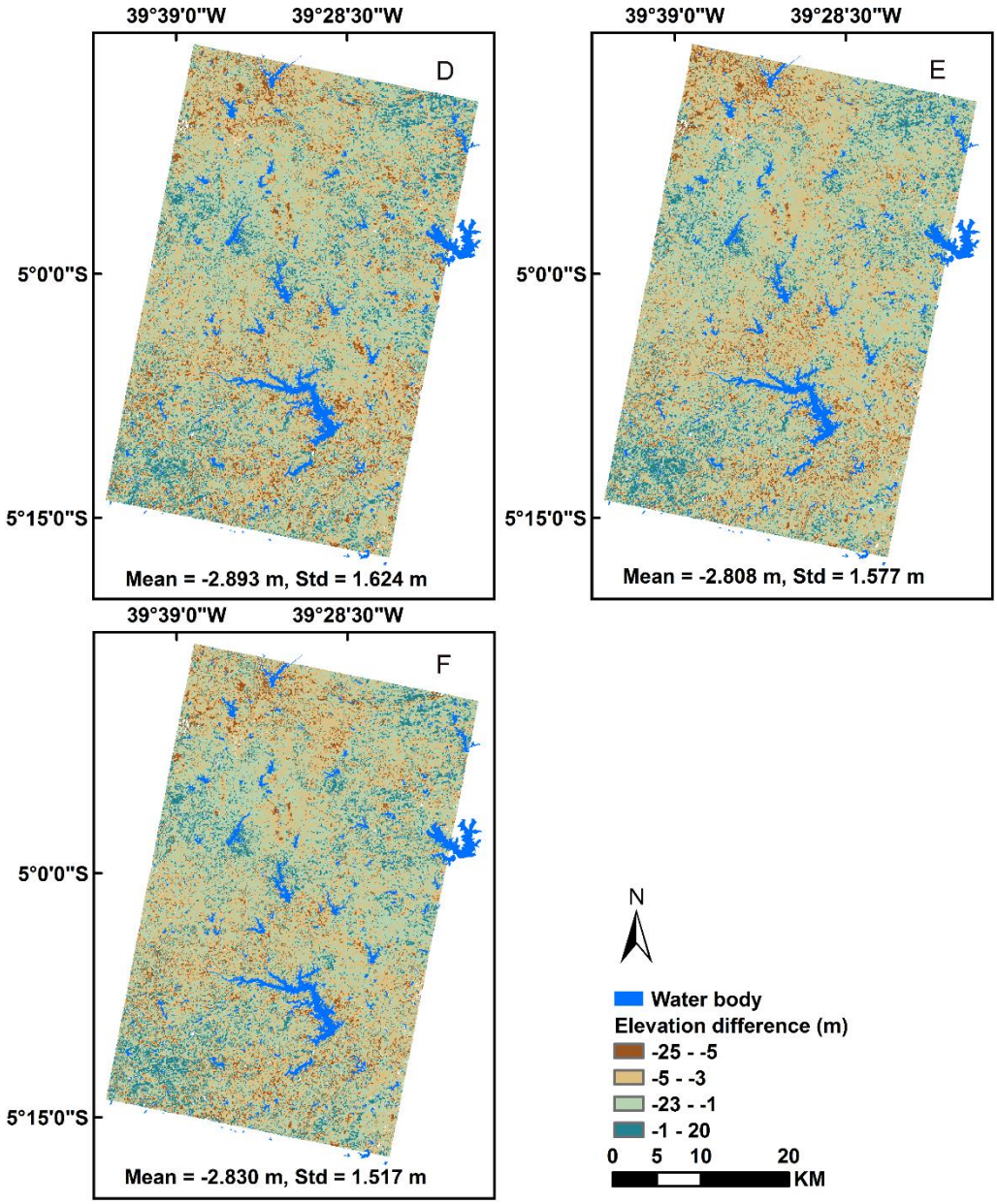

Figure 2.6 Comparison of the TDX DEMs and between the TDX DEMs and SRTM DEM. A): The result of subtraction of TDX DEM 2014-02-16 from TDX DEM 2011-07-05; B) the result of subtraction of TDX DEM 2014-03-21 from TDX DEM 2011-07-05; C) The result of subtraction of TDX DEM 2014-02-16 from TDX DEM 2014-03-21; D) The result of subtraction of SRTM DEM from TDX DEM 2011-07-05; E) The result of subtraction of SRTM DEM from TDX DEM 2014-02-16; F) The result of subtraction of SRTM DEM from TDX DEM 2014-03-21. Areas with coherence of less than 0.6 in either of the three interferograms were eliminated and displayed as holes in the comparison images as no-value areas.

2.4.2 Accuracy assessment

In the validation with DGPS data and DEMs derived from TanDEM-X data (Figure 2.7), nearly

all absolute elevation differences are in the range of +2 m to -2 m. Point No.7 was measured on a typical 3-4 m wide dam in the area. The elevation based on DGPS measurements at this point is the real elevation of the dam. The values from the three DEMs are the results of averaging neighboring lower ground and the dam and are therefore lower than the real values. Systematic offset among these three data sets are not significant (Figure 2.7).

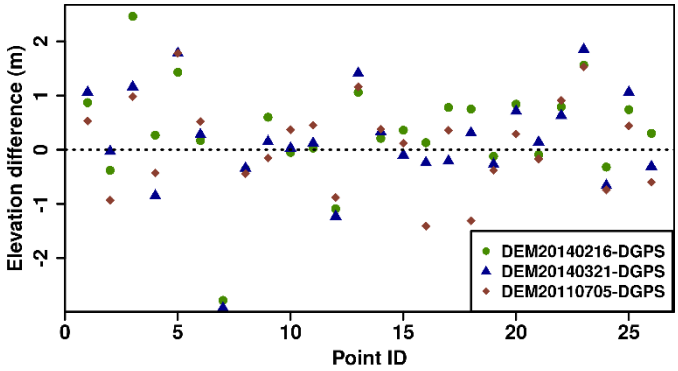

Figure 2.7 The validation of the TDX DEMs with DGPS data. The value of each plotted point was obtained by the subtraction of DGPS measurement from the corresponding elevation of the TDX DEMs pixels at the same locations. Positive values mean the TDX DEMs have higher values than from DGPS measurement, and vice versa. The measurements enclosed by the red rectangle were taken on the top of an approximately three meters high dam.

The accuracies of the three TDX DEMs were calculated according to Rosen et al. (2000) by referring to DGPS data (Table 2.2). The relative accuracies of the three TDX DEMs are slightly better than the absolute ones (Table 2.2). Both relative and absolute accuracies of the TDX DEMs in this study are better than the reported 2 m and 10 m in relative and absolute accuracies for the Global TanDEM-X DEM (TanDEM-X ground segment, 2013). The TDX DEM 2014-03-21 from TanDEM-X data with a long baseline and a small HoA (Table 2.1) yields overall better accuracy than do the other two TDX DEMs. However, the magnitude of the differences is very little and at the decimeter level the accuracies are comparable (Table 2.2).

Table 2.2 Vertical accuracies of the TDX DEMs generated in this study (m).

		TDX DEM 2011-07-05	TDX DEM 2014-03-21	TDX DEM 2014-02-16
Validation with DGPS data	Absolute accuracy	1.21	1.06	1.16
	Relative accuracy	1.16	1.01	1.03

Note: the values in the table are all provided at a confidence level of 95%.

The similarities between TDX DEMs from different TanDEM-X data demonstrated the stability of the workflow applied in this study for DEM generation. Inter-year land cover and seasonal changes can also be observed from these comparisons. The comparison of TDX DEMs and their accuracies proved the potentials of the TanDEM-X data for generation of the highly accurate DEM. Comparison between uncalibrated SRTM DEM and TDX DEMs shows that the offset removal was reasonable.

2.4.3 Water extents

During the acquisitions of the three TanDEM-X data sets for TDX DEM generation there were different amounts of water in the reservoirs. On 2014-02-16 the extents of retained water in the reservoirs were the smallest. TDX DEM 2014-02-16 was therefore chosen to reveal the bathymetry of reservoirs in the Madalena catchment, despite its slightly lower accuracy than the other two TDX DEMs. Table 3 shows the surface areas of retained water obtained from the field survey on 2014-02-23, and the water areas delineated from the coherence map of TanDEM-X data for 2014-02-16. With 7 days' time lag, the water areas from field data and coherence map defined by threshold coherence < 0.6 were nearly the same (Table 2.3). It demonstrates that the threshold of coherence < 0.6 is suitable for removing the effect of water retained in the reservoirs, despite the small area of mudflat around the open water displayed in Figure 2.4 C. In the case of São Nicolau, the areas of the water remained during the field trip on 2014-02-23 and during the overpasses of the TanDEM-X satellites on 2014-02-16 were nearly

0.00 km2, even after the overestimation of water surface. Thus, the areas of water in São Nicolau were represented with NA in Table 2.3, to indicate that nearly no water remained in the reservoirs on 2014-02-23 and 2014-02-16.

Table 2.3 Water areas in reservoirs in the Madalena catchment (km^2).

Reservoir	Marengo	São Joaquim	São Nicolau	Raiz	Mel
Water area on 2014-02-23 (field survey)	0.64	0.16	NA	0.01	0.01
Water area on 2014-02-16 (coherence < 0.6)	0.63	0.16	NA	0.01	0.01

2.4.4 Bathymetric map validation

Because no other bathymetric data were available for the reservoirs in the Madalena catchment, the bathymetric maps derived from field survey were used to compare against the TDX DEM 2014-02-16 in the reservoirs. The available field measurements reveal the depths of the surveyed waters, not the absolute elevations of reservoirs' bottom. In order to enable the comparison of bathymetries derived with the two approaches, we calculated the mean elevation of the TDX DEM 2014-02-16 pixels which underlie the con-current waterline (extent) during the field measurements. The field measurements were then aligned to the TDX DEM 2014-02-16 by subtracting them from this mean elevation. As a result, both the field measurements and TDX DEM 2014-02-16 present the elevations of the reservoirs' bottom. This is enough to illustrate how the same reservoir on TDX DEM 2014-02-16 morphologically varies from it on the bathymetric map derived from field survey. However, some uncertainties probably still exist in the absolute elevations converted from the field measurements as the mean elevation we employed may not be the real absolute elevation due to the accuracy of TDX DEM 2014-02-16. Therefore, the validations of TDX DEM 2014-02-16 in the terms of the bathymetric mapping were conducted only at a morphological aspect in the overall reservoir scale, to see the coverage and shape differences reflected by the two datasets.

Considering the absence of the precise reference elevation for the field bathymetric measurements, we did not directly compare the individual field measurements and corresponding pixels on TDX DEM 2014-02-16.

2.4.4.1 Bathymetric map comparison

For the purpose of resevoir bathymetry mapping, the DEMs generated from TanDEM-X data acquired between the end of the dry season and the beginning of the wet season are preferred. On the one hand, this is after the intensive evaporation in the dry season and before the wet season when the reservoirs are usually refilled. At this time water-free areas in reservoirs are usually at a maximum and the inundation area reaches the minimum. On the other hand, at this time the perennial acquatic plants in the inundation are expected to diminish due to the absence of water, and the possible elevation contribution/disturbance from these plants is minimal. For example, in the Madalena catchment, the occupation of macrophytes in the reservoirs was marginal in the dry season at the limited area of water surfaces (Figure 2.2 and Figure 2.4 C).

Figure 2.8 shows the reservoirs in the Madalena catchment on bathymetric maps derived from field survey and on TDX DEM 2014-02-16. Only reservoirs with available field bathymetric measurements are presented here. The reservoir areas were extracted from TDX DEM 2014-02-16 with the maximal water extents recorded in the RapidEye archive (i.e. RapidEye image on 2009-11-11 for the majority of the reservoirs and RapidEye image on 2015-08-02 for São Nicolau). Before the extraction, a buffer of 40 m was added to the reservoirs' extents to better illustrate the reservoirs bathymetry on the TDX DEM 2014-02-16. Only for São Nicolau was a buffer of 100 meter applied, considering that the maximal extent recorded in RapidEye archive for this reservoir was smaller than the water extent in June 2014 when the field bathymetric survey was conducted. The water extents acquired in the field on 2014-02-23 were overlaid on both bathymetric maps. Bathymetric maps derived from field survey and TDX DEM 2014-02-16 were compared at the spatial scale. As the five meters accuracy of the handheld GPS is below the pixel spacing of TDX DEMs (ten meters), no horizontal uncertainty

was considered in the comparison between TDX DEM 2014-02-16 and the bathymetric maps derived from field survey.

At the time of the field campaign for bathymetric survey in Marengo and São Joaquim, the water in the reservoirs was not at the maximum, i.e., as at 2009-11-11. Bathymetric maps derived from field survey for these two reservoirs, therefore, cannot cover the complete extent of the reservoirs (Figure 2.8). The depths of most branches of the two reservoirs were not measured during the field campaigns, although they were inundated (Figure 2.8). On TDX DEM 2014-02-16, areas free of water including the branches were fully covered with continuous measurements in Marengo and São Joaquim. The elevation of the lowest areas occupied by the retained water is left unknown (Figure 2.8) . Attributing these areas with the minimum surrounding values results in the flat-bottom shapes for the two reservoirs on TDX DEM 2014-02-16. In general, on TDX DEM 2014-02-16 the topography inside the reservoirs Marengo and São Joaquim is smoother and gentler than shown in bathymetric maps derived from field survey (Figure 2.8).

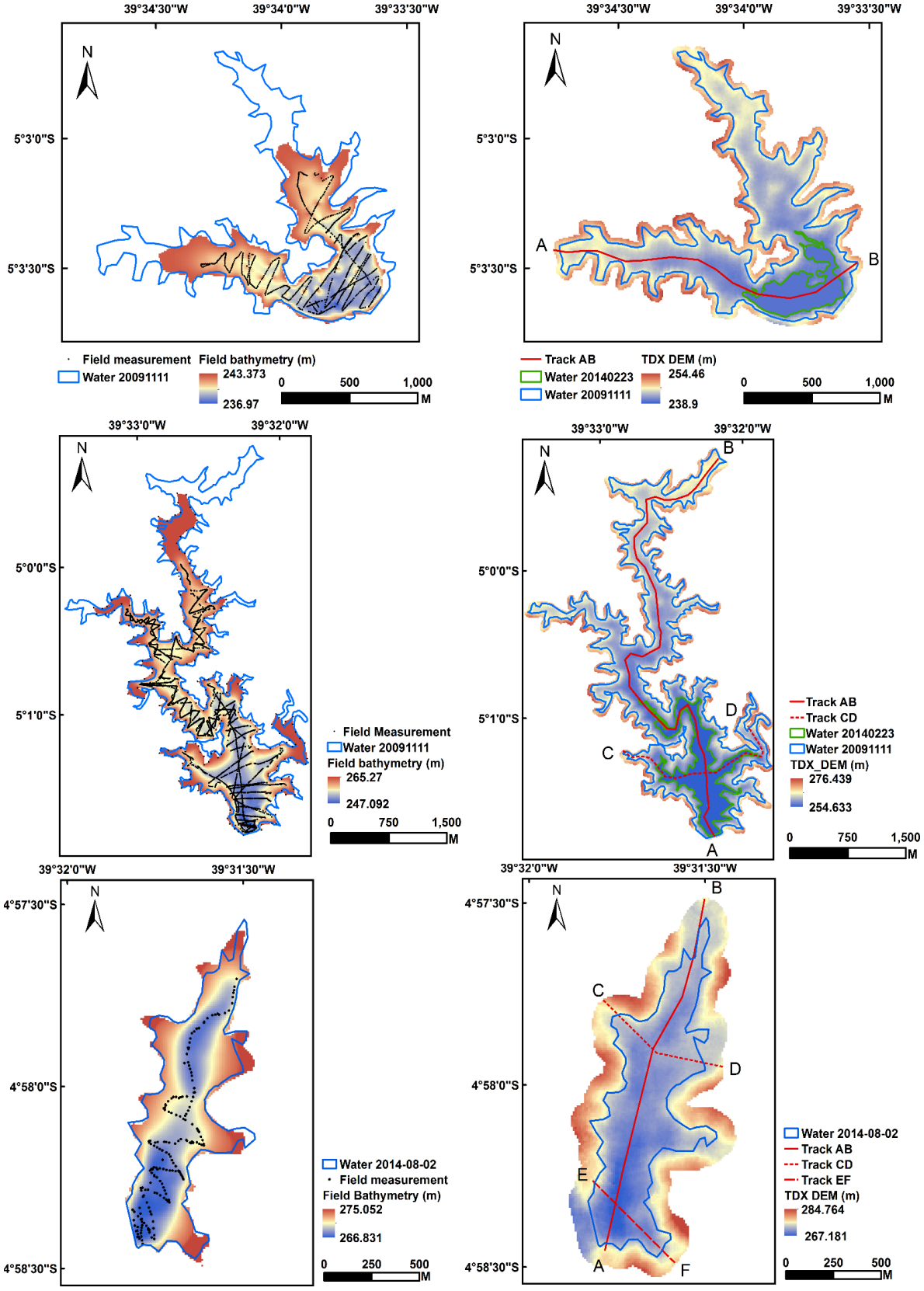

Figure 2.8 Comparisons of the bathymetric maps derived from field surveys (left column) and the TDX DEM 2014-02-16 (right column) for São Joaquim Reservoir (top row), Marengo Reservoir (middle row) and São Nicolau

Reservoir (bottom row).

In São Nicolau, the emergent macrophytes at the northern part impeded the collection of depth measurements from a boat. A vast area of vegetation left only a narrow channel for the boat to pass through and survey the reservoir bathymetry (Figure 2.8). As a result of interpolation from sparse field measurements, the shape of the reservoir at the northern part is steep in bathymetric maps derived from field survey, particularly in the northern part. On TDX DEM 2014-02-16, São Nicolau could be completely mapped because it was empty during the TanDEM-X image acquisition (Figure 2.8).

Overall, TDX DEM 2014-02-16 results in a continuous bathymetric map for the reservoirs investigated with evenly distributed measurements of pixels. The bathymetric maps derived from field surveys are based on the point-wise field measurements, which are in many cases unevenly distributed due to the inaccessibility caused by either the shallowness of the waters or the obstruction of the emergent macrophytes at these areas. Derived from data acquired in the dry season, TDX DEM 2014-02-16 mapped the majority of the reservoirs with an accuracy of about one meter while bathymetric maps derived from field surveys were constrained by the water extents at that time which were in many cases not at the maximum and, thus, only part of the reservoirs were surveyed.

2.4.4.2 Profiles of bathymetric maps derived from field survey and TDX DEM 2012-02-16

Figure 2.9 shows the comparison between bathymetric maps derived from field survey and TDX DEM 2014-02-16 in the three reservoirs along the tracks marked in Figure 2.8. The performance of two bathymetric mapping approaches in preserving the reservoirs shapes are presented in this subsection.

In São Joaquim at the area indicated as water on TDX DEM 2014-02-16, the elevation on bathymetric map derived from field survey fluctuates slightly and remained of nearly the same magnitude (Figure 2.9 A). In São Joaquim the maximal depth unmeasured by TDX DEM 2014-02-16 is about one meter (A). The long diameter of the unmapped areas is approximately

500 m, but the mapped value is 3 000 m. The total depth of the reservoir is eight meters.

In Marengo the north–south transect passes through an island at 500 m in the profile of TDX DEM 2014-02-16, where an elevation jump is displayed (Figure 2.9 B). But the morphology of this island is not shown in bathymetric maps derived from field survey (Figure 2.9 B). On the west-east transection of the bathymetric map derived from field survey in Marengo, an elevation difference is shown at ~ 250 m in the inundation area (Figure 2.9 C). But this variation is not visible in the north-south transect of bathymetric map derived from field survey or in TDX DEM 2014-02-16 (Figure 2.9 B). This could be due to the appearance of submerged plants, a few tree stumps or even artifacts in the point-wise measurements. This is because solid objects that were above the water surface on 2014-02-16 and larger than one pixel would present high coherence in the interferogram and be displayed accordingly in TDX DEM 2014-02-16. The maximal unmeasured depth of the inundated areas in Marengo is approximately five meters, but the mapped maximal depth of the reservoir is 10 m (Figure 2.9 A-C). On 2014-02-16 the longer diameter of the unmapped Marengo area is on the order of 2 000 m, while that of the mapped area is 7 000 m. Combining the bathymetric map derived from field survey and the TDX DEM 2014-02-16, the total depth of Marengo is 15 m.

No water retention appeared in São Nicolau on 2014-02-16, thus the profiles from the bathymetric map derived from field survey and TDX DEM 2014-02-16 are expected to show a similar shape for the reservoir. However, the bathymetric map derived from field survey and TDX DEM 2014-02-16 show significantly different shapes for the reservoir Figure 2.9 D-F). On the TDX DEM 2014-02-16 São Nicolau is seen as open and wide, and the gradient is gradual while the bathymetric map derived from field survey casts a rather narrower shape for this reservoir (Figure 2.9 D and E) with abrupt topographic fluctuations (Figure 2.9 F). The areas with large bathymetric discrepancies are located at the boundary and the center of the reservoirs (Figure 2.9 D-F). For the central area (Figure 2.9 D), the discrepancy was probably caused by submerged vegetation or stumps. At the boundary region, the shallow waters were inaccessible and there is thus a lack of field measurements. Consequently, the bathymetric map

derived from field survey for these areas was interpolated from a few relatively distant measurements and thus shown as flat (Figure 2.9 E and F). The bathymetric map derived from field survey in São Nicolau does not completely replicate the shape of the reservoir. São Nicolau was empty on 2014-02-16, and the entire reservoir bottom was therefore mapped by TanDEM-X data and presented high coherence. As a result, for those areas with a large bathymetric discrepancy, the TDX DEM 2014-02-16 should reflect a more reliable shape for São Nicolau. The interference of macrophytes on the field bathymetric survey during the wet season was avoided.

In general, in the profiles of São Joaquim, Marengo and São Nicolau reservoirs (Figure 2.9 A-F) the flat features on TDX DEM 2014-02-16 indicate the areas of water retention during the TanDEM-X data acquisition. Elevations of these areas were attributed from the minimal elevation of the adjacent pixels. On the profiles of bathymetric maps derived from field survey in these reservoirs, the flat features are mainly at the shallow areas adjacent to the reservoirs' boundaries (Figure 2.9 B-F). At boundary areas, the bathymetric maps were interpolated from the elevations of the bank that were far away from the depth measurements in the water. Large population of emergent macrophytes which hindered the access of field measurement have probably contributed to this effect, e.g. in São Nicolau.

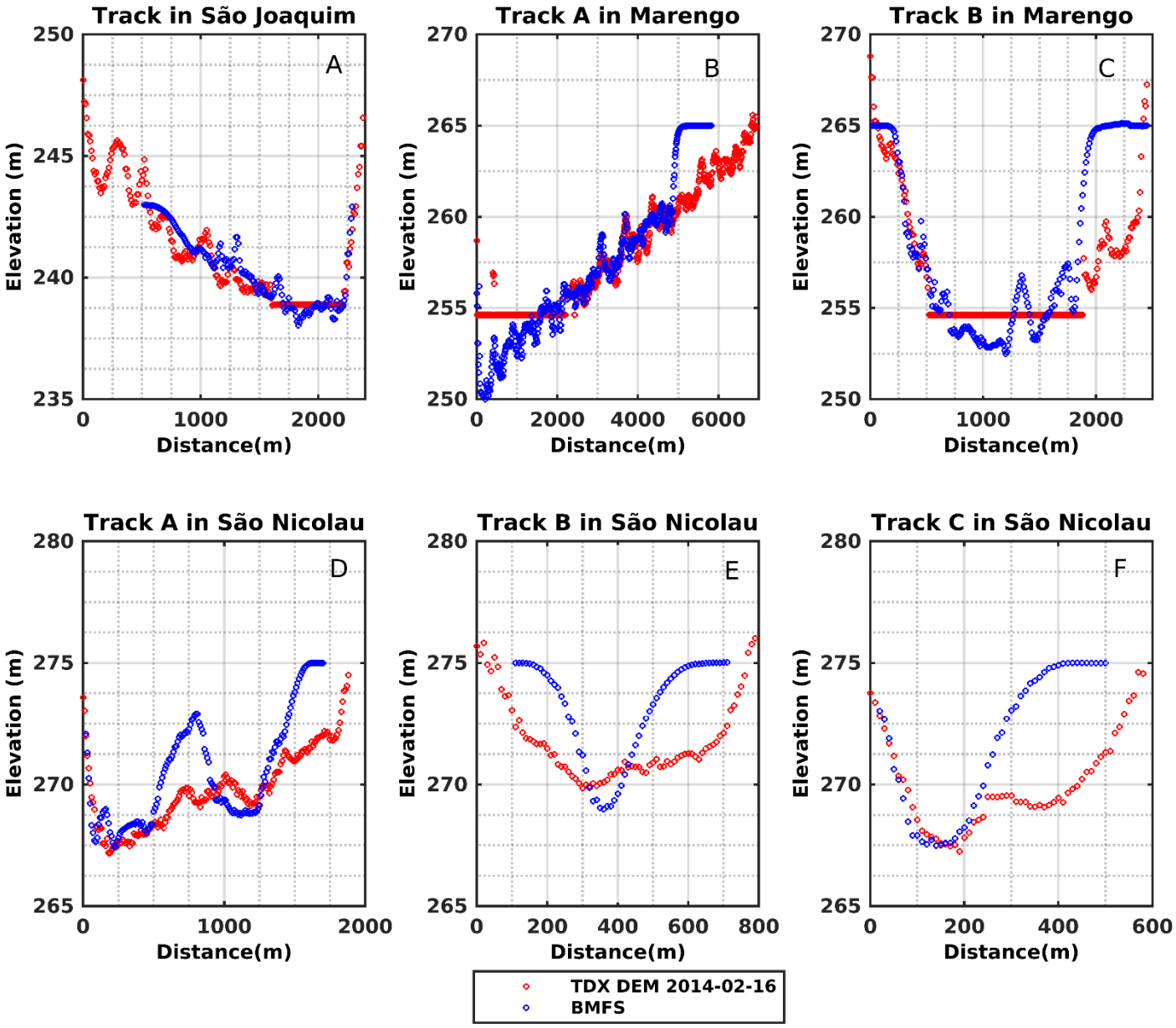

Figure 2.9 Profiles of TDX DEM 2014-02-16 and bathymetric maps derived from field survey (BMFS in the sub-figures) in three reservoirs in the Madalena catchment. The track in São Joaquim goes from west to east, track A in Marengo from south to north, track B goes from west to east (see Figure 2.8). Track A in São Nicolau goes from south (dam) to north (tail zone), while track B and C spans from west to east. The distance between neighboring samples is 20 m.

In summary, the profile comparisons of the TDX DEM and the bathymetric maps derived in field surveys evidently show differences in reservoir shapes cast by these two approaches, in addition to the coverage difference. Absence of field measurements at shallow boundaries leads

to fake flat shapes for the reservoir for these areas on thus derived bathymetric maps. TDX DEM 2014-02-16 can retrieve the bathymetry for the areas with fine structures such as the island, tails and branches. In reservoirs with few submerged macrophytes, TDX DEM 2014-02-16 and bathymetric maps derived from field survey cast similar shapes at the areas where TanDEM-X data and the field measurements overlap, e.g. Marengo and São Joaquim. However, in the case of the densely vegetated reservoir, i.e. São Nicolau, submerged macrophytes, stumps or even artifacts in the field measurements at high water level stage misshapes the reservoir on the bathymetric maps derived from field surveys. By mapping the dry bottoms of the reservoirs, TDX DEM 2014-02-16 is free of the influence from submerged macrophytes, stumps and shallow depth, and thus presents reliable shapes for the reservoirs.

2.4.4.3 Water area-to-volume relationship

The inundation area and the corresponding volume are the main inventory data for the reservoirs in the quantitative assessment of available water. The volume of the water under certain water area in a reservoir is usually estimated from a bathymetric map. In this study, the relationship between water area and corresponding reservoir volume was extracted both from TDX DEM 2014-02-16 and bathymetric maps derived from field survey. We employed this parameter to investigate the effect of different bathymetric maps in the water area-to-volume relationship extracted from them. Figure 2.10 shows the water area-to-volume relationship for São Joaquim, Marengo, São Nicolau and Fogareiro.

In São Joaquim, the comparison of the water area-to-volume relationship is limited to the coverage of the bathymetric maps derived from field survey. Within the spatial range of bathymetric maps derived from field survey, the water area-to-volume relationships extracted from both data sources for this reservoir yield nearly the same water volumes (Figure 2.10 A). The unmapped area of São Joaquim on TDX DEM 2014-02-16 was occupied by water during TanDEM-X data acquisition, but it barely impacted the water area-to volume relationship.

According to TDX DEM 2014-02-16, Marengo can expand to a larger area than the

bathymetric map derived from field survey. For the same area of water in Marengo, the bathymetric map derived from field survey indicates a larger water volume in the reservoir than TDX DEM 2014-02-16 does (Figure 2.10 B). At the initial stage of the relationship the retained water with maximal unmeasured depth of about five meters and diameter of nearly 2 000 m is the main cause (Figure 2.10 B). The volume of the unmeasured water can be obtained from the initial difference of the relationship. As the water area increases, the difference between the bathymetric map derived from field survey and TDX DEM 2014-02-16 becomes larger for Marengo. Fewer measurements near the boundaries of bathymetric map derived from field survey cast a narrower shape for the reservoir than shown in TDX DEM 2014-02-16. As a result, on this narrow bathymetric map of Marengo the corresponding water volume increases more quickly than the water area does when the water level rises (Figure 2.10 B). The flat features caused by the lack of field measurements in shallow waters impact the water area-to-volume relationship significantly in Marengo, but the impact of macrophytes may be ignored.

According to the TDX DEM 2014-02-16, the water area in the reservoir São Nicolau can expand to a similar extent as the bathymetric map derived from field survey, larger than the maximum of water extent recorded in the RapidEye archive. The water area-to-volume relationship extracted both from the bathymetric map derived from field survey and TDX DEM 2014-02-16 show significant differences (Figure 2.10 C). For the same water areas, the bathymetric map derived from field survey implies a larger water storage for the reservoir than TDX DEM 2014-02-16 does (Figure 2.10 C). Due to the different shapes casted by the two bathymetry datasets (e.g. Figure 2.10 D), a much shallower water depth on TDX DEM 2016-02-16 will occupy the same water area as that under a higher water level on the bathymetric map derived from field survey. Therefore, under the same water area the water stored in the reservoir calculated from TDX DEM 2014-02-16 is less than that obtained from bathymetric map derived from field survey (Figure 2.9 D). This phenomenon becomes more significant as the water area increases, resulting from the narrow morphology of the reservoir

caused by the lack of field measurements in the boundary areas. In this reservoir, as no water retained on 2014-02-16, no contribution from it was observed for the water area-to-volume relationship derived from TDX DEM 2014-02-16 for São Nicolau. In contrast, the emergent and submerged macrophytes and at shallow areas and the lack of field measurements in the boundary area have notably impacted the bathymetric maps derived from field surveys (Figure 2.10 D-F), as well as the water area-to volume relationship extracted from it.

A comparison of water area-to-volume relationships was also conducted for Fogareiro (Figure 2.10 D). The field data were collected during a topography survey before the construction of the reservoir, with the relative elevation given. As no water was filled during the field survey, no effect of macrophytes or shallow water depth will exist. TDX DEM 2014-02-16 is expected to indicate similar shapes as the bathymetric map derived from field survey. The water area-to-volume relationships extracted from the bathymetric map derived from field survey and TDX DEM 2014-02-16 are very similar and with a stable discrepancy as the water area increases. The volume difference of ~ 10 hm^3 between the two relationships stands for the volume of water retained in Fogareiro on 2014-02-16. In the TDX DEM 2014-02-16, ~ 1/6 of the area was unmapped and ~5% of the corresponding volume was not derived.

The effect of remained water and shape difference were shown in this subsection. The contribution of the water retained during TanDEM-X data acquisition was determined by the initial differences between the water area-to-volume relationships extracted from TDX DEM 2014-02-16 and bathymetric maps derived from field surveys. The unmapped areas in TDX DEM 2014-02-16 only impact the water area-to-volume relationships derived from them for the larger reservoirs such as Forgareiro. The volume of the water under the unmapped area is marginal in comparison to the volume under the area which was mapped by TDX DEM 2014-02-16. As the water area increases, the effect of misshaping caused by the lack of field measurements in the shallow areas emerges and increases. For the shallow reservoir São Nicolau, which was empty on 2014-02-16 but densely vegetated during field bathymetric survey in the wet season, the impact of shape differences between TDX DEM 2014-02-16 and

bathymetric map derived from field (Figure 2.10 D-F) is significant. Having mapped the dry bottom of these reservoir with continuously distributed pixels, TDX DEM 2014-02-16 reveals more reliable shapes and water area-to-volume relationships for reservoirs Marengo, São Nicolau and São Joaquim, as compared to bathymetric maps derived from field surveys.

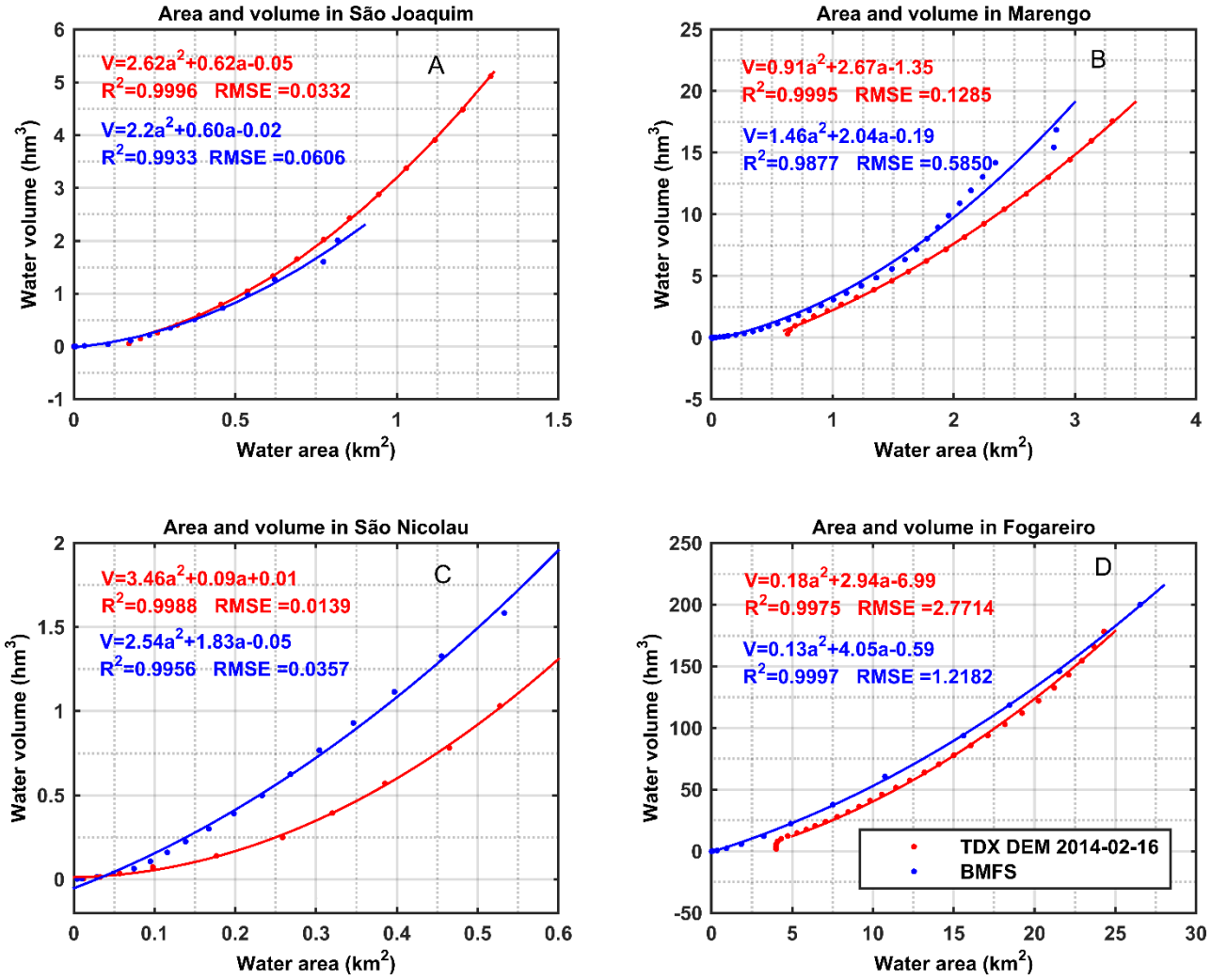

Figure 2.10 Comparisons of the water area-to-volume relationship based on TDX DEM 2014-02-16 and bathymetric maps derived from field survey (BMFS in the figures). The field water area-to-volume data of Fogareiro was provided by COGERH with water level step of 2.5 m. Other field bathymetric maps were acquired from the interpolation of the field depth measurements as stated in the data section

2.4.5 Water volume

The volume of water stored in the reservoirs in the Madalena catchment and in Fogareiro at their maximal water extents as archived by RapidEye data is listed in Table 2.4, disregarding

the small amount of retained water. Among these five reservoirs, Marengo and São Joaquim play the major role in water storage. From the water area-to-volume relationship derived from bathymetric maps derived from field survey, the volumes of water retained in Marengo, São Joaquim and Fogareiro on 2014-02-16 were ~0.92 hm^3, ~0.00 hm^3 and ~10 hm^3, respectively, corresponding to 5.09%, 0.02%, and 5.00% of the achievable total storage capacities. These values were calculated from the relationships when the area equals the first value on the water area-to-volume relationship derived from TDX DEM 2014-02-16.

Table 2.4 Areas and volumes of water stored in the reservoirs under the maximal water extent archived.

	Marengo	São Joaquim	São Nicolau	Raiz	Mel	Madalena catchment	Fogareiro
Area (km^2)	3.37	1.30	0.57	0.28	0.09	5.61	24.31
Ratio of area to total %	60.07	23.17	10.11	4.93	1.65	-	-
Volume (hm^3)	18.58	5.53	1.31	1.04	0.20	26.14	178.23
Volume accuracy (%)	21.8	29.3	59.4	33.6	53.3	-	15.83
Volume ratio of total %	71.08	21.15	5.01	3.98	0.77	100	-

DEM generated from TanDEM-X data with single pass interferometry can reach an accuracy of about one meter. Despite the accuracy of individual measurements, shallow water depth, incomplete water coverage, uneven distribution of the field measurements, the presence of dense emergent and/or submerged macrophytes and artifacts in the field survey can all undermine the quality of bathymetric maps derived from field survey. Contrastingly, the TDX DEMs can map all the coherent areas (coherence > 0.6 in this study) under the TanDEM-X image coverage with evenly distributed pixels, including the water-free areas. The evenly distributed measurements of SAR data in water-free areas replicates the more reliable shape for the reservoirs in the TDX DEM, and thus reflects the more reliable water area-to-volume relationship. As for the water remaining in some reservoirs, its contribution to the reservoir volume is very slight in the case of the Madalena catchment area, compared to the total volumes.

2.5 Discussion

In this study, DEMs were separately generated from three bistatic TanDEM-X data sets with single-pass interferometry. The TDX DEMs were compared with one another, validated with field DGPS data, and their accuracies were assessed. Among the three TDX DEMs, TDX DEM 2014-02-16 shows the smallest water areas in the reservoirs thus was selected to reveal the reservoir topography. It is then compared to bathymetric maps derived from field survey.

The elevation differences between the TDX DEMs range from -2 m to +2 m with mean at zero meter, which demonstrates the reliability of the TDX DEM generation workflow. Land use changes in the three years between the data collections (i.e. 2011 and 2014) and seasonal differences (February, March and July) are regarded as the cause for these elevation differences in the range of one to two meters. According to Krieger et al. (2007), vegetation five meters high could introduce an elevation error of 1-1.5 m in the TDX DEMs. In 2011 the TanDEM-X data were acquired in the wet season when the canopy of the vegetation is closed, and more volume decorrelation is possible. This might explain the elevation variation beyond the range of -2 m to +2 meter in the comparison of maps of DEMs from TanDEM-X data acquired in 2011 and 2014. TDX DEM 2014-02-16 and TDX DEM 2014-03-21, which were respectively generated from TanDEM-X images acquired 33 days apart, show overall smaller differences from each other (i.e. mostly within -1 to +1 m) (Figure 2.6 C).

The results in Table 2 show that the accuracies of the TDX DEMs in the Madalena catchment area are of the order of one meter, higher than the overall accuracies of the global TanDEM-X DEM (TanDEM-X ground segment, 2013). This is probably because the overall accuracies of the global TanDEM-X DEM were given based on the global scale, covering multiple ground topographies and land uses. In addition, TanDEM-X data acquired in different seasons are used for the global DEM generation. On the other hand, the accuracy derived in this study may only apply to the TDX DEMs from bistatic TanDEM-X data over this specific area, which is characterized by relatively flat terrain (Figure 2.1 C) and covered by deciduous shrubs. It is

possible that the same processing of data with similar acquisition for other areas will yield TDX DEMs with a certain difference, depending on the specific terrain and land cover. Field DGPS data were collected from bare land without tree coverage, similar to the situation at the bottom of water-free reservoirs. Thus, the accuracy is assumed to be acceptable for water volume assessment in reservoirs.

We used the generated TDX DEM in the reservoirs areas to reveal the reservoir bathymetry. The approximate one-meter accuracy of the TDX DEMs is slightly worse than the 0.89 m of the bathymetric map derived by Pacheco et al. (2015) and 0.67 m by Brando et al. (2009) from spectral reflectance of water columns. Although mainly applied in coastal regions, methods based on spectral characteristics can map inland water bathymetry. However, the accuracy of the bathymetric maps derived with such methods varies with the water turbidity/clarity (Brando et al., 2009), and so do the accuracies of the bathymetric mapping from LiDAR measurements (Guenther et al., 2000). In contrast, the accuracies of TDX DEM are relatively stable within the TanDEM-X scene, and thus in the study catchment.

Moreover, derivation of bathymetric maps from optical remote sensing requires images acquired in cloud-free conditions and is constrained limited water depths e.g. 4-13 m (Brando et al., 2009; Lafon et al., 2002; Pacheco et al., 2015; Sandidge and Holyer, 1998). Even though, these methods are capable of mapping large-scale coastal areas within the retrievable water depth, in spite of the smaller test sites of kilometers. LiDAR measurements can also map water bathymetry with very high accuracy and resolutions smaller than one meter, but their application in bathymetric mapping is often constrained into the small scale of sub-kilometers. The expense is another factor that concerns its application for large scale mapping. In contrast to those methods, DEMs, which are derived from TanDEM-X data acquired in the dry seasons with minimum water retention, can map the water-free areas in all the reservoirs under its coverage, independent of weather conditions, water quality (i.e. turbidity, etc.) and depth. For example, TDX DEM 2014-02-16 maps the São Nicolau with a complete depth of seven meters, the major part of Marengo with depth around ten meters and the majority of Fogareiro.

Shallow areas and fine structures of reservoirs (e.g. branches and tails) in northeastern Brazil are usually vegetated by macrophytes and thus not accessible for field measurements. As a result, sparse and inadequate field measurements in these areas can cause inaccurate, misshapen bathymetric maps for the reservoirs, e.g. São Nicolau and Marengo (Figure 2.9). Considering their usually small sizes, reservoir branches are prone to problems in terms of mixed-pixels when the data of coarse resolution such as Landsat are used. With the high spatial resolution of the TanDEM-X data, very detailed reservoir bathymetry can be derived with evenly distributed pixels on TDX DEM. Furthermore, compared to bathymetric maps interpolated from water/land borders extracted from time series of images (Arsen et al., 2013; Feng et al., 2011), TDX DEM is free of misclassification effects.

Macrophytes have an impact on the performance of the bathymetric maps derived for inland waters. Massive aquatic grasses can disturb the spectral reflectance from the water surface. According to Dierssen et al., (2003), the magnitude of the retrieved bottom reflectance, which is used to derive ocean bathymetry, is highly correlated to the seagrass leaf area index ($r2 = 0.88$). Stumps and submerged macrophytes affect the point-wise bathymetric mapping with LiDAR (Guenther et al., 2000) and field depth measurements by reflecting the wrong depth of waters being measured. In the TDX DEM over the reservoirs, the extent of the vegetation in waters can be minimized by acquiring the TanDEM-X data in the dry season. As for the effect of those macrophytes growing in and/or along the waters retained during the TanDEM-X image, overestimating the extent of retained water from coherence map can eliminate it. However, this is the case only for reservoirs with water retention during the TanDEM-X data acquisition in the dry season. For empty reservoirs it is not even necessary. In this study, we did not consider the impact of macrophytes in water on the TDX DEM, as we are relying on TDX DEM simply to study the bathymetry of the dry part of the reservoirs.

We extracted the water area-to-volume relationship for the reservoirs from both TDX DEM 2014-02-16 and the bathymetric maps derived from field survey. These relationships were used to further investigate the effect of the retained water and other factors influencing the field

measurements. Dense submerged macrophytes and the lack of measurements at shallow areas of the reservoirs can significantly affect the water area-to-volume relationship from bathymetric map derived from field surveys. As TDX DEM 2014-02-16 mapped the reservoirs in the dry season when hardly any vegetation emerged in the reservoirs, water area-to-volume relationships obtained from TDX DEM 2014-02-16 for the reservoir were found to be more reliable. Compared to the reservoir storage curves obtained from time series of optical images (Peng et al. 2006) and the volumes estimated for big reservoirs from MODIS data and altimetry data (Zhang et al., 2014), the effect of misclassification for water/land border extraction is eliminated by extracting the inundation area with the same water level intervals (i.e. 0.5 m) from TDX DEM 2014-02-16. The extraction of water area-to-volume relationship from TDX DEM is less dependent on the number of optical images available in the archive. According to Heine et al. (2014), the water areas in reservoirs in another catchment in the Ceará state do not vary spatially synchronously. This is very likely also the case in the Madalena catchment. Once the water extents in the reservoirs are obtained from remote sensing images for a certain time, the total water volume stored in the Madalena catchment at that time can be derived from the water area-to-volume relationships of the reservoirs. If applied on a regional scale such as for Ceará State, this method can help in understanding the dynamic amount of water stored in the region or in a large hydrological unit and in managing local water resources. For example, with the maximal water extent recorded in the RapidEye data archive, the potential water storage in the Madalena catchment reservoirs was estimated to be 26.14 hm^3, disregarding the retained water.

The corresponding accuracies of the estimated water volume was retrieved for each reservoir using equation (2.2), independent of field measurements. This also quantifies the accuracies of the water storages estimated for the reservoirs, if it is applied in the water volume related study or for water resources management. Despite the presence of retained water, the water volumes estimated from TDX DEM 2014 -02-16 are higher than those derived from bathymetric maps derived from field survey, thanks to the excellent performance of TDX DEM 2014-02-16 in the

reservoirs mapping (Figure 2.8 and Figure 2.9).

However, an empirical threshold value of 0.6 was adopted in this study to overestimate the water area. Although within the tolerance of the overall coherences of the interferograms derived from the TanDEM-X images used, this value is site-specific and much higher than those adopted in other studies for open water masking. Therefore, when applying this approach in other areas, it may be necessary to introduce some adjustments on the threshold of the coherence according to the local conditions such as the type and coverage of aquatic vegetation. Alternatively, reliable information on real-time water extents obtained from other sources is also an option. In addition, the maximal water extents recorded in the RapidEye data archive are possibly not the real upper limit of water extent in the reservoirs. The storage capacities estimated here for the reservoirs might be slightly lower than the real values. This limitation can hopefully be improved by introducing the real elevations of the spillways or the real maximum inundation area delineated based on a longer time-series of images with frequent data acquisition. Finally, in this study the coordinates of the field measurements were given by the handheld GPS, and their accuracy is approximately five meters and thus well below the pixel spacing of the TDX DEMs. However, when the accuracy of the handheld GPS is in the order of the pixel spacing of the TDX DEMs, the similarity between the accuracy of GPS and pixel spacing needs to be considered in the comparison.

2.6 Conclusion and outlook

The DEMs generated from TanDEM-X data with single pass interferometry can achieve approximately one-meter absolute accuracy in the Madalena region in north-eastern Brazil. We used this TDX DEM acquired in the dry reservoirs to represent the bathymetry for the reservoirs. Compared to bathymetric maps derived from field survey data, the TDX DEMs have shown advantages for the reservoir bathymetric survey with respect to the larger coverage, even distribution of measurements, and independence of the disturbance from macrophytes in the wet season. TDX DEMs were found to better replicate the reservoirs' shapes and to provide

more reliable water area-to-volume relationships for the reservoirs. The water retained during TanDEM-X image acquisition was found to have little impact on the derived reservoir bathymetry and water volumes for the reservoirs. TDX DEMs allow an efficient reservoir bathymetric survey, especially in remote areas.

One might argue that the demand for adequate TanDEM-X data, i.e., ideally acquired during dry season without remaining water, is a limitation of the approach. However, our results demonstrate that the retained water during data acquisition has little impact on the derived reservoir bathymetry as well as on estimated water volumes. Moreover, the high repetition rate of TanDEM-X supports the acquisition of adequate data. However, the approach is limited to areas with significant water volumetric fluctuation and temporarily exposed reservoir bottoms. Flat terrain is also an important factor to ensure a high accuracy of the TDX DEMs and thus, the derived reservoirs' bathymetric maps. In this study, the water areas were overestimated with an empirical threshold on the coherence map. For a more efficient water masking, other suitable approaches would be worth investigating.

The proposed approach is particularly interesting for regions that are characterized by a very high number of water bodies, such as our study site in Ceará. Contrary to a remote sensing-based approach, common bathymetry mapping would result in very time and cost consuming field surveys. In general, the approach can support regional water, sediment and ecological management in any dryland areas with similar conditions. However, when applied in large areas of several thousand square kilometers, the terrain and land cover heterogeneity need to be considered to obtain a high overall DEM accuracy.

3. Mapping effective water surface in macrophyte-covered reservoirs in NE Brazil based on TerraSAR-X time series

Abstract: Water supplies in northeastern Brazil strongly depend on the numerous surface water reservoirs of various sizes there. However, the seasonal and long-term water surface dynamics of these reservoirs, particularly the large number of small ones, remain inadequately known. Remote sensing techniques have shown great potentials in water bodies mapping. Yet, the widespread presence of macrophytes in most of the reservoirs often impedes the delineation of the effective water surfaces. Knowledge of the dynamics of the effective water surfaces in the reservoirs is essential for understanding, managing, and modelling the local and regional water resources.

In this study, a two-year time series of TerraSAR-X (TSX) satellite data was used to monitor the effective water surface areas in nine reservoirs in NE Brazil. Calm open water surfaces were obtained by segmenting the backscattering coefficients of TSX images with minimum error thresholding. Linear unmixing was implemented on the distributions of gray-level co-occurrence matrix (GLCM) variance in the reservoirs to quantify the proportions of sub-populations dominated by different types of scattering along the TSX time series. By referring to the statistics and the seasonal proportions of the GLCM variance sub-populations the GLCM variance was segmented to map the vegetated water surfaces. The effective water surface areas that include the vegetation-covered waters as well as calm open water in the reservoirs were mapped with accuracies > 77%. The temporal and spatial change patterns of water surfaces in the nine reservoirs over a period of two consecutive dry and wet seasons were derived. Precipitation-related soil moisture changes, topography and the dense macrophyte canopies are the main sources of errors in the such-derived effective water surfaces. Independent from in-situ data, the approach employed in this study shows great potential in monitoring water surfaces of different complexity and macrophyte coverage. The effective water surface areas obtained for the reservoirs can provide valuable input for efficient water management and improve the hydrological modelling in this region.

Keywords: TerraSAR-X, GLCM variance, effective water surface, macrophyte-covered reservoirs, semiarid region, northeastern (NE) Brazil

3.1 Introduction

Knowledge of water bodies covered by vegetation and their water dynamics is vital for understanding local to regional ecology and hydrology (Alsdorf et al., 2000; Capon, 2003; Colloff and Baldwin, 2010; Roshier et al., 2002). In the semiarid region in NE Brazil, aquatic vegetation abundantly present in many surface water reservoirs as an indicator of water quality variation. Mapping these water bodies by field survey is labor consuming and challenging due to the impediment of dense macrophytes on the accessibility to these areas.

Available satellite data have continuously increased and opened up substantial opportunities for water surface mapping from space (Douglas E. Alsdorf et al., 2007; Alsdorf and Lettenmaier, 2003; Palmer et al., 2015). Based on the spectral characteristics of water bodies, optical images have been widely used to map the open water characteristics and their changes (Donchyts et al., 2016; Mohammadi et al., 2017; Pekel et al., 2016). Due to its independence of sun illumination and thus weather, Synthetic aperture Radar (SAR) data have been increasingly applied in the mapping and monitoring of water surfaces and water environments. Calm open water surfaces, acting as specular reflectors, reflect away nearly all the incident SAR pulses and thus appear black in SAR images. Based on this characteristic, various methods have been developed for mapping open water surfaces such as flooding using SAR data sets. SAR data acquired with different polarizations, wavelengths and incidence angles etc. were also investigated (Eilander et al., 2014; Horritt et al., 2003; Klemenjak et al., 2012; Li et al., 2014; Martinis et al., 2015a; Schlaffer et al., 2015; Wendleder et al., 2013).

However, in landscapes like wetlands, marsh lands and alike, open water always fail to represent the complete water surface, as in these areas a large proportion of the water surface is often covered by vegetation. Therefore, it can be challenging to map the effective water surface, consisting of open water and vegetation covered water surfaces. In many studies spectral indices

such as vegetation and water indices were used to map the inundations in wetlands (Ahamed and Bolten, 2017; Feng et al., 2012; Gonzalez-Dugo et al., 2014; Li et al., 2015a; Thomas et al., 2015). Based on spectral indices and LiDAR data, Lang and McCarty (2009) developed a model to describe the characteristics of inundation in wetlands. This model has been applied to map the inundations in wetlands with optical data (Huang et al., 2014; Jin et al., 2017). However, vegetation indices tend to overestimate the water surface, when the surrounding terrestrial vegetation shows similar spectral characteristics during the leaf-on seasons (Toeyrae et al., 2001). Therefore the inundation mapping with spectral vegetation characteristics is often limited to the leaf-off season (Huang et al., 2014; Jin et al., 2017). Employing water indices could introduce underestimation of the effective water surfaces, as the vegetated waters are not taken into account. Cloud coverage poses another obstruction to the application of optical data. Capable of penetrating vegetation canopy, SAR data have served as a powerful alternative for mapping waters beneath vegetation. On vegetated water surfaces the incident SAR pulses bounce between the water surface and the vertical tree trunks or standing stalks of emergent plants and reflect more SAR pulses back to the sensors than the surroundings. Therefore, vegetated water surfaces appear much brighter than the surroundings on a SAR image (Hess et al., 1990; Richards et al., 1987; Silva et al., 2008). Based on this knowledge, mapping of water surfaces beneath vegetation has been undertaken with various SAR data in circumstances including flooded forests, wetlands and marsh land (Hess et al., 1995; Kim et al., 2014; Lang et al., 2008; Lee et al., 2012; Marti-Cardona et al., 2013, 2010; Pulvirenti et al., 2013; Schlaffer et al., 2017). Descriptive studies have established the characteristics of difference species at different stages and canopy density (Dobson et al., 1995; Hess et al., 1995; Kim et al., 2014). Supervised and object-oriented classification approaches have been frequently adopted with assistance of substantial field data (Bourgeau-Chavez et al., 2001; Evans and Costa, 2013). Models have been developed and applied to understand the SAR backscatters of flooded forests (Cohen et al., 2016; Kasischke et al., 2003). It has been demonstrated that double bounces, specular reflectance, and volumetric scattering in the canopy constitute the backscatters of flooded forests in SAR images (Cohen et al., 2016; Hess et al., 1990).

The brightness of flooded forest is proved to be related to the height and canopy density of the vegetation (Cohen et al., 2016). However, the majority of these studies tend to target at few timestamps with in-situ data available. Suitable for mapping short-term events like flooding, yet, these studies are not applicable for long-term mapping of effective water surfaces in environments like wetlands and marshlands. Moreover, knowledge of few scenarios is not sufficient to recover the temporal development in the targeted water environment. The compositions of the vegetation in a water environment are complex and vary among study sites and throughout seasons. Therefore, the studies on mappings of waters beneath vegetation with SAR backscatters are rather site-specific and strongly dependent on available field data. As acquiring continuous and extensive field data is not realistic, a field data independent approach is necessary for a continuous monitoring with multi-temporal remote sensing data.

Studies have proved that including texture information can enhance the image analysis in the aspects of ground object identification and land use classification (Ban et al., 2014; Esch et al., 2013; Proctor et al., 2013; Stasolla and Gamba, 2008; Uhlmann and Kiranyaz, 2014). Among these studies, urban area mapping has achieved prominent results due to the fundamental characteristic of double bounces between the buildings and the ground (Ban et al., 2014; Esch et al., 2013). Analogous to the interaction between the penetrating SAR pulses and plant trunks or stalks, double /multiple bounces are expected from the water surface covered by vegetation. Therefore, it is worth investigating the potential of texture indices for mapping the water surface covered by vegetation. Moreover, to the authors' best knowledge, SAR texture indices have rarely been used to map the vegetated water surfaces.

In northeastern (NE) Brazil, many reservoirs are covered by macrophytes to various extents. In-situ monitoring of the effective water surfaces is often infeasible, due to the large number of the reservoirs and the remoteness of the region. However, knowledge of the effective water surfaces in reservoirs is vital for efficient water management.

In this study we investigated the potential of multi-temporal TSX data and GLCM texture for

mapping the effective water surfaces in reservoirs. The approach which includes mapping of both open water surfaces and the vegetated water surfaces was applied to nine reservoirs. In-situ data were used to validate the results. The effective water surfaces were mapped for marginally and largely vegetated reservoirs over two consecutive dry and wet seasons, i.e., considering reservoirs under various conditions in terms of water levels, macrophyte growth stages and terrestrial vegetation coverage.

3.2 Study area

Since the 19th century, numerous reservoirs have been constructed in NE Brazil. Monitoring these water bodies has been inconsistent, resulting from managements by different country, federal state and local municipality organizations (SIRH/Ce, 2015). In general, large reservoirs supported by the federal state and country are regularly monitored and maintained because of their strategic importance. In contrast, numerous reservoirs of small to medium size and/or at remote areas are poorly monitored (SIRH/Ce, 2015). However, those relatively small reservoirs actually play an eminent role in the runoff retention in the upstream parts of the catchments and act as the only water suppliers to the population in rural areas (Peter et al., 2014).

The Madalena region is in the central part of the federal state of Ceará (Figure 3.1). The local climate is semiarid with pronounced wet and dry seasons. From January to June is the wet season when the major precipitation events take place; the dry season spans from July to December. The average annual precipitation is approx. 600 mm, and the potential evaporation exceeds 2000 mm per annum. Caatinga, an endemic seasonal shrubby forest landscape in NE Brazil (Bullock et al., 1995), is the dominant land cover. The unevenly distributed precipitation in the wet and dry seasons, the intensive evaporation and water consumption have led to significant fluctuations in the water levels in the reservoirs throughout the year. This is a typical phenomenon for the reservoirs in NE Brazil. Reservoir monitoring in the Madalena catchment was undertaken only recently by the Federal University of Ceará (UFC), basically by means of in-situ investigation in a few accessible reservoirs. So far, there are only few remote sensing studies aiming at reservoir

mapping in this region, e.g. Zhang et al. (2016) or for a similar area (Heine et al., 2014). Reservoirs in this region are covered by macrophytes to various extents. In some reservoirs, even the majority of the water surfaces are covered. *Pistia stratiotes L., Salvinia auriculata, Nymphaea alba, Ludwigia helminthorrhiza* and *Lemna valdiviana* are the most frequently noticed floating macrophytes in those reservoirs. The frequently found emergent macrophytes are *Paspalidium geminatum, Oxycarium cubense, Paspalum vaginatum* and *Polygonum ferrugineum*. In the Madalena region, floating macrophytes are mainly found in the reservoirs Paus Branco, Nova Vida 1, Nova Vida 2, and one anonymous reservoir labeled as NN1 (Figure 3.1). As this investigation only considers the macrophytes that intervene the interaction between the water surface and incident SAR pulses, submerged macrophytes are excluded from the scope of this study.

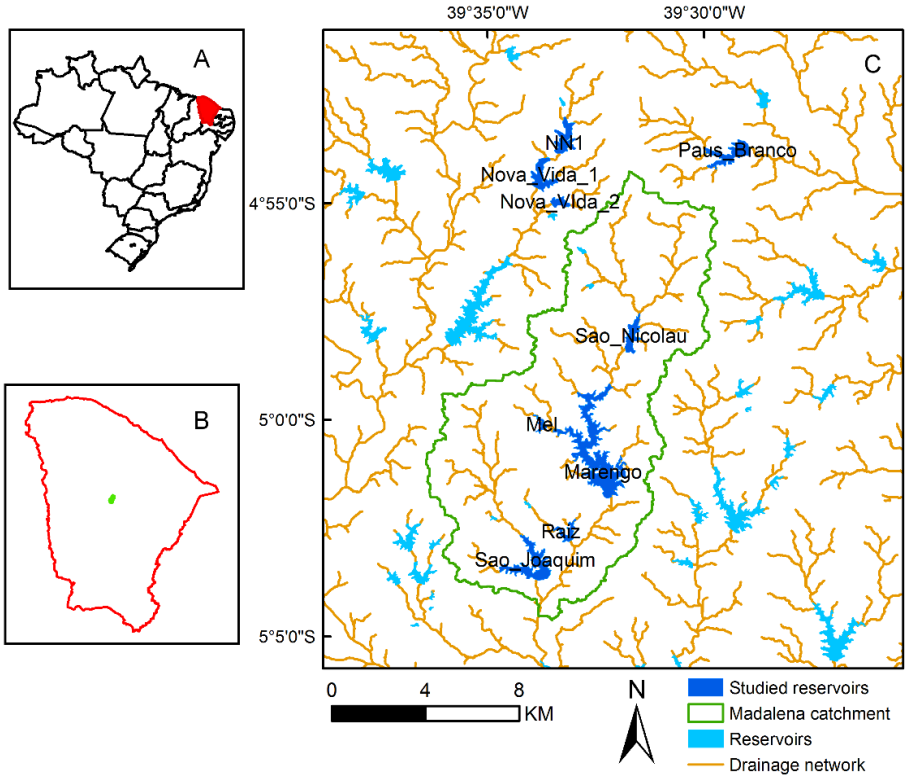

Figure 3.1 Location of the study area. A: location of the State of Ceará in Brazil, B: location of the Madalena catchment in the State of Ceará, C: locations of the studied and the neighbouring reservoirs.

This study focuses on nine reservoirs, namely Marengo, São Joaquim, São Nicolau, Raiz, Mel, Paus Branco, Nova Vida 1, Nova Vida 2 and NN1 (Figure 3.1) with respective areas of 3.39 km^2,

1.20 km^2, 0.49 km^2, 0.25 km^2, 0.09 km^2, 0.81 km^2, 0.62 km^2, 0.21 km^2, and 0.65 km^2. Because in the Madalena catchment São Nicolau is the only reservoir that was noticeably covered by macrophytes, the reservoirs Nova Vida 1, Nova Vida 2, Paus Branco and NN1 with substantial vegetation appearance were included. Those reservoirs consist of two types, with and without significant presence of macrophytes. Figure 3.2 shows some field views on the macrophytes coverage in both the marginally and largely vegetated reservoirs in the Madalena region.

Figure 3.2 Field impressions of macrophyte coverages in the reservoirs Marengo (A), Sao Joaquim (B) São Nicolau (C), Nova Vida 2 (D), Nova Vida 1 (E) and Paus Branco (F).

3.3 Data and method

3.3.1 Data

Overall 37 TSX data sets were acquired to cover the study area from February 2014 to September 2015 (17 images in 2014 and 20 in 2015). The TSX data were acquired in the strip map mode with HH polarization. Each TSX scene covers an area of 30×50 km². The delivered TSX data were processed to be Enhanced Ellipsoid Corrected (EEC), with radiometric enhancement. Further data parameters are listed in Table 3.1. The nominal revisit time of TSX satellites is 11 days. Due to the conflicts between data acquisitions for the TSX and the TanDEM-X data missions, there are two one-month gaps in the time series. A few failures in data downlink also resulted in small gaps in the time series.

Table 3.1 The parameters of the TSX data employed in the study.

Orbital direction	Over pass time (UTC00)	Incidence angle (degree)	Pixel spacing (m)	Resolution (m)	Orbit	Beam	No. of acquisitions
Descending	8:25	30.0	2.75	7	110	007	37

A total of 11 acquisitions of RapidEye satellite images, delivered in level 3A, were employed in the study (Figure 3.3). Frequent cloud cover in the rainy season constrained the majority of RapidEye data in the dry season. RapidEye images were used to delineate the floating macrophyte areas, as well as to illustrate the results.

In-situ water contours were obtained with a Garmin X handheld GPS by walking along the accessible water/bank borders. Water contours collection was conducted at five dates (Figure 3.3). However, dense terrestrial vegetation and emergent macrophytes have impeded access to the reservoir shorelines in the wet seasons and caused the unavailability of in-situ data at some of the five dates for some reservoirs.

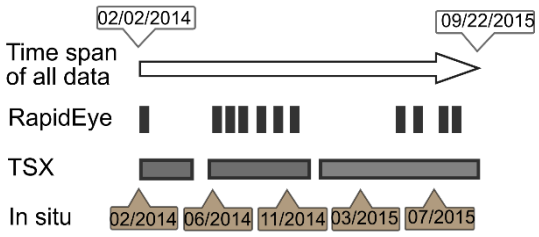

Figure 3.3 Illustration of the satellite data acquisition and in-situ data collection

3.3.2 Method

3.3.2.1 Background and assumption

Mainly three types of scattering take place on a vegetated water surface: specular reflection, diffusive/volumetric scattering and double/multiple bounces, with the strength in an ascending order (Cohen et al., 2016; Ferrazzoli and Guerriero, 1995; Horritt et al., 2003; Ormsby et al., 1985; Ramsey, 1995) All other types of scattering are formed on rougher surfaces can return SAR pulses of various intensities. In a macrophyte-covered reservoir in NE Brazil illustrated in Figure 3.4 A, open water surfaces present the specular reflection (SR); the water surfaces vegetated by large emergent macrophytes with penetrable canopies present double bounces (DB), and multiple bounces (MB) as the density increases; volumetric scatterings (VS) take place on the rough surfaces covered by dense plants, including vegetated banks, water surfaces covered by floating macrophytes or emergent macrophytes of closed canopy. All these scatterings are present in a reservoir both sole and combined forms. Specifically, banks covered by both tall and short terrestrial plants can present the combined scattering of the double bounce and the volumetric scattering (DB+VS). Water surfaces vegetated by very sparse short vegetation and the bald bank caused by over grazing can present the combined scattering of specular refection and volumetric scattering (VS + SR). In total, we expect the above six types of scattering in the reservoirs in NE Brazil.

Both of the vegetation conditions on the bank and in water evolve along with the season. For

example, the density and height of emergent macrophytes in the wet season differ from that in the dry season (Lee et al., 2012). The area ratio of bank to water also varies as the water surface expands or retreats. Moreover, variations in the water levels may alter the length of transmission paths and the strength of the returned SAR pulses (Kasischke et al., 2003; Kim et al., 2014; Kevin O. Pope et al., 1997; Pulvirenti et al., 2011). The consequence of these factors is that, within the extent of a macrophyte-covered reservoir, the proportions of different types of scattering vary throughout the year. Because the scattering taking place in a pixel is independent from that in the neighboring pixels as illustrated in Figure 3.4 A, a sufficiently small subset of the reservoir can represent the sub-population dominated by scattering of a certain type (Figure 3.4 C-F). For the same reason, the distribution of the backscattering on a SAR image is the linear sum of all the sub-populations.

Let's assume that each sub-population (i.e., surface dominated by one type of scattering within a reservoir) is characterized by a specific backscattering measure, the backscattering distribution of the entire reservoir can be described by a linear sum of the backscatter sub-populations:

$$H = \sum_{i=1}^{n} H_i * P_i \qquad (3.1)$$

where H is the distribution of the population of backscattering index (e.g. backscattering coefficient, intensity, and texture indices) in the entire reservoir, excluding open water; H_i is the distribution of the i^{th} backscattering index sub-population dominated by one scattering illustrated in Figure 3.4 A, excluding the open water; P_i is the proportion of the corresponding sub-population H_i and $\sum_{i=1}^{n} P_i = 1$; and n is the number of the total sub-populations.

As double and multiple bouncing mainly take place in the vegetated water surface, if the sub-populations dominated by these two types of scattering can be distinguished from the rest, then the vegetated water surface can be delineated for a reservoir from an image.

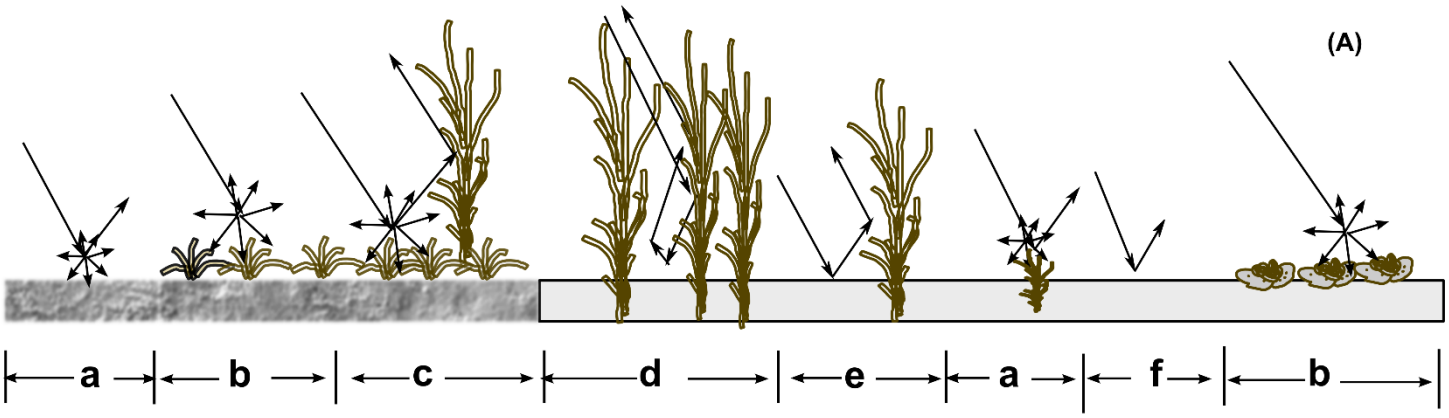
(A)
a
b
c
d
e
a
f
b

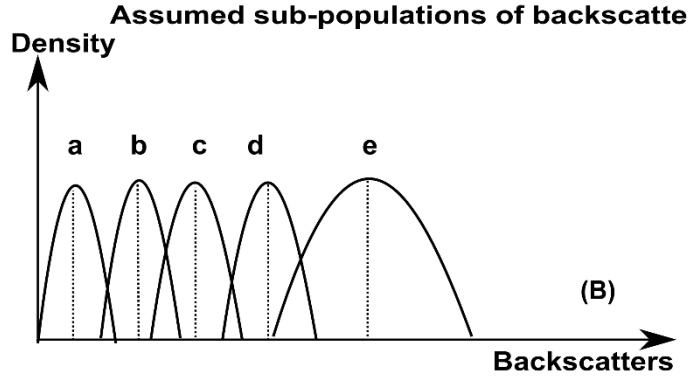
Assumed sub-populations of backscatters
Density
a
b
c
d
e
(B)
Backscatters

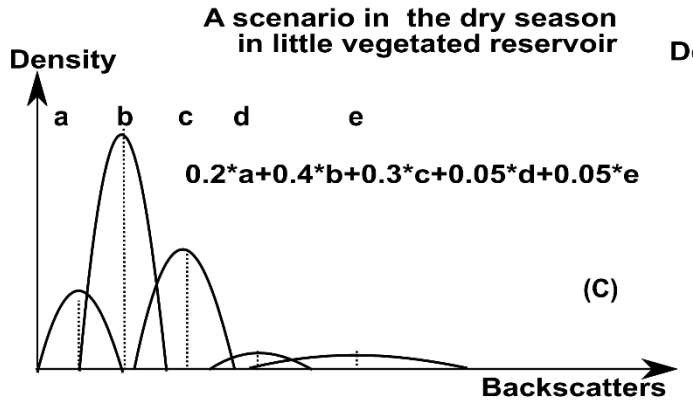
A scenario in the dry season
in little vegetated reservoir
Density
a
b
c
d
e
0.2*a+0.4*b+0.3*c+0.05*d+0.05*e
(C)
Backscatters

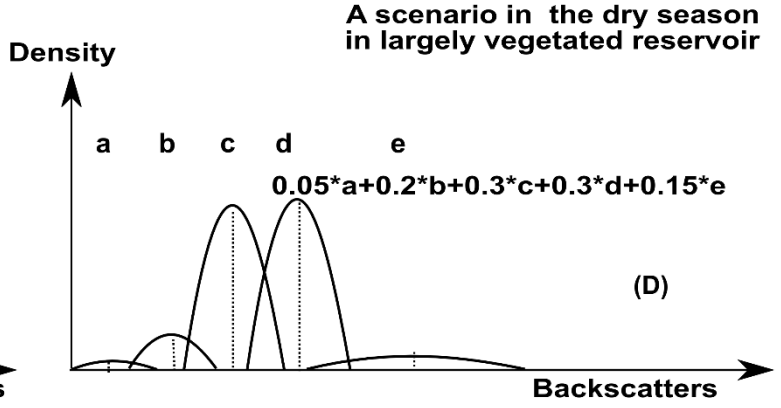
A scenario in the dry season
in largely vegetated reservoir
Density
a
b
c
d
e
0.05*a+0.2*b+0.3*c+0.3*d+0.15*e
(D)
Backscatters

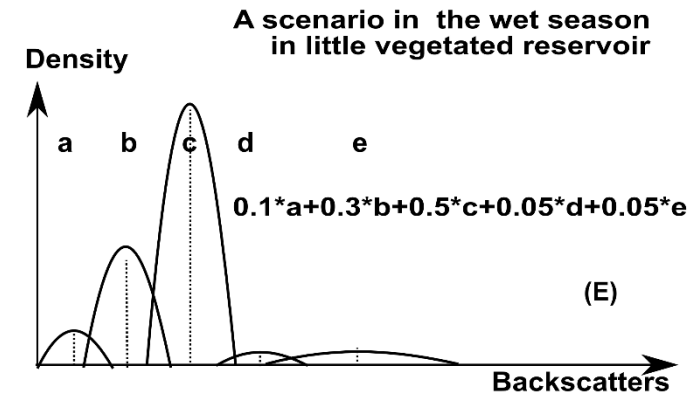
A scenario in the wet season
in little vegetated reservoir
Density
a
b
c
d
e
0.1*a+0.3*b+0.5*c+0.05*d+0.05*e
(E)
Backscatters

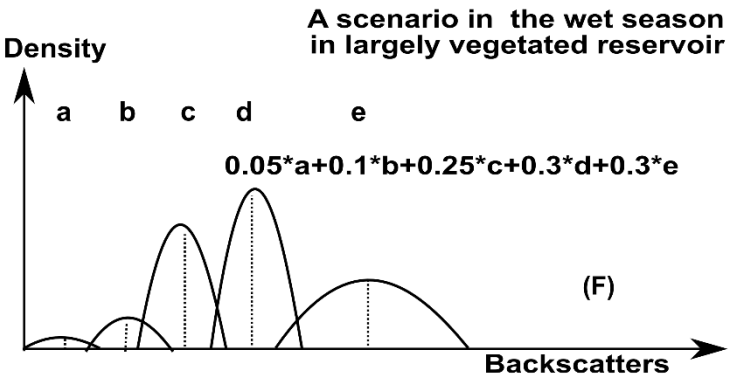
A scenario in the wet season
in largely vegetated reservoir
Density
a
b
c
d
e
0.05*a+0.1*b+0.25*c+0.3*d+0.3*e
(F)
Backscatters

Figure 3.4. Different SAR scattering and the proportions of the sub-populations dominated by them in different types of reservoirs in different seasons. A. Different SAR scattering resulting from interactions between the incident SAR pulses and ground objects within the reservoirs: From the weakest backscattering intensity to the strongest are: f, SR on calm open water surface ; e, DB from the vegetated waters; d, the MB on the water surfaces vegetated by the macrophytes of increased canopy closure; c, DB + VS on the bank covered by dense vegetation; b, VS on the densely vegetated surfaces in reservoir; a, VS + SR on bare land and the water surface sparsely vegetated by short grass-like macrophytes. Sub-plots C – F illustrate the seasonal variation of the proportions of the sub-populations dominated by different types of scatterings, excluding open waters which barely return any SAR signals.

3.3.2.2 Remote sensing data preprocessing

One RapidEye image without cloud presence was selected as the master image and laterally shifted to 26 DGPS points measured in the field at identifiable locations The rest of the RapidEye images were co-registered to the master image using AROSICS software developed by Scheffler et al. (2017). The co-registration accuracy is one pixel. The images of the TSX time series were co-registered with the same approach.

Radiometric calibration was subsequently conducted on the TSX data by following the instruction for TSX calibration provided by DLR (Infoterra an EADS Astrium company, 2008). The TSX data were calibrated to the sigma naught in decibel (dB). The TSX images of backscattering coefficients were subsequently filtered in a moving window of 3×3 pixels with adaptive Lee filter (Lee, 1980).

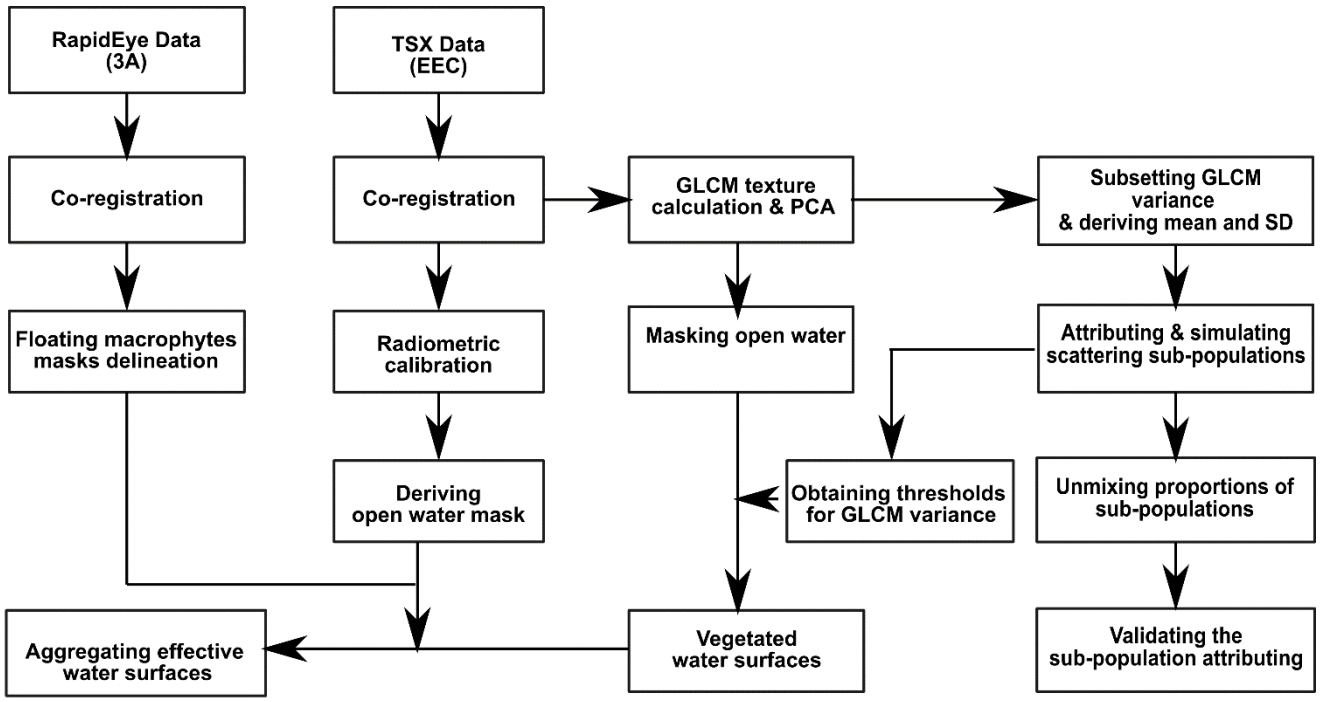

Figure 3.5 The workflow followed in the study.

3.3.2.3 Mapping open waters

In contrast to calm open water surfaces which barely return any transmitted SAR pulses to the sensor, the non-open water areas with rougher surfaces can reflect more transmitted SAR pulses back to the sensors and appear bright in a SAR image. The distribution of a population formed by these two sources of comparable sizes will present bimodality, i.e. with a significant valley in between. A minimum error thresholding algorithm developed by Kittler and Illingworth (1986) to effectively segment populations of bimodality, has been proved to be successful and fast in open water and water related change delineation (Bazi et al., 2005; Martinis et al., 2015a). Splitting the image of potential bimodality was one effective approach to mitigate the population size contrast between open waters and the surroundings, and to unveil the bimodality of the distribution (Martinis et al., 2015a; Schlaffer et al., 2017). Therefore, the TSX backscatters in each reservoir were subset 2×2 with two times of iteration, considering the relatively small size of the reservoirs. Segmentation thresholds were obtained for the subsets which fulfill the bimodality, i.e. a valley

and a local minimum exist in the distribution (Schilling et al., 2002). In this study the local minimum was constrained into the interval of -25 dB and -10 dB to avoid the effect of interference of extreme values. Each TSX image was segmented with the mean of the thresholds derived for its subsets to obtain the raw open water mask.

3.3.2.4 Mapping vegetation covered waters

The masks of floating macrophytes obtained from RapidEye data are expected to indicate standing waters, as floating macrophytes can only survive on water surfaces. In a RapidEye image, floating macrophytes appear remarkably brighter than emergent macrophytes and riparian vegetation. By referring to the brightness and greenness, the masks of floating macrophytes were digitized from the RapidEye images. A manual approach was chosen to avoid the potential contamination of terrestrial plants or emergent macrophytes under drought stress. The masks of floating macrophytes were resampled to the same pixel spacing as the TSX data. For a specific data set in the TSX time series, the floating macrophyte mask from RapidEye data acquired on the date closest to the TSX acquisition was chosen and adopted to assist the effective water surface delineation.

GLCM texture indices mean, variance, homogeneity, contrast, dissimilarity, second moment, and entropy (Conners et al., 1984; Haralick et al., 1973) were calculated in all directions in a sliding window of 3×3 pixels on the amplitude of TSX time series. In accordance to other studies e.g., Hagensieker et al, (2017), Nyoungui et al. (2002) and Sarker et al. (2013), GLCM should be derived without any speckle filtering. We chose the GLCM texture to do the analysis, because the GLCM approach produces more texture indices and potentially can reflect integral texture characteristics of the vegetated water surfaces. The TSX data were acquired and delivered in a depth of 16-bit (Fritz and Eineder, 2013). In order to be comparative to SAR data delivered with different bit depths, TSX data were scaled to 8-bit before the GLCM indices calculation.

Principal Component Analysis (PCA) was applied on the stack of all calculated GLCM indices to reduce the number of variables and obtain the most relevant features. The PCA results showed that

the GLCM variance is the primary feature constituting the first PC. For all the data used in the study the absolute loadings of GLCM variance were larger than 0.97 (Figure 3.6 A). The first PC has explained most of the variance, over 90% for all the reservoirs on all the datasets (Figure 3.6 B). Therefore, the GLCM variance was used as the sole input for further delineation of macrophyte-covered water surfaces. This indicates that regarding GLCM, variance is the most adequate parameter to explain most of the local complexity and heterogeneity of SAR scattering in the reservoirs in comparison to other GLCM texture indices. Since the time series of TSX data on EEC level has undergone multi-looking, the remaining heterogeneity contribution of SAR speckle is regarded to be very small and thus ignored.

We assumed that the GLCM variance sub-populations dominated by individual types of scattering in Figure 3.4 (A) follow normal distributions (Figure 3.4 B). After the open waters were masked off, each TSX image over a reservoir was subset by 4×4 to derive the modes and standard deviations of the GLCM variance distributions of the subsets. The modes of all the TSX data subsets cluster at the values of 0.5, 3.5, 6.5, 8.0 and 12.0, while the range of the standard deviation spans relatively large (Figure 3.6). We attributed this phenomenon to the impurity of the scattering in the squared subsets. More specifically, more than one type of scattering take place in the subset and contributes to the standard deviation but only one type of scattering dominates and presents the mode for the subset distribution. Kmeans clustering was applied with centers at 0.5, 3.5, 6.5, 8.0 and 12.0 to generalize the modes. Meanwhile, the minima of the standard deviations corresponding to the same modes were regarded as the standard deviation of the sub-populations. At last, five sub-populations were derived, with their mean values at 0.8, 3.3, 6.7, 8.6 and 11.8 and standard deviations at 0.62, 1.73, 2.69, 3.35 and 4.03. The local variance of the SAR backscattering in a GLCM calculation window is positively related to the amount and amplitude of the scattering with high backscattering which is further positively related to the smoothness of the surface. Referring to Figure 3.4 (a) and the observation on the subset modes of the nine reservoirs (Figure 3.6) (i.e. subsets with large means tend to appear in largely vegetated reservoirs), we attributed the five sub-populations to be respectively dominated by scattering A-E illustrated in

Figure 3.4 (a), namely, VS+ SR, VS, DB + VS, MB, DB. The neighboring sub-populations overlap with each other at the tail parts.

In order to validate the confidences of the assumption in Figure 3.4 and the credibility of the above attribution of the sub-populations, we applied linear unmixing using these five sub-populations to derive the proportions of the sub-populations in the reservoirs along the TXS data time series. Linear unmixing is a widely applied approach in the remote sensing domain to obtain the proportions of spectral endmembers e.g. vegetation and soil in remotely sensed optical images on the pixel level (Asner and Heidebrecht, 2002; Bian et al., 2017; Roberts et al., 1998; Shi and Wang, 2014). It has also been applied on the sediments and on chemicals of runoff to derive the contribution of different sediments and waters sources (Barros Grace et al., 2008; Dietze et al., 2012; James and Roulet, 2006). In this study, the distribution of GLCM variance of individual TSX acquisition within an individual reservoir is analogous to the spectrum of one pixel in the case of unmixing optical remote sensing data (Adams et al., 1995; Roberts et al., 1998). Thus, the linear unmixing was implemented on the reservoir level instead of on the pixel level which is the case in the linear unmixing of optical images. In this study it is assumed that the GLCM variance distribution in a reservoir consists of the linear sum of the distributions of sub-populations (i.e., the endmembers when unmixing optical remote sensing data) with corresponding proportions (Figure 3.4). Linear unmixing was conducted on the time series of the GLCM variance distributions to derive the proportions of the sub-populations in the reservoirs on each TXS acquisition. The proportions of the sub-populations in a reservoir were obtained by nonnegative least squares algorithm (Lawson and Hanson., 1974).

The unmixing approach was implemented as below:

$$A = \sum_{i=1}^{n} P_i A_i + \epsilon \qquad (3.2)$$

with the constraint:

$$\sum_{i=1}^{n} P_i = 1 \quad (3.3)$$

In this study, A is the density of a value, say M, in GLCM variance distribution H; P_i is the proportion of sub-population H_i; A_i is the density of M in the ith sub-population H_i; ϵ is the residue failed to be expressed by either of the sub-population H_i.

$$M \sim N(\mu_i, {\sigma_i}^2) \ when \ M \in H_i \quad (3.4)$$

μ_i and σ_i are the mean and the standard deviation of the sub-population H_i, respectively; μ_i results from the Kmeans clustering, and σ_i is the minimum of standard deviations corresponding to μ_i. The distribution H_i is simulated with 5000 samples from the given μ_i and σ_i.

The sub-populations dominated by multiple scattering and the double scattering with high local GLCM variance are expected to be more in the largely vegetated reservoirs than in the marginally vegetated ones. The sub-populations dominated by volumetric scattering on the bank with small GLCM variance prevail in the marginally vegetated reservoirs. By comparing the differences between the two types of reservoirs, we can distinguish the scattering coming from the vegetated waters from that originating from the bank by the following threshold:

$$T = (Max_b + Min_I)/2 \quad (3.5)$$

Max_b is the mean of the sub-population which possess the largest mode among those taking place on the bank, and Min_I is the mean of the sub-population that has the smallest mode among those prevailing in the vegetated water surfaces. In this study, we attributed the sub-population with means at 0.8, 3.3, 6.7, to take place on the bank, and the sub-populations with means at 8.6 and 11.8 on water. Thus, $\mathrm{Max_b}$ is 6.7, $\mathrm{Min_I}$ is 8.6, and the threshold 7.6 was used to distinguish the water surfaces producing DB and MB from the other scatterings in the reservoirs. In reality, the optimal threshold might vary slightly from the T due to the varying sizes of sub-populations. But it should be very close to the value of 7.6 in the case of the studied reservoirs based on the calculated GLCM texture.

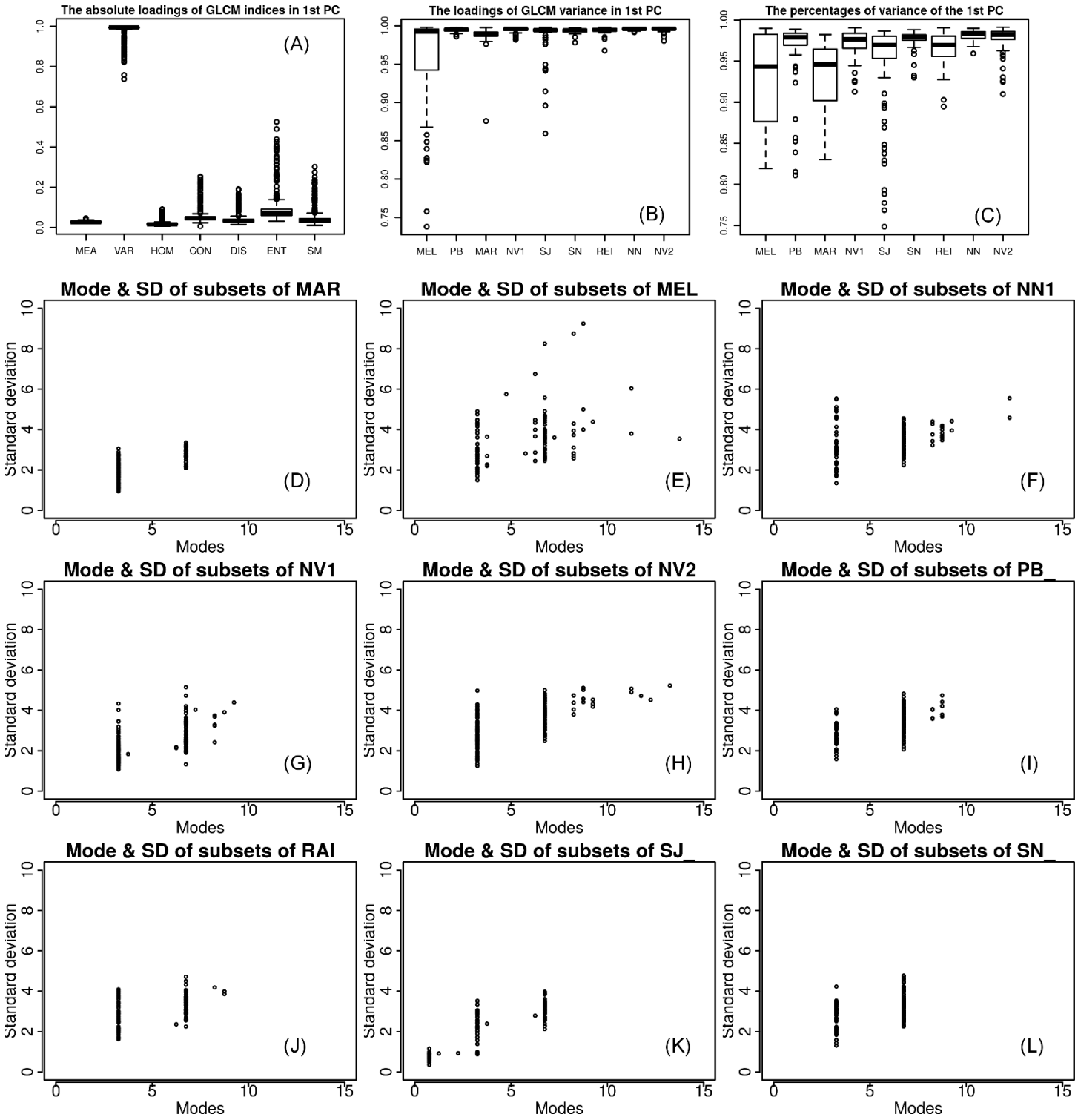

Figure 3.6 Results of the PCA on the GLCM texture for all acquisitions over the reservoirs in the study. MEA, VAR, HOM, CON, DIS, ENT and SM refer to the seven GLCM texture indices: mean, variance, homogeneity, contrast, dissimilarity, entropy and second moment. MAR MEL, NN1, NV1, NV2, PB, RAI, SJ and SN are the abbreviations of the reservoirs Marengo, MEL, NN1, Nova Vida 1, Nova Vida 2, Paus Branco, Raiz, São Joaquim and São Nicolau.

3.3.2.5 Derivation of effective water surface

The masks of open waters, floating macrophytes and water surfaces vegetated by emergent macrophytes were stacked into one layer. The morphological closing with a square window of size 5×5 pixels, and the gap filling were subsequently applied on the derived water masks.

3.4 Results

In this section, we present the dominant scattering types as output of linear unmixing along the times series, the effective water surfaces obtained for marginally and largely vegetated reservoirs, the spatial and temporal changes in the open and effective water surfaces in Nova Vida 1 as an example of results in this aspect, the temporal changes in the areas of open and effective water surfaces in the nine reservoirs. The accuracies of the effective water surfaces based on available in-situ data are presented in the end of the section.

3.4.1 Proportions of the sub-populations dominated by different types of scattering

Along the time series, the five sub-populations showed the seasonal trajectories of different scattering in all the nine reservoirs (Figure 3.7). The assumed sub-populations dominated by DB and MB are mainly present in the largely vegetated reservoirs i.e. São Nicolau, NN1, Paus Branco, Nova Vida1 and Nova Vida 2, and in the small and marginally vegetated reservoirs Raiz and Mel. In the marginally vegetated reservoirs, they tend to account for large proportions with abrupt fluctuations in the raining season and none in the dry season (Figure 3.7). The sub-population dominated by DB + VS had analogous proportions in both types of reservoirs, and showed significant seasonal trends, i.e. more in the wet season than in the dry season. In contrast, the sub-populations dominated by VS + SR are mainly present in the reservoirs Marengo, São Joaquim and São Nicolau. In the marginally vegetated reservoir São Joaquim, this sub-population plays a dominant role in the dry season. This sub-population showed nearly stable proportions in the largely vegetated reservoirs São Nicolau and marginally vegetated reservoir Marengo throughout the time series.

In summary, the sub-populations dominated by DB and MB tend to prevail in the vegetation covered reservoirs, while the sub-populations dominated by DB + VS prevail on the bank in the wet season. Marginally vegetated reservoirs of large size are characterized by scattering of low GLCM variance. Largely vegetated reservoirs show more scattering of large GLCM variance. The marginally vegetated reservoirs show common seasonal characteristics, so do the largely vegetated reservoirs. This means the previous attribution of the sub-populations in section 3.2.1 is reasonable.

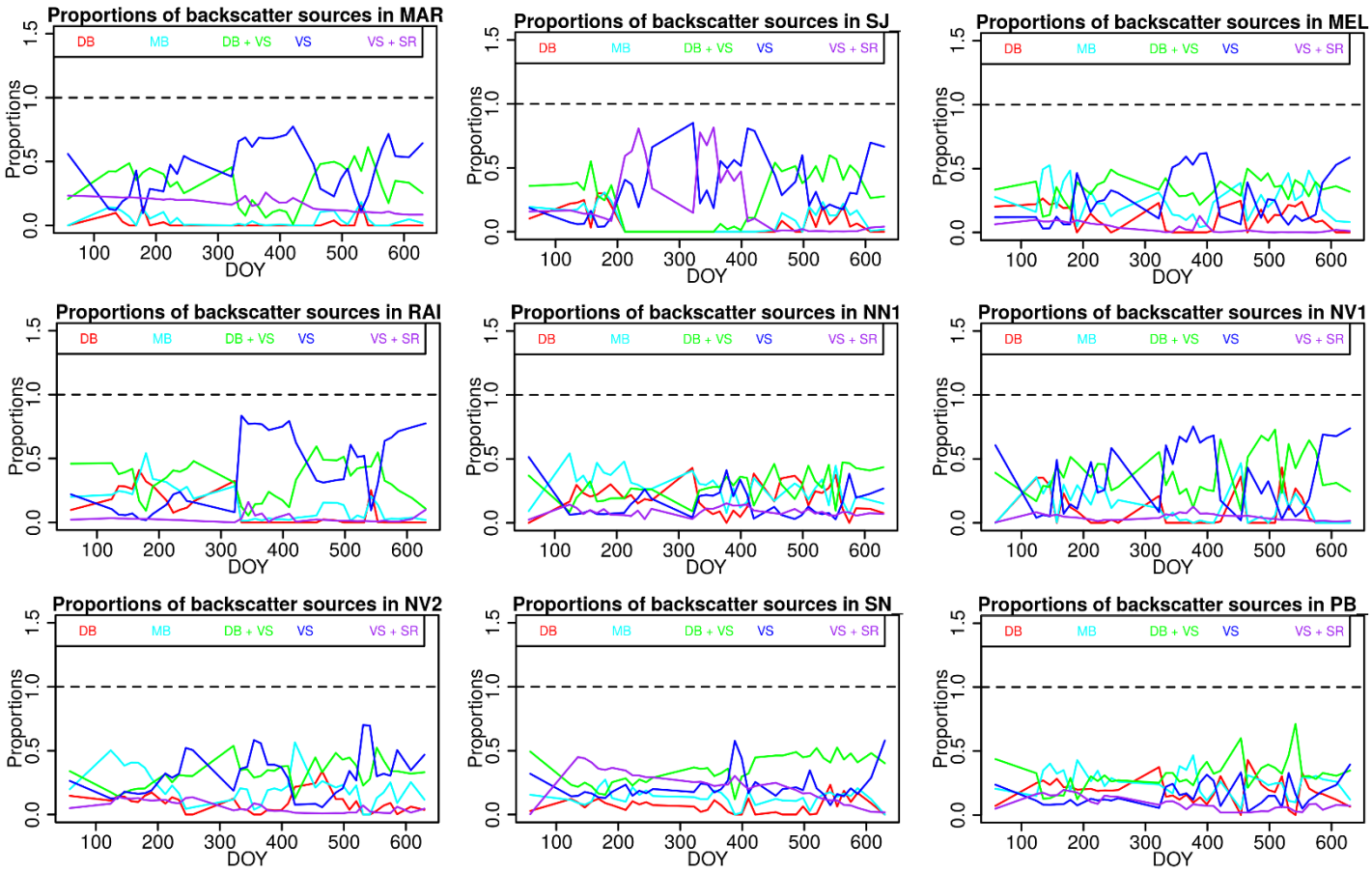

Figure 3.7 Proportions of the GLCM variance sub-populations dominated by different types of scatterings in each reservoir along the TSX time series.

Figure 3.8 presents the RMSE of the modelled results for all the reservoirs and all acquisitions, and the correlations of the simulated and the observed proportions of all GLCM variance values. RMSE are lower than 0.1 and correlation coefficients are larger than 0.7 with a mean at 0.9, which indicates the confidence of the modelling. Therefore, the threshold of 7.6 used to distinguish the scattering on the bank and the scattering on the vegetated water surfaces is regarded to be reasonable.

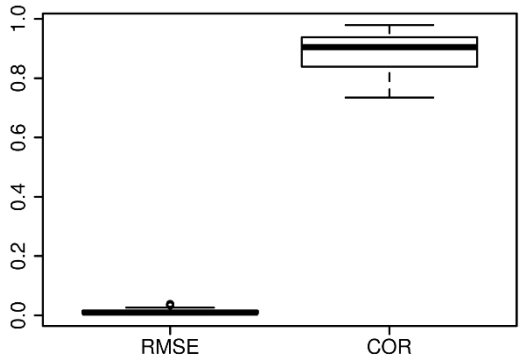

Figure 3.8 The RMSE of the modelled results for each reservoir and correlation coefficients of the modelled values and the value from TSX time series images. The unit for both RMSE and COR is 1.

3.4.2 Effective water surfaces

3.4.2.1 Reservoirs with little macrophyte coverage

There are only few macrophytes growing along the waterlines in Marengo (Figure 3.9). The open water surface coincides well with the in-situ data (Figure 3.9 A-B). Very narrow waterways at the tail part of Marengo indicate the mudflat that was inaccessible during the field surveys or too narrow to show in the SAR data. The parallax, the inherent nature of SAR data, barely caused any visible mismatching between the remote sensing results and in-situ data in this reservoir. However, these two factors suggest that the accuracy of open water from SAR data, though high, can never reach 100%. This phenomenon was also noticed in São Joaquim, Mel, and Raiz.

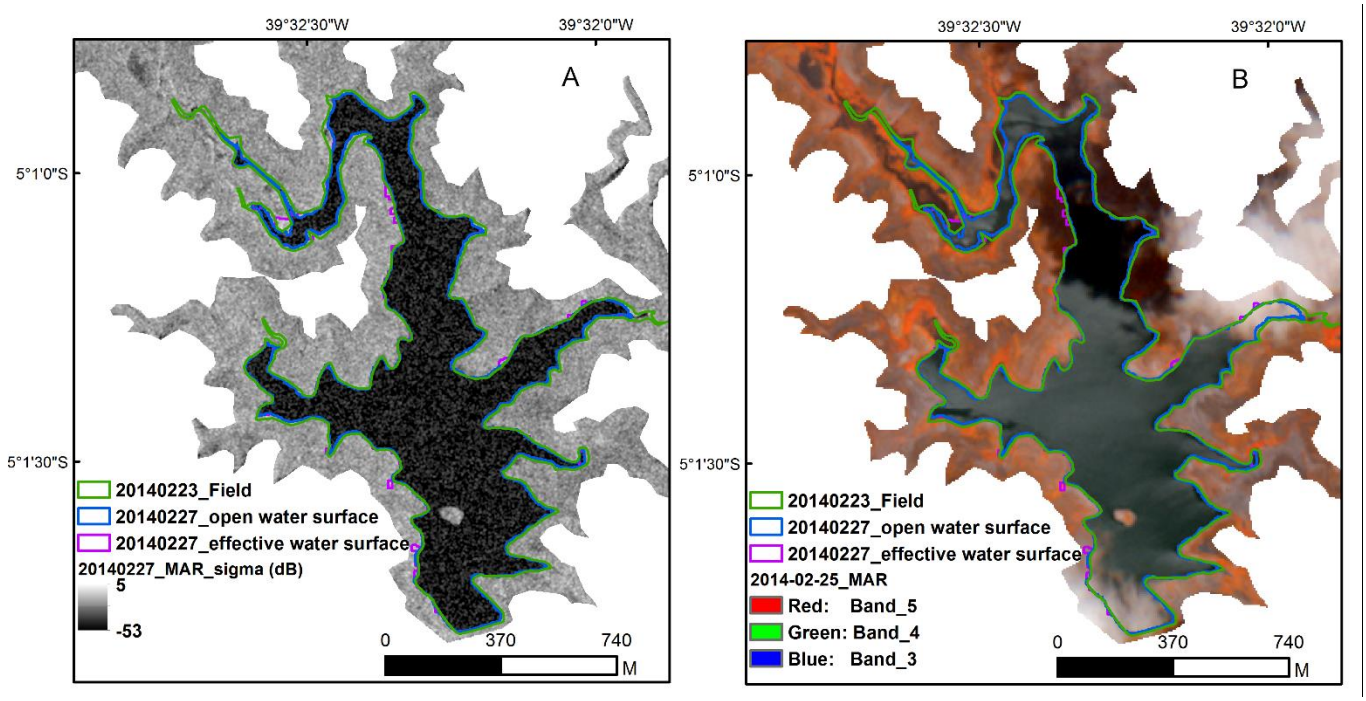

Figure 3.9 Waters mapped from TSX data for the reservoir Marengo. Blue polygons denote the open water surfaces, violet polygons indicate the effective water surfaces, and green polygons the in-situ water surface. (A) The backgrounds are the backscattering coefficient of TSX data; (B) the same data overlaid on the RapidEye data acquired on 2014-02-23

3.4.2.2 Reservoirs with large macropyte coverage

Paus Branco is one of the reservoirs vastly covered by macrophytes of various species. The results in Figure 3.10 A-B were derived from TSX acquired on 2015-07-07 in the end of the wet season. The results from this TSX data indicate the close-to-the-effective water surface. Floating macrophytes, i.e. the bright green area in RapidEye data (Figure 3.10 B), show similar backscatters to the terrestrial part (Figure 3.10 A). A few similar cases were also noticed on data acquired for Nova Vida 2 and NN1. Waters under emergent macrophytes which are at the senescence stage and do not show greenness are also mapped for Paus Branco from SAR data (Figure 3.10 A-B).

The reservoir Nova Vida 1 is also widely vegetated by macrophytes, and in-situ data are thus difficult to attain. The only available in-situ data were acquired on 2014-06-15 and cover parts of the reservoir, thus only used to indicate the effective water surface at that time in the reservoir. All the areas of high backscatters and variance and adjacent to the open water surface were correctly

delineated as water areas (Figure 3.10 C). On the RapidEye acquired in the wet season the terrestrial vegetation shows similar spectral characteristics to the macrophytes in waters (Figure 3.10 B). But TSX data were able to distinguish aquatic vegetation from the terrestrial and yield accurate water surfaces (Figure 3.10 B).

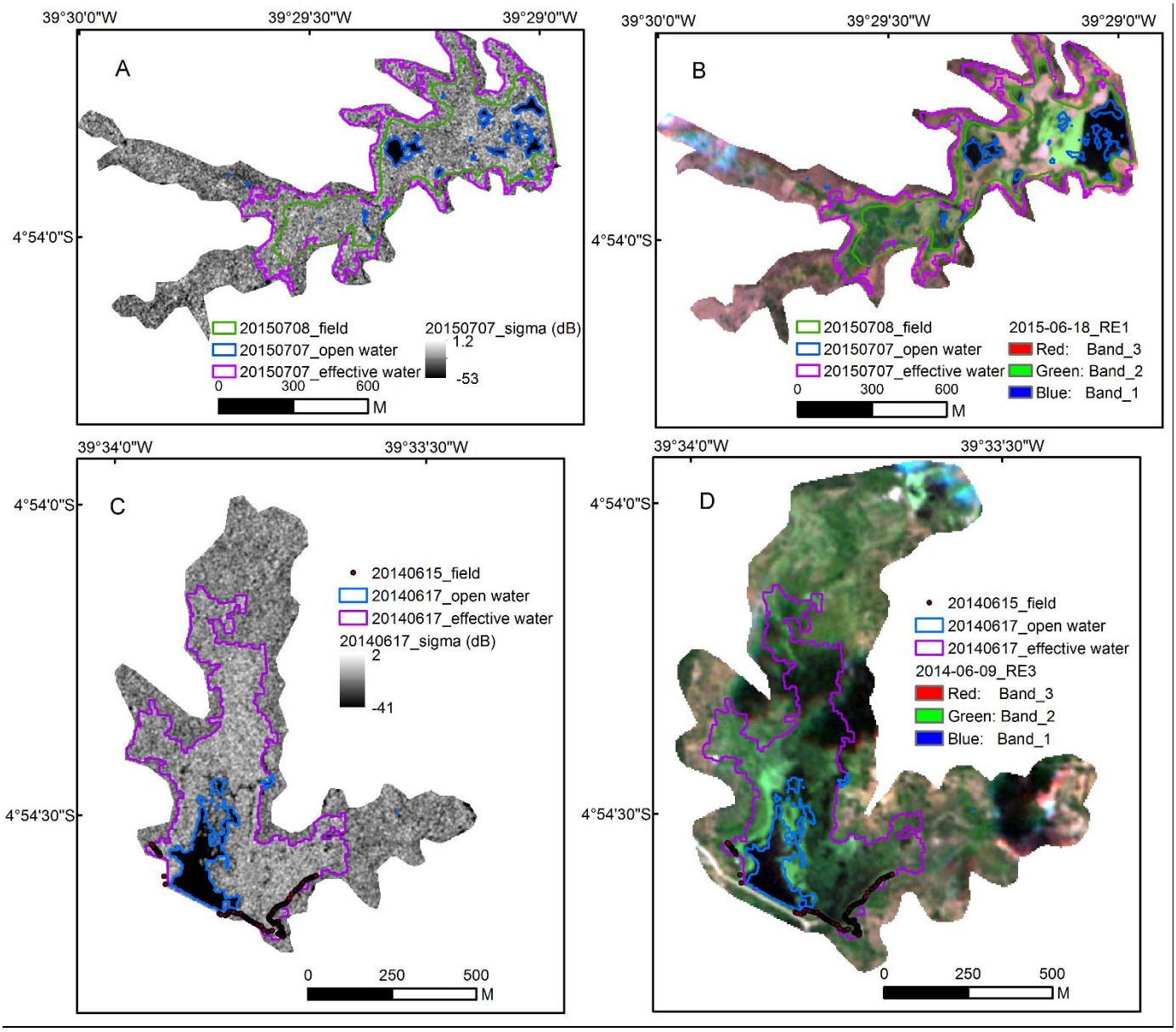

Figure 3.10 The final water surfaces delineated for the reservoir Paus Branco and Nova Vida 1. A: the water surfaces extracted from TSX data acquired on 2015-07-07 (violet), and in-situ data on 2015-07-18 (green polygons). Background is the backscatters of TSX image acquired on 2015-07-07; B: same data overlaid on the RapidEye data acquired on 2015-06-18. C: Water surfaces for the reservoir Nova Vida 1 from TSX data acquired on 2014-06-17 (violet) and from field (dots) on 2014-06-15. The background is the backscatter of TSX 2014-06-15. D, and the same

results overlaid on the RapidEye image acquired on 2014-06-09.

3.4.3 Spatial-temporal changes in effective water surfaces

Figure 3.11 shows, as an example, the temporal changes in the open water and the effective water surfaces delineated for the reservoir Nova Vida 1. Only few bare grounds which present similar backscatters to calm open waters remained (Figure 3.11 A). Both the open and effective water surfaces in the reservoir have retreated towards the outlet. The general changes in the open and effective water surfaces are reasonable from the spatial perspective. Open water surfaces only represent part of the total ones in the reservoirs (Figure 3.11 A and B). Few exceptional overestimates of effective water surfaces were obtained for the dates in the wet seasons (Figure 3.11 B).

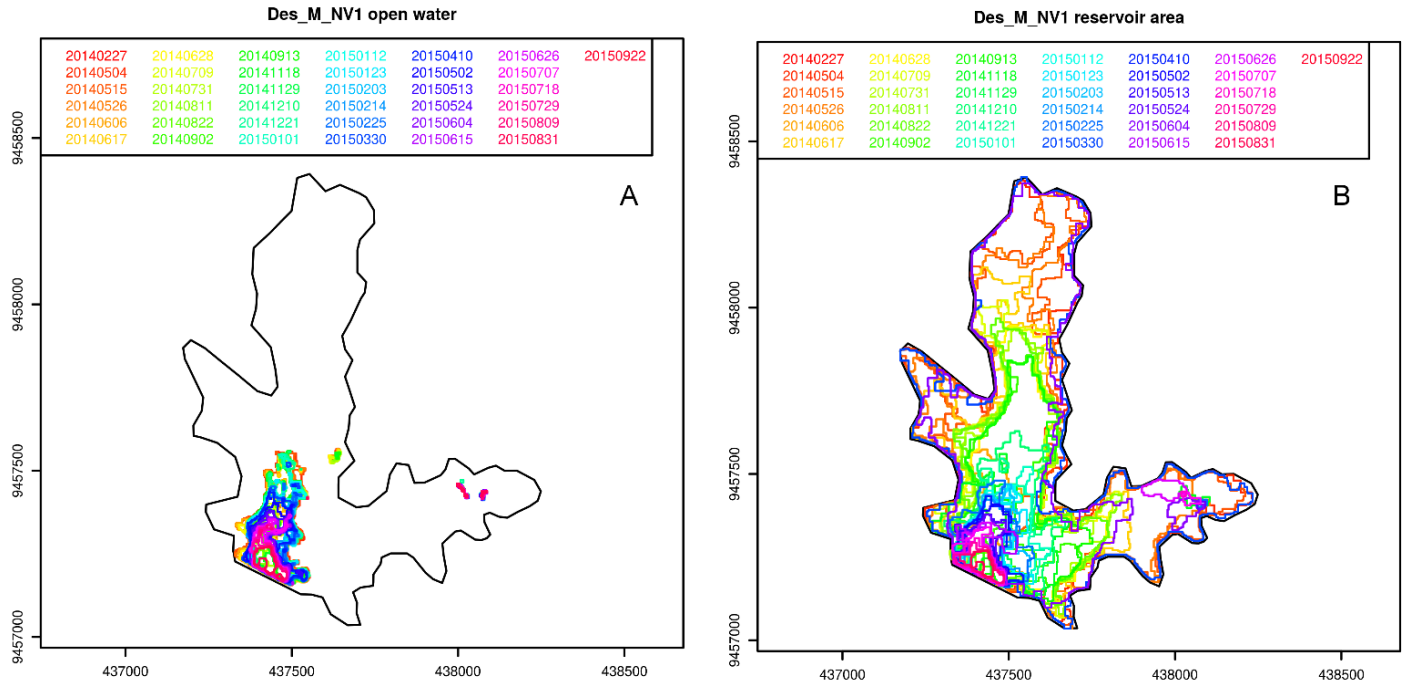

Figure 3.11 Temporal-spatial changes in open water surfaces (A) and effective waters surfaces (B) in the reservoir Nova Vida 1.

Figure 3.12 shows the profiles of the open and effective water surfaces in all the nine studied reservoirs along the time series. In the largest reservoir Marengo where the vegetation coverage over water surface is minimal the open water surface can denote the effective water surface. The

only significant overestimate in Marengo coincides with the effective water estimate anomalies in other reservoirs. Water surfaces in São Joaquim whose water free bottom frequently was used as crop field, and two small reservoir Raiz and Mel are marginally vegetated, but often overestimated in our study, particularly in the wet season of 2014 (Figure 3.12). The area differences between open and effective water surface are significant in the largely vegetated reservoirs São Nicolau, Nova Vida 1, Nova Vida 2, Paus Branco and NN1 (Figure 3.12). The open and effective water surfaces show similar change trends along the time series (. Most of the overestimates were obtained for TSX data acquired in the wet season, e.g. January to June. Despite of overestimates, the seasonal changes are remarkable both in open and the effective water surfaces.

The following trends can be obtained for the nine studied reservoirs: all the water surfaces in the reservoirs decreased during the studied period; São Joaquim, Raiz and Mel became empty in October 2014, occasionally collected little water and eventually fell empty in 2015; Nova Vida 2 turned dry in July 2015; São Nicolau and Nova Vida 1 became dry in December 2015. The vegetated water surfaces in Nova Vida 1 were largely in 2014 but became little in 2015 till the reservoirs dried up; Marengo, Paus Branco and NN1 are the only three reservoirs that still had water by the end of the studied period.

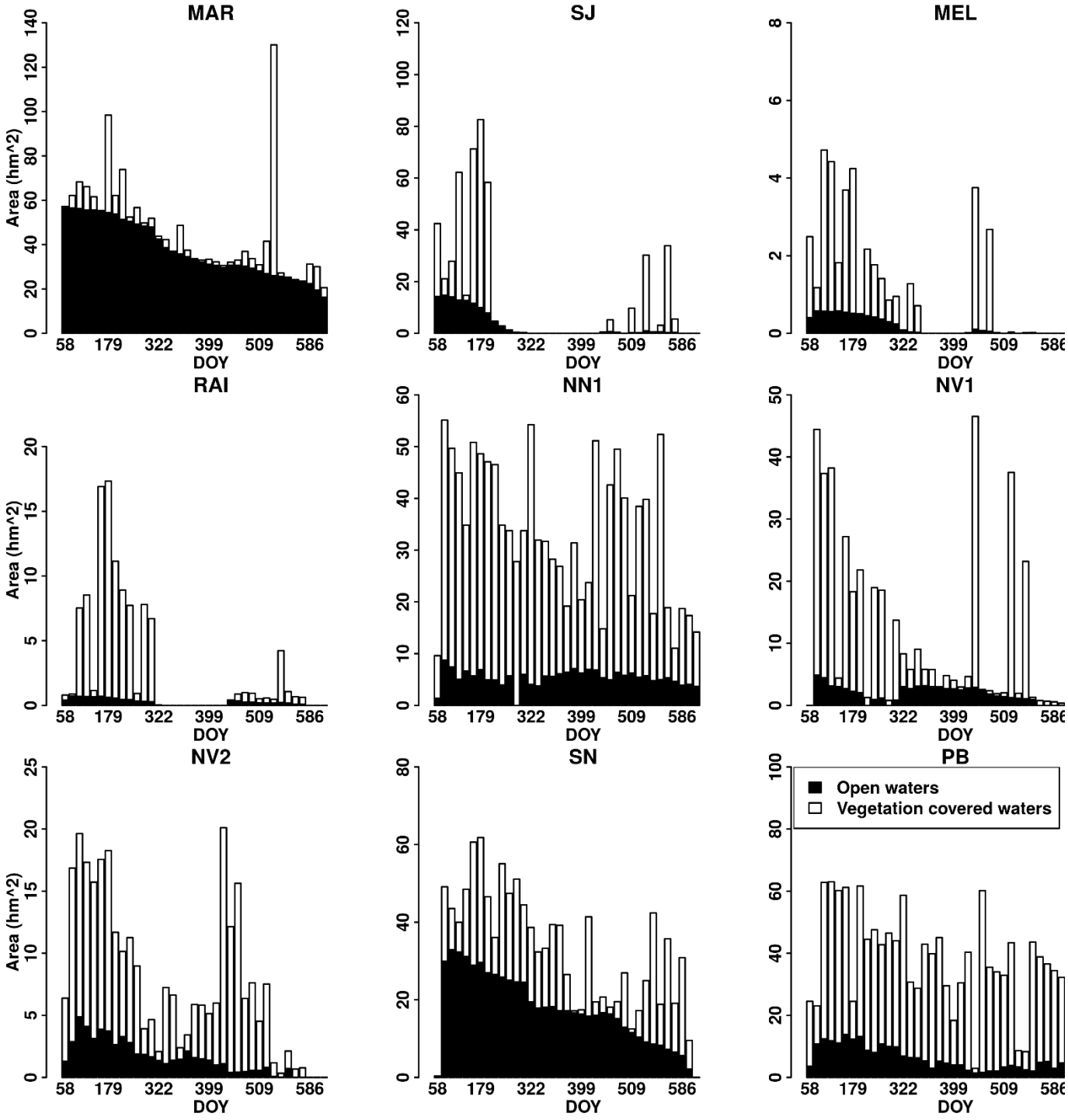

Figure 3.12 The change trends of the open waters and the effective waters in all studied reservoirs. Abbreviations MAR, SJ, MEL, RAI, NN1, NV1, NV2, SN and PB refers to the reservoir Marengo, São Joaquim, Mel, Raiz, NN1, Nova Vida 1, Nova Vida 2, São Nicolau and Paus Branco, respectively. DOY indicates the day starting from 2014-01-01.

3.4.4 Accuracy assessment

In Table 3.2 the accuracies of the water surfaces delineated for three selected reservoirs are listed. Marengo represents reservoirs with little vegetation coverage, whereas Paus Branco and São Nicolau represent the reservoirs with heavy vegetation coverage.

In the reservoirs with little vegetation coverage, the in-situ data include some small areas of wet soil adjacent to the open waters, particularly at the tail of the reservoir. These wet soil spots are the main cause of low accuracies. The high producer's accuracies demonstrate that open waters represent the overall waters of reservoir Marengo and reservoirs alike.

Table 3.2 Accuracies of the delineated water surfaces for representative reservoirs (%).

Date of in-situ data collection	User's accuracy			Producer's accuracy			Overall accuracy		
	Marengo	São Nicolau	Paus Branco	Marengo	São Nicolau	Paus Branco	Marengo	São Nicolau	Paus Branco
2014-02-27	90.24	*	-	99.56	*	-	99.93	*	-
2014-05-26	-	81.38	-	-	94.73	-	-	94.80	-
2014-11-29	84.99	83.77	-	99.46	87.55	-	99.94	91.54	-
2015-01-12	83.29	-	-	99.30	-	-	99.93	-	-
2015-03-30	87.53	83.11	-	96.69	89.68	-	99.68	95.97	-
2015-07-07	84.39	82.43	97.56	98.94	76.29	57.65	99.92	92.93	77.11

* indicates that the reservoir was empty at the overpass of the TSX satellites; - indicates that there was no match of in-situ data and TSX data.

More in-situ data were available for São Nicolau in comparison with Paus Branco, and the overall accuracy for this reservoir is > 90%. Fewer in-situ data were available for Paus Branco and some of them fall into the gaps in the TSX time series. For Paus Branco on 2015-07-07, the overall accuracy is > 77.11%. At the end of the wet season, the wet soil adjacent to the water was falsely included and led to a low producer's accuracy (Figure 3.10 A-B).

3.5 Discussion

This study investigated the potential of GLCM textural information for mapping macropyte-covered water surfaces. Open water surfaces were derived by segmenting the SAR

backscattering coefficient with minimum error algorithm. Linear unmixing approach was implemented to obtain the proportions of the sub-populations dominated by different types of SAR scattering in a reservoir. The SAR texture index, i.e. GLCM variance, was subsequently segmented to discriminate the scattering on vegetated water surfaces from the double or multiple bouncing on emergent macrophytes covered waters. The effective water surfaces were delineated for nine reservoirs in the TSX data time series which mapped the reservoirs of diverse macrophytes status and water areas. The accuracies of the final water areas in the reservoirs were assessed. Despite the confidence in the results derived for reservoirs under various conditions (e.g. vegetation coverage and type, seasons of the acquisition), the performance of the approach is still affected by precipitation, topography, and the macrophyte canopy closure.

3.5.1 Impact of precipitation

The presence and changes of wet soil in the reservoirs affected the proportions of the sub-populations dominated by different types of scattering and the delineated effective water surfaces. The dielectric constants of wet soil rises as soil moisture increases (Shoshany et al., 2000; Troch, 1996; Ulaby and Long, 2014). However, it reaches the maximum when soil moisture is approx. 50% - 60% (Shoshany et al., 2000; Troch, 1996; Ulaby and Long, 2014), probably because soil with moisture > 60% may be dominated by the scattering characteristics of water rather than that of soil. It is the case on SAR imagery acquired during or shortly after heavy rainfall events when the surfaces of the ground and vegetation remain oversaturated. This converts the high GLCM variance on the vegetated waters in dry condition to the low GLCM variance, interestingly like sparsely vegetated banks but not bare banks (Figure 3.7), and thus introduces an underestimation in the effective water surfaces in the largely vegetated reservoirs like Paus Branco and Nova Vida 1 (Figure 3.10). As time passes, the characteristics of the wet objects emerge. The intensity of backscattering from wet soil can be equivalent to the double/multiple bounces from the macrophyte covered water surfaces (Shoshany et al., 2000; Troch, 1996), the thresholds obtained for GLCM variance cannot discriminate these two sources of scattering. Therefore, both are attributed as double/multiple bounces from the macrophyte-covered water surfaces, resulting

in an overestimation of sub-population dominated by double bounce and multiple bounces, as well as the effective water surfaces. The effect of wet soil surfaces appears as abrupt fluctuations in the water surface time series (Figure 3.7 and Figure 3.12). The effect of oversaturated soil was noticed in largely vegetated reservoirs after heavy rainfall events (Figure 3.7 and Figure 3.12). The effect of enhanced GLCM variance of wet soil presents more in the wet season when the soil surface is covered by little vegetation (Figure 3.7 and Figure 3.12), e.g. in the beginning of the wet season.

Solely with SAR data it is difficult to distinguish the effect of precipitation in the wet season. Since optical data usually suffer from the clouds cover during precipitation and from the confusion of terrestrial plant in sunny days, optical data hardly possess any potential in solving this problem. However, combining SAR data acquired before the precipitation data from other SAR senor with similar configuration can be a solution to this issue. SAR data with different polarization also hold potential in tackling this problem.

3.5.2 Impact of topography

Due to the foreshortening effect, slopes facing the satellite show SAR backscattering intensity as high as those from the double or multiple bounces (Ford et al., 1983). These fore slopes account for large area proportions in the two smallest reservoirs Mel and Raiz, and mistakenly contribute more to the sub-populations dominated by double/multiple bounces and to the water areas delineated than that in the large reservoirs. Except those from the wet reservoir bottom in the wet season, nearly all the mistaken areas of the water in these two reservoirs result from the effect of topography, as there are barely any macrophytes growing in these two reservoirs. The effect of topography is difficult to tackle in the case of small reservoirs but can be ignored in the case of large reservoirs.

3.5.3 The effect of macrophyte canopy closure

Closed canopies pose a strong obstruction in mapping water surface below the canopy using SAR data (Hess et al., 1990; Silva et al., 2008). Field observation revealed two sources of closed canopies in the reservoirs: the floating macrophytes and the seasonally varying emergent

macrophytes. These two sources of closed canopy have increased the proportions of volumetric scattering which mostly take place on vegetated banks.

Floating macrophytes, which are frequently present with high canopy density in some reservoirs, separate open waters from waters vegetated by emergent macrophytes (Figure 3.10 B). Dense floating macrophytes usually show similar backscatter and texture to the terrestrial part of the reservoirs (Figure 3.10 A), because barely any SAR pulses can penetrate and return through their nearly closed canopy. This phenomenon tends to be present in the deep dry season when the nutrients in the water accumulate, macrophytes prosper and their canopy density increases. Therefore, floating macrophytes were manually delineated from optical RapidEye data to indicate their locations and extents in the corresponding SAR data. By doing so, the deterioration of floating macrophytes on the effective water surfaces in this study was mitigated. However, in further studies in different areas optical remote sensing data suitable for floating macrophytes derivation in terms of spatial and temporal resolution can also be adopted, possibly in combination with SAR data to further explore the synergies in effective water surface mapping. For example, it is also worthwhile to investigate SAR data of acquired with different polarization, wavelength or spatial resolution. Drifting as local winds blow, the floating macrophytes are probably the reason for slight fluctuation in the open water surfaces detected in the reservoirs Paus Branco, Nova Vida 2 and NN1 (Figure 3.12) where reasonable coverage of floating macrophytes such as water lettuces were noticed.

Studies have shown that SAR scattering decreases with increasing leaf area index (LAI) or even become absent with the closed canopy of wetland and mangrove (Durden et al., 1995; Krohn et al., 1983). Some gaps in the delineated effective water surfaces coincide with certain places in Paus Branco and Nova Vida 2 where emergent macrophytes grow, typically sedges such as *Oxycarium cubense*, as confirmed by observations in the field. This may be explained as when the canopies of the emergent macrophytes developed denser, the scattering transferred from double or multiple bounces into volumetric scattering and failed to show large variance. The closed canopies thus can

deteriorate the user's accuracy of the effective water surfaces derived for reservoirs with large coverage of emergent macrophytes. The incidence angle of the TSX data in this study is 30 degree, within the suitable range of incidence angles of 15 - 40 degrees, for mapping water surfaces beneath vegetation (Hess et al., 1990; Marti-Cardona et al., 2010). Cohen et al.(2016) found that it is not possible to detect the water/flooded area beneath boreal forest with X- band data if the canopy closeness is over 80%, even if it is acquired in competent incidence angles. Therefore, the canopy closure of the emergent macrophytes beneath which the water failed to be mapped is probably also > 80%. Vice versa, those water surfaces detectable with GLCM variance in the nine studied reservoirs is likely covered by canopy closure less than 80%.

Very sparse grass-like macrophytes cannot alter scattering sufficiently to introduce large GLCM variance but can only elevate the scattering slightly. This might result from the fact that the sub-population VS + SR are present in the reservoirs São Nicolau throughout 2014.

3.5.4 Effective water surface map

Compared to the open water mapping with SAR data and optical data (Li et al., 2015b, 2014; Martinis et al., 2015b; Pekel et al., 2016), this study derived not only the open water surfaces, but also those covered by vegetation. The temporal changes of the effective water surfaces were obtained with high accuracies with few exceptions caused by precipitation events. The parameters in the presented study were defined by referring to the intrinsic texture characteristics of the studied reservoirs. The same criterion was applied to all nine reservoirs with 37 TSX data sets.

In terms of the range of the study period, this study covers a two-year period, and revealed the seasonal variations of sub-populations dominated by different types of scattering and changes in the open and effective water surfaces for this period. This implies that in terms of study period the approach of the study is superior to the inundation mappings with spectral vegetation indices e.g. NDVI and NDWI or classification with in-situ data on a few timestamps (Bourgeau-Chavez et al., 2001; Feng et al., 2012; Voormansik et al., 2014; Ward et al., 2014; L. Zhao et al., 2014).

Moreover, the proposed approach only employed remotely sensed data, while no in-situ data were used to generate the final maps. In-situ data were only used to validate of the results of effective water surfaces. Therefore, the approach can be applied to similar areas for an operational monitoring over a long period.

However, from the data perspective, polarimetric SAR data and indices derived from them probably also hold great potential to provide more insights in the contributions of different scattering sources and to automatically delineate the effective water surfaces in terms of operational mappings. When available in a suitable temporal and spatial resolution, SAR and optical satellite data are seen as synergetic data sources for future effective water surface mapping of inland water bodies. For example, the synergy of data acquired by Sentinel-1 & 2 missions act as candidate of great potentials in this aspect.

3.6 Conclusion

In the presented study, a method was proposed for mapping the effective water surface areas in macrophyte-covered reservoirs with time series of TSX data. The approach was applied to different reservoirs of varying complexity and throughout two consecutive dry and wet seasons. A detailed evaluation, including the use of in-situ data, demonstrated that the approach is robust and holds potential for mapping vegetation covered water surfaces or flooded vegetation. In most cases, the overall accuracies of the effective water surfaces of vegetation covered reservoirs were > 77%. However, precipitation, closed canopy and bare grounds were found to be the main causes for the reduced mapping accuracy. The approach can easily be applied to multi-temporal data, and thus, allows for mapping the spatial-temporal variation of the effective water surface throughout the seasons and years. Finally, the approach is independent of in-situ data. Overall, the proposed approach proofs useful for effective water surface mapping and seems particularly relevant in the context of operational monitoring systems.

4. The spatio-temporal variation of surface water storage in dense reservoirs in NE Brazil, using remote sensing approaches

Abstract: Knowledge on the surface water storage is vital for local/regional water resource management, and for prediction/warning of water related hazard. In NE Brazil, the majority of the reservoirs lack this information. In this study, bathymetry of 2 105 reservoirs in four regions of total area 10 000 km^2 in NE Brazil were derived with very high-resolution digital elevation model (DEM) generated from TanDEM-X data. Based on the reservoirs' bathymetry and a time series of RapidEye satellite images acquired in the period of 2009-2017, the temporal and spatial distribution characteristics of surface water storage in the four regions were obtained. Furthermore, the surface water storages derived from field monitoring were employed to validate the surface water storage yield by remote sensing approaches. Our study found that: 1) DEM derived from TanDEM-X acquired in the deep dry season can reveal the full bathymetry for 90% of the reservoirs; 2) NE Brazil is densely dammed with number of reservoirs 0.04-0.23/km^2, surface water area 0.78-4.13 ha/km^2, and storage 0.01-0.23 hm^3/km^2; 3) Among all the reservoirs, those < 10 ha account for the most of the water body population but contribute the least to the regional surface water storage; 4) From 2009 to 2017 the overall surface water storage decreased at the rate of 10^5 m^3/year on the scale of 5×5 km; 5) The decrease of surface water storage in the period of 2009-2017 showed high spatial heterogeneity. Our study has filled the data gap of the reservoir bathymetry and surface water storage capacity for the 2 105 reservoirs in NE Brazil. The high consistence between the surface water storage yield by remote sensing and that from in-situ measurements demonstrated the potential of monitoring the surface water storage with remote sensing. In addition, the surface water storages derived for these reservoirs on annual frequency for the past eight years can act as a reference for future water management and serve in optimizing hydrological modelling and validation in the regions.

Keywords: Bathymetry, surface water storage, dense reservoir, TanDEM-X, RapidEye, northeastern (NE) Brazil

4.1 Introduction

Surface water support the society in terms of supplying domestic water consumption, irrigation etc. In water scarce area, the knowledge on the water quantity is important for the local/regional water resource management, deployment, and prediction. Surface water also determines the status of wildlife habitats in landscape like wetland. On global scale, there is a necessity to know the spatial and temporal surface water availability (D E Alsdorf et al., 2007).

Remote sensing data and relevant approaches have accounted for a majority part of the studies in deriving surface water quantity and their variations. Based on the physical characteristic of water in the visible spectrum and the interaction of water surface with transmitted synthetic aperture radar (SAR) pulses, water surfaces have been mapped on regional and the global scales (Donchyts et al., 2016; Fluet-Chouinard et al., 2015; Melrose et al., 2012; Papa et al., 2010; Pekel et al., 2016; Song et al., 2014; Vörösmarty and Sahagian, 2000; Westerhoff et al., 2013). Various data sets and approaches have been applied in those studies. The changes of water surface along multiple dates or continuous time series have also been revealed (Song et al., 2014; Tulbure and Broich, 2013). However, the water surface and its variation could not provide sufficient knowledge on the precise water quantity. Efficient water management and decision making require precise knowledge on surface water storage.

Water volumetric variations in large lakes were depicted by combining water surfaces derived from satellite images and water level changes provided by altimetry measurements (Birkett, 2000; Duan and Bastiaanssen, 2013; Jiang et al., 2017; Smith and Pavelsky, 2009; Zhang et al., 2014). However, due to the large footprints of the altimetry measurements and wide inter-measurements distance (Zwally et al., 2002), such-derived water volumetric variations are constrained to large lakes (Birkett, 2000; Duan and Bastiaanssen, 2013; Jiang et al., 2017; Zhang et al., 2014). Therefore, these approaches are not applicable for regions characterized by (dense) small water bodies such as reservoirs. In addition, most of those studies revealed only partial volumetric variation of surface water, instead of the storage capacity variation.

A few studies estimated surface water storage with remote sensing approaches. With water surface derived from remote sensing images, water storage in lakes and reservoirs were derived from empirical or aggregated relations between the water surface and storage (Jiang et al., 2017; Ran and Lu, 2012). However, empirical water storage functions or those aggregated over many water bodies can potentially yield large inaccuracy in the estimated surface water storage. In addition, Yuan et al. (2017) estimated the surface water storage in Congo basin from the water level-storage function fitted from the water levels obtained for the region with InSAR technique.

In areas without available water storage functions, the surface water storage can be derived from bathymetry which is the morphology of the water bodies. Up to now, various mechanisms have been investigated to derive bathymetry from remote sensing data and further to extract the surface water storage. Current studies on bathymetry retrieval mainly investigated shallow coastal areas, based on the attenuated substrate reflectance on optical image or the Bragg scattering of waves which are modulated by submarine topography and captured by SAR images (Brusch et al., 2011; De Loor and Loor, 1981; Dierssen et al., 2003; Jay and Guillaume, 2014; Pacheco et al., 2015; Shuchman et al., 1985). The approaches adopted in these studies require certain conditions in the regards of clarity, depth , vastness of open water surface, and wind speed (> 3 m/s) (Dierssen et al., 2003; Jay and Guillaume, 2014; Reichert et al., 1998), which inland water bodies do not frequently fulfill. However, Sneed and Hamilton (2007) and Williamson et al. (2017) have adapted the physicl model developed by Philpot (1989) for coastal batymetry derivation, and obtained the water volumes of glacier lakes in Greenland using ASTER and MODIS data, respectively. Even though, their studies still depend on the absence of sediment in those lakes formed on pure ice (Sneed and Hamilton, 2007). Moreover, Feng et al., (2011) attributed elevation measured along transactions to the isoclines yielded by MODIS data, and derived bathymetry for Poyang lake. Furthermore, the DEM derived from remote sensing images mapping the water bodies at low water stage can represent the bathymetry for them. Assuming the reservoirs were empty during the flights of SRTM DEM

mission in 2002, Avisse et al. (2017) adopted SRTM DEM to represent the bathymetry of a few inaccessible reservoirs in Syria, and derived the water storage variation in those water bodies along time series. Furthermore, Messager et al., (2016) developed a number of statistic models to model the global water storage, by referring to the surrounding topography of the water bodies represent by SRTM DEM. However, their models were constrained to natural lakes, and showed poor performance on water bodies smaller than 10 km^2 (Messager et al., 2016).

Interferometry SAR (InSAR) is a very effective technique for the DEM generation and ground displacement mapping (Bamler and Hartl, 1998; Rosen et al., 2000; Small, 1998). The TanDEM-X satellites are new generation of SAR constellations designed to generate a global DEM of high resolution and accuracy (Krieger et al., 2007; A. Moreira et al., 2004). DEMs derived from single pass TanDEM-X data have been used to study volcanic morphological changes, forest biomass estimate, and reservoir bathymetry retrieval etc.(Karila et al., 2015; Kubanek et al., 2015; Rossi et al., 2016; Schlund et al., 2013; Zhang et al., 2016). Among all these studies, Zhang et al. (2016) found that the accuracy of the DEMs derived from single pass TanDEM-X data can reach one meter at the areas of gentle terrain, and demonstrate great potential for representing reservoirs bathymetry. If derived from the very water level stage and covering a large area, those DEMs can provide bathymetry for regional water bodies. Integrating those DEMs with images of very high resolution (VHR) which provide the historical water surfaces can potentially reveal the historical surface water storage changes on a regional scale.

In the semiarid northeastern Brazil water supply mainly comes from the numerous reservoirs of various sizes. The surface water storages in the reservoirs remarkably concern the residents and authorities due to the frequently occurring droughts. However, most of the reservoirs in the region do not have inventory data to support efficient water management or deployments. There is no record about the spatio-temporal characteristics of the surface water storage in the region. In this study, we aimed to investigate the temporal and spatial surface water storage characteristics in four representative regions of total area of 10 000 km^2, comprising of 2 105

reservoirs of various sizes. We derived the reservoir bathymetry from TanDEM-X data using single-pass interferometry. Subsequently, with the water surface area yielded by RapidEye images acquired in the period of 2009-2017, surface water storages were obtained for the four regions on annual frequency. We further analyzed the spatial-temporal variation in the surface water storage and validated it with data from field observations.

4.2 Data and method

4.2.1 Study area

The climate in NE Brazil is semiarid with pronounced wet and dry seasons. From January to June is the wet season when the major precipitation events take place; the dry season spans from July to December. The average annual precipitation is approx. 600 mm, and the potential evaporation exceeds 2000 mm per annum (INMET, 2018). Caatinga, an endemic seasonal shrubby forest with sparse distribution of trees, is the main land cover in NE Brazil (Bullock et al., 1995).

Since the 19th century, numerous reservoirs have been constructed in NE Brazil to support the local water consumption in the regards of domestic utilization etc. (SIRH/Ce, 2015). Despite the large number of reservoirs and the seemingly enlarged water supply, the region is still vulnerable to frequent droughts. In-situ monitoring of these water bodies has been inconsistent, resulting from the managements undertaken by different country, federal state and local municipality organizations, and only covers a very small fraction of the total water bodies (SIRH/Ce, 2015). Specifically, a few of large reservoirs supported by the federal state and country are regularly monitored and maintained owing to their so-called strategic importance. In contrast, numerous reservoirs of small to medium size and those at remote areas barely receive any attention (SIRH/Ce, 2015). Due to the large number and relatively small size of the reservoirs (SIRH/Ce, 2015), the past abundant studies on the regional and global water mapping failed to provide inventory data for most of the reservoirs, or to depict the historical surface water storage in the region. Up to now, only a few remote sensing studies have aimed at

mapping the reservoirs in these regions , regardless the size of the reservoirs, e.g. (Heine et al., 2014; Zhang et al., 2018, 2016). As a result, the regional surface water storage and the variation characteristics are still unknown for NE Brazil. However, the knowledge is the critical input for effective water management/deployment, and further studies on regional hydrology.

From the vast range of NE Brazil, we selected four representative regions comprising the catchments of Bengue, Madalena, Pentecoste and Sangue (Figure 4.1). The four regions cover areas of 4114, 1575, 5140 and 4539 km^2, and consist of reservoirs of 160, 256, 657 and 1007 supporting the adjacent towns and/or settlements (Figure 4.1).

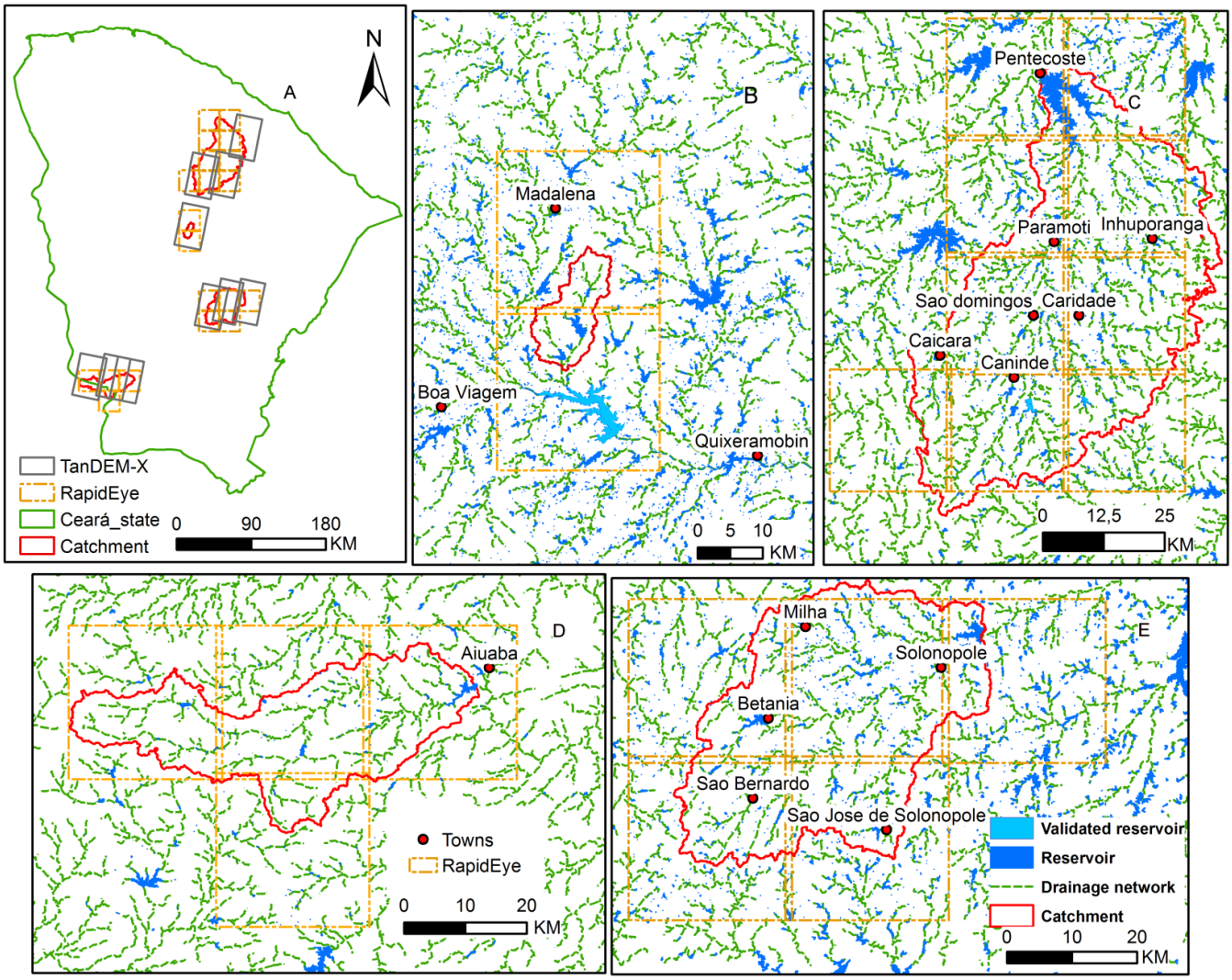

Figure 4.1 Locations of the studied regions. A) The location of the four regions in the federal state of Ceará, Brazil; B-E The distribution of the reservoirs, drainage network and settlements in the four regions

4.2.2 Data

We used TanDEM-X data to derive the DEM and further represent the reservoirs' bathymetry. RapidEye time series provided the annual maximal inundation for the reservoirs. Precipitation data, simulated evaporation and soil moisture were employed to reflect the meteorological changes in the regions. Data acquired by the in-situ measurement were used to validate the surface water storage derived from remote sensing data.

4.2.2.1 TanDEM-X data

The four study areas are covered by ten TanDEM-X geometries in descending orbits (Figure 4.1 A). In October-December 2015 when it was the deep dry season of the year, 59 single pass TanDEM-X scenes were acquired in bistatic mode, mapping each of the four regions two to three times with slightly different height of ambiguity (HoA) (Table 4.1). TanDEM-X data were delivered in the format of Co-registered Single look Slant Complex (COSSC), the same format as used for global DEM generation within the TanDEM-X mission (Duque et al., 2012). The mean coherence of each TanDEM-X scenes is above 0.8, and further parameters of the COSSC TanDEM-X data are list in Table 4.1.

Table 4.1 The details of the TanDEM–X data used in this study.

Catchment	Bengue			Madalena	Sangue			Pentecoste		
Date of acquisition (MM/DD)	10/14 10/25 11/05 11/16	12/30	11/25/ 12/08/ 12/19	10/14 10/25 11/05 11/16	11/27 12/08 12/19	11/09 10/20 10/31 11/11	11/22 12/03 12/14	11/27 12/08 12/19	10/14 10/25 11/05 11/16	12/30
Incidence angle (degree)	40.57	38.42	37.08	33.72	29.9	46.69	45.23	33.74	29.9	31.33
Height of ambiguity	76 75 76 70	63	57 59 60	58 57 58/ 53	42 43 44	99 98 100 86	86 84 85	51 52 53	50 49 50 45	47

4.2.2.2 RapidEye images

The five RapidEye satellites visit the same area on the earth once a day. Such short revisit time

ensures that the entire representative regions were mapped at least once a year, considering the frequent clouds presence in NE Brazil. It is rather difficult for data from other optical missions, such as Landsat images with revisit cycle of 16 days. The time series of RapidEye images covers the period 2009- 2017, and the images were primarily from the dry season. The four regions were covered by 20 tiles of 3A RapidEye tiles (resolution 5 m) (Figure 4.1). In this study, only those images of cloud coverage less than 10% were adopted. In total, approximately 300 scenes of RapidEye images from 20 tiles were used.

4.2.2.3 Maximal water mask

Pekel et al. (2016) derived the historical maximal water surface on global scale from Landsat archive, by employing an expert system comprising of a sequential decision trees. As their study combined images from long time series, the water surface products are regarded to be of high credibility. In this study, the maximal water masks from their study served in the following procedures: 1) constraining the bathymetry extent for individual reservoir mapped; 2) filtering out potential clouds and shadows in the water mask delineated from individual RapidEye image. Prior to the applications, a buffer was applied to the maximal water mask of each reservoirs to leave space for any possible underestimation of the water surfaces, due to the 16 days revisit of Landsat satellites used. The buffer distance is 1/3 of the radius of the circle which covers the equivalent area to the maximal water mask of the reservoirs.

4.2.2.4 Global TanDEM-X DEM

Five tiles of the global TanDEM-X DEM covering the four regions were used to validate the DEMs generate from TanDEM-X data in this study. The TanDEM-X data employed in the global TanDEM-X DEM mission were acquired in two phases characterized with slightly different acquisition baselines. As calm open water surface presents incoherent in an interferogram, the areas occupied by open water on either of the TanDEM-X acquisitions were indicated as invalid (TanDEM-X ground segment, 2013). The resolution of the final DEM data is 12 m (TanDEM-X ground segment, 2013), and the absolute and relative accuracy of the

DEM are 10 m and 2 m, respectively (TanDEM-X ground segment, 2013). The global TanDEM-X DEM is so far the best DEM data set for the region for the validation purpose.

4.2.2.5 Tropical Rainfall Measuring Mission (TRMM) data

Product from TRMM has been widely used for drought monitoring from climatological perspective (AghaKouchak et al., 2015; Immerzeel et al., 2009; Penatti Costa et al., 2015; Sahoo et al., 2011). Monthly precipitation data which is the TRMM 3B34 product were obtained from NASA data center to indicate the climatological background of the study area over the period of 2009 -2017. The data were processed with Version 7 TRMM Multi-Satellite Precipitation Analysis (Tropical Rainfall Measuring Mission (TRMM), 2018).The resolution of the data is 0.25°.

4.2.2.6 Simulated evaporation and soil moisture data

Global Land Data Assimilation System (GLDAS) employs advanced land surface modeling like Noah, CLM, VIC, and Mosaic land surface models and data assimilation techniques to yield optimal 1979-present fields of land surface states and fluxes in near-real time on global scale (Rodell et al., 2004). The system integrates observation-based precipitation, downward radiation products and the best available analyses from atmospheric data assimilation systems. The surface climatological results produced by GLDAS include snow cover, snow water equivalent, soil moisture, surface temperature, and leaf area index. The high-quality, global land surface fields provided by GLDAS support several current and proposed predictions on weather and climate, water resources applications, and water cycle investigations. The data used in this study are the Noah model yielded monthly evapotranspiration and 0-10 cm soil moisture, with resolution of 0.25 degree and temporal range of 2009-2017.

4.2.2.7 In situ data

Water Resources Management Company of Ceará (COGERH) monitors the strategic reservoirs in the federal state of Ceará as the state water agency. For most of the reservoirs it monitors, GOGERH conducts the topography survey before the reservoir construction, and thus obtains

the reservoir bathymetry and the water level-area-storage relations (COGERH, 2018). In addition, GOGERH routinely collects the daily water level measurements for these reservoirs. In this study, the water level-area-storage relations and the daily water levels were provided for the three reservoirs Fogareiro, Sousa and Caracas (Figure 4.1). The water level measurements for the first two reservoirs range from 2009-01-01 to 2017-12-31, and for the reservoir Caracas the available water level measurements range from 2009-01-01 to 2012-02-27.

4.2.3 Method

4.2.3.1 Reservoirs bathymetry derivation

DEMs were generated from each of the TanDEM-X scenes with single pass interferometry by following the workflow in Zhang et al. (2016), with the offset removal reserved. The interferometry was realized in GAMAM software (Werner et al., 2000). Among the DEMs generated from TanDEM-X in the same geometry, the one with least HoA were selected and mosaicked with its counterpart from other geometries for further bathymetry derivation. On such-derived DEMs, the areas of coherence less than 0.6 were regarded as open water and/or areas deteriorated by rough terrains. The elevations of these areas were replaced with the minimum of the surrounding elevation. As a result, in the reservoir where open water retained during the acquisitions of TanDEM-X data the elevations of the pixels at the open water surface represent the contemporary water level.

In the study of Zhang et al. (2016), the generated DEMs were validated only for Madalena region. However, the data used in this study have different HoAs, and this study covers four regions of slightly different topography. Therefore, instead of directly adopting the accuracies established by Zhang et al. (2016) for the single region, we validated the DEMs generated in this study with the global TanDEM-X DEM. Before the validation, invalid areas in either of the two DEM data sets were masked out. Specifically, areas of coherence less than 0.6 indicate the invalid elevation in the DEMs generated in the study, and the data quality maps delivered together with global TanDEM-X DEM position the invalid elevation in the product. The DEM

validation was conducted within the buffered zones of the maximal water mask. The reasons of undertaking the evaluation in this manner are: 1) the bathymetry is only inside the reservoir; 2) the areas far away from the drainage network are possibly characterized by terrains not relevant to the reservoir bathymetry. The absolute accuracy and the relative accuracy were established according to Rosen et al. (2000).

4.2.3.2 Water surfaces from RapidEye images

Top of atmospheric reflectance was obtained for each RapidEye image. For each RapidEye tile a cloud-free reference image was selected and subsequently shifted to match the topography represented by the DEM generated in the study. The process was conducted in ARCGIS (ESRI, 2011) with the assistance of visual inspection. All RapidEye images from the same tile were co-registered to the corrected reference image with algorithm AROSICS (Scheffler et al., 2017).

Water surfaces were delineated from each RapidEye image in the time series. In the leaf-off season, vegetation zone in water bodies like wetland show distinct spectrum from terrestrial objects (Carter, 1982). Based on this, water surface beneath the vegetation were obtained with normalized differential vegetation index (NDVI) (Zhao et al., 2011). In this study, the areas where normalized differential water index (NDWI) > 0 were denoted as open water, and the areas of NDVI > 0.4 as the water surface covered by vegetation, i.e. emergent and floating macrophytes in the reservoirs. From individual RapidEye image, open water and vegetation zone in the adjacency were obtained separately, and then aggregated to produce water surface captured by this image. Subsequently, a filtering with the buffered maximum water mask was applied to eliminate the possible contamination of clouds, shadow etc. Water surface from RapidEye images acquired in the same year were aggregated to mitigate the data gaps caused by the constrained of 10% clouds coverage. This water surface represents the complete maximal water surface that any optical archive can provide in the length of the time series 2009-2017 for all the reservoirs in the four regions. Only data in the dry season were used

considering availability of the data, and also that the water availability is more concerning in the dry season than in the wet season. Ultimately, the water surfaces of high resolution were generated for the four regions on annual frequency.

4.2.3.3 Water storage extraction

The surface water storages were derived from the DEM using the water surface from the RapidEye images. Before the surface water storage extraction, the DEMs were resampled to the same pixel size as the RapidEye images. The co-current water level was determined by the mean of the elevation underlying the water/land borders, i.e. the water extent derived from RapidEye data set. The surface water storage in a reservoir was obtained as shown by the equation below:

$$V = \sum_{i=1}^{n} (H_i - H_w)A \quad with\ H_i > H_w \tag{4.1}$$

where V is the water storage corresponding to the water surface extracted from RapidEye images mapping the reservoir in a certain year; H_i is the elevation of the pixel beneath the water surface yield from the RapidEye images mapping that reservoir in that year; H_w is the co-current water level of the reservoir; n is the total number of the water surface pixels; A is the pixel area of the RapidEye images.

The accuracy of the extracted storage is defined as:

$$\delta V = 0.95^n \sum_{i=1}^{n} (\delta E_i A_{DEM}) \tag{4.2}$$

Where δE_i is the relative accuracy established for the pixel Number i on the DEM generated in this study, 0.95 is the confidence level at which the DEM accuracy was established. A_{DEM} is the pixel area of the DEMs generated in this study.

4.2.3.4 Gridding

In order to eliminate the impact of reservoirs size difference on the illustration of the results on

spatial scale, we presented the derived results relevant to the surface water storage in a grid form. The size of grid cell was set to be 5×5 km based on the following concerns: 1) to respect the dense distribution of water bodies in the regions, as overlarge grid cells may introduce the overlaid effect of the large and the neighboring small reservoirs. 2) The medium reservoirs in the region are about 2-3 km long, the grid cell should respect the size of the reservoirs. The overall extent of the grid was determined by the RapidEye tiles covering the four study areas. The parameters attributed to the grid cells include maximal surface water storage in the period 2009-2017, storage/area ratio, annual surface water storage, and the change rate of surface water storage in the same period. The maximal surface water storage of the grid cell is the sum of the maximal surface water storage of the reservoirs whose geometric centroids fall in the extent of the grid cell. The annual surface water storage of the grid cell was attributed in the same manner. Storage/area ratio of the grid cell was calculated based on its maximal area and maximal surface water storage. The temporal change rate of surface water storage was fitted grid cell-wise in the four regions.

4.3 Results

In this section, we presented the results on the assessment of the DEM generated for reservoir bathymetry representation, the spatial distribution of surface water storage, and the temporal variation of the surface water storage on overall and local scales in the four regions.

4.3.1 Reservoir bathymetry from TanDEM-X DEM

4.3.1.1 TDX DEM validation

The DEMs generated from TanDEM-X data were validated against the global TanDEM-X DEM product. The absolute accuracies of DEM are in the range of 3-6 m, and the relative ones are in the range of 1-5 m (Table 4.2). DEMs from the same geometry have nearly the same absolute and relative accuracies. The DEMs of the largest relative accuracies are in the Bengue region.

Table 4.2 The accuracy of the DEMs generated in the study

	Bengue			Madalena	Sangue			Pentecoste		
Date of acquisition (MM/DD)	10/14 10/25 11/05 11/16	12/30	11/25 12/08 12/19	10/14 10/25 11/05 11/16	11/27 12/08 12/19	11/09 10/20 10/31 11/11	11/22 12/03 12/14	11/27 12/08 12/19	10/14 10/25 11/05 11/16	12/30
absolute accuracy (m)	6.09 6.12 6.01 5.99	5.36	5.24 5.24 5.02	4.10 4.10 4.09 4.18	3.30 3.35 3.45	3.28 3.31 3.74 3.32	3.33 3.20 3.14	5.02 5.76 5.71	6.00 5.98 5.19 5.82	5.08
Relative accuracy (m)	5.11 5.14 5.10 5.00	4.2	4.24 4.2/ 4.0	2.47 2.48 2.45 2.59	1.84 1.50 1.79	2.30 2.35 2.38 2.36	2.01 2.41 2.39	2.93 2.57 2.46	1.66 1.64 2.66 2.49	2.01

4.3.1.2 Impact of remaining water on derived reservoir bathymetry

Figure 4.2 shows the areal percentages of the remaining water in the reservoirs during the acquisitions of TanDEM-X data in the four regions. The remaining water surfaces indicate the area where the bathymetry derivation failed. The majority of the reservoirs (65%-92%) were empty during October-December 2015, with remaining water accounting for approximate 0% of the reservoir's maximal area. In only few reservoirs (~ 5%) the areal ratios of the remained water were larger than 50% (Figure 4.2). In fact, the reservoirs with large area of remaining water were the very small ones. Some the large ones which were often monitored by the local authorities were empty or have remaining water surface less than 50% during the TanDEM-X data acquisition (Figure 4.2). This indicates: 1) DEM generated in this study can effectively represent the full bathymetry for the majority of the reservoirs in the region; 2) these regions have suffered from a severe drought in October-December 2015.

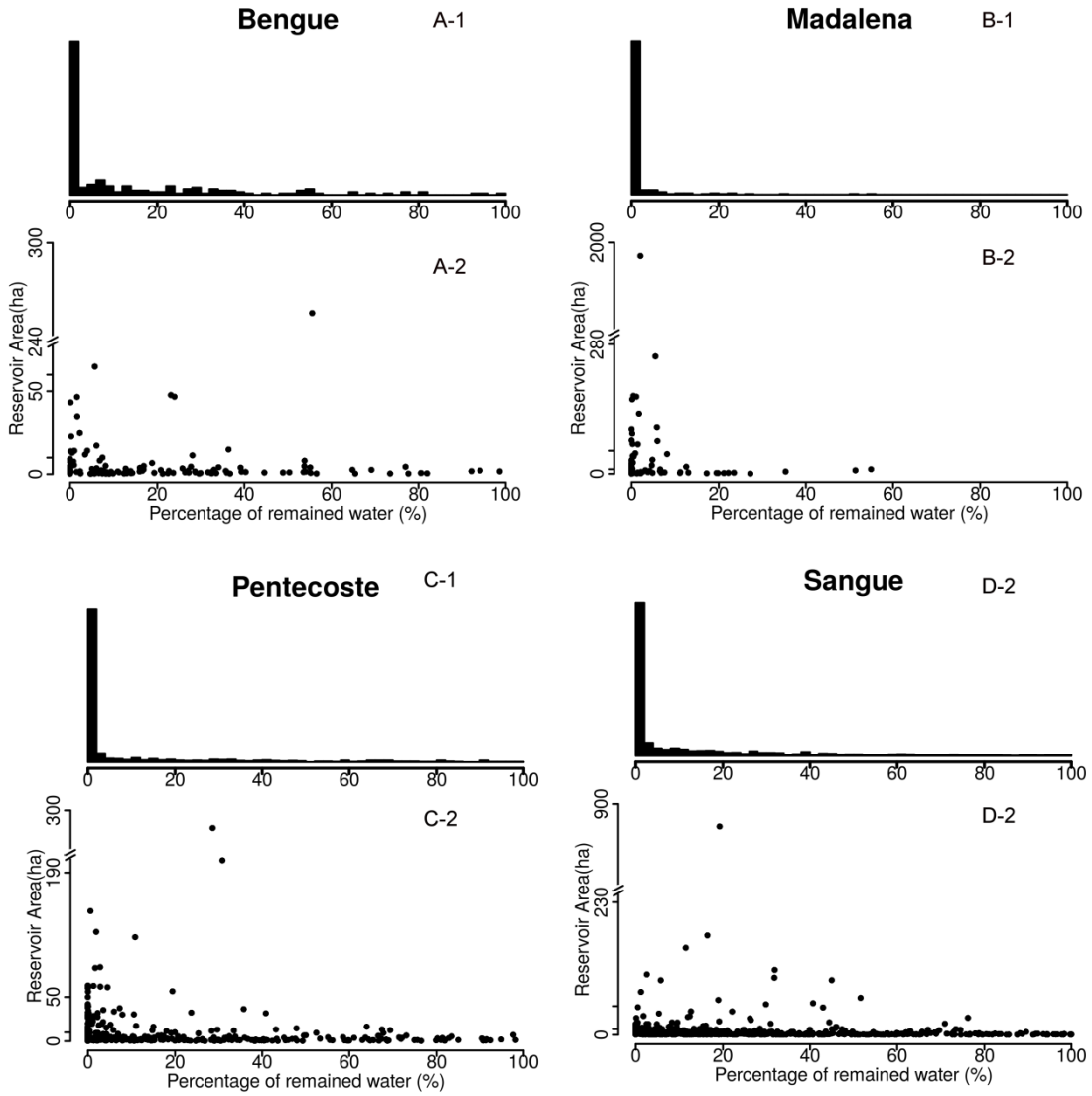

Figure 4.2 The areal percentage of water remained in the four regions. The second and third ticks on the Y-axis of the scatterplots are at the position of 10 ha and 50 ha, corresponding to the classes of the reservoirs.

4.3.2 Spatial characteristics of water surface storage

4.3.2.1 Composition of surface water in the four regions

Table 4.3 shows the overall constitution of water bodies in the four regions. In total, there are 2 105 reservoirs in the four regions and classified into four classes according to their sizes (Figure 4.3). In general, the small reservoirs (<10 ha) account for the largest proportion of the reservoir population but contribute the least to the regional surface water storage, vice versa. For example, the small reservoirs (< 10 ha) account for 87%-94% of the water bodies, 4%-29% of surface water storage. Large reservoirs (>10 ha) account for 5%-13% of the water bodies but

contributed 68%-95% of surface water storage (Table 4.3).

The regions are impounded with high density. On average, there is 0.04-0.23 reservoir in every square kilometer. The water surface correspond to this density is 0.23-3.35 hectare (ha) /km^2, and the correspondng surface water storage is 0.01-0.17 hm^3/km^2. Among the four regions, the Bengue region is the least densely impounded, and the Sangue region is the most densely dammed. Madalen and Pentecoste have similar overall reservoir densities (Table 4.3).

The surface water storage capacities in the regions Bengue, Madalena, Pentecoste and Sangue are 26.00, 358.92, 218.94, 190.07 hm^3, respectively. The Madalena region is the smallest among the four regions (Figure 4.1), but it potentially stores the most surface water (Table 4.3). The regions Pentecoste and Sangue have very large numbers of the reservoir and the water surface, but relatively fewer surface waters storage capacity than the Madalena region (Table 4.3).

Table 4.3 The potential contribution of reservoirs to the region water resource in the four regions.

		Bengue		Madalena		Pentecoste		Sangue	
		Total	Percentage (%)	Total	Percentage (%)	Total	Percentage (%)	Total	Percentage (%)
Number	< 1	79	49.06	91	35.41	202	31.42	503	48.13
	1 - 10	69	42.86	132	51.36	361	56.14	488	46.70
	10 - 50	11	6.83	22	8.56	64	9.95	46	4.40
	> 50	2	1.24	12	4.67	16	2.49	8	0.77
	In total	161	100	257	100	643	100	1044	100
	Density (/km^2)	0.04	-	0.16	-	0.13	-	0.23	-
Area (ha)	< 1	36.75	4.80	67.39	1.04	131.34	2.16	321.28	5.63
	1 - 10	181.33	23.70	727.70	11.17	1483.52	24.38	1981.41	34.70
	10- 50	209.99	27.45	817.15	12.55	1724.56	28.34	1301.78	22.80
	> 50	337.03	44.05	4898.43	75.24	2745.95	45.12	2105.81	36.88
	In total	765.09	100	6510.67	100	6085.38	100	5710.28	100
	Density (ha/km^2)	1.86	-	4.13	-	1.18	-	1.25	-
Surface water storage (hm3)	< 1	0.28	1.06	0.64	0.18	1.10	0.50	2.89	1.52
	1 - 10	3.17	12.19	14.96	4.17	27.66	12.64	32.40	17.05
	10- 50	5.95	22.90	28.14	7.84	55.42	25.31	37.63	19.80
	> 50	16.60	63.84	315.16	87.81	134.76	61.55	117.15	61.63
	In total	26.00	100	358.92	100	218.94	100	190.07	100
	Density (hm^3/km ^{2})	0.01	-	0.23	-	0.04		0.04	-

4.3.2.2 Spatial characteristic of surface water storage within regions

Figure 4.3 shows the spatial distributions of surface water storage in the four regions on the scale of 5×5 km grid. A few gaps present in the grids over the four regions (Figure 4.3). This coincides with the result in Table 4.3, and indicates that the regions are densely impounded. Among the four representative regions, Sangue is most densely impounded, followed by Pentecoste, Madalena and Bengue (Figure 4.3).

Reservoirs in the majority of the grid cells are of surface water storage 10^4-10^7 m^3 and

distributed in the upper and middle streams of the drainage systems. Reservoirs at the outlets claim the largest surface water storage, ranging from 10^7 to 10^9 m^3 (Figure 4.3). However, reservoirs of storages up to 10^7 m^3 were also constructed in the upper and middle reaches of the Madalena, Pentecoste and Sangue regions (Figure 4.3). The distributions of surface water storage in the four regions show high spatial heterogeneity.

For the grid cells in all the representative regions, the accuracies of the maximal surface water storage are in the range of 0-250 m^3 (Figure 4.3 B, E, H and K), which is very high in comparison to the estimated maximal surface water storage (Figure 4.3 A, D, G and J). For the majority of the reservoirs, the accuracies of surface water storage are 0-20 m^3, including those of surface water storage up to 10^{10} m^3 (Figure 4.3 B, E, H and K).

The storage/area ratio of a grid cell is related to the morphology of reservoir whose centroid falls in the grid cell and positions the areas where discrepancies may take place between the water resource estimated from area and volume. Overall, larger storage/area ratios present in grid cells of large surface water storage, with few exceptions in the upstream of the regions (Figure 4.3 C, F, I and L).

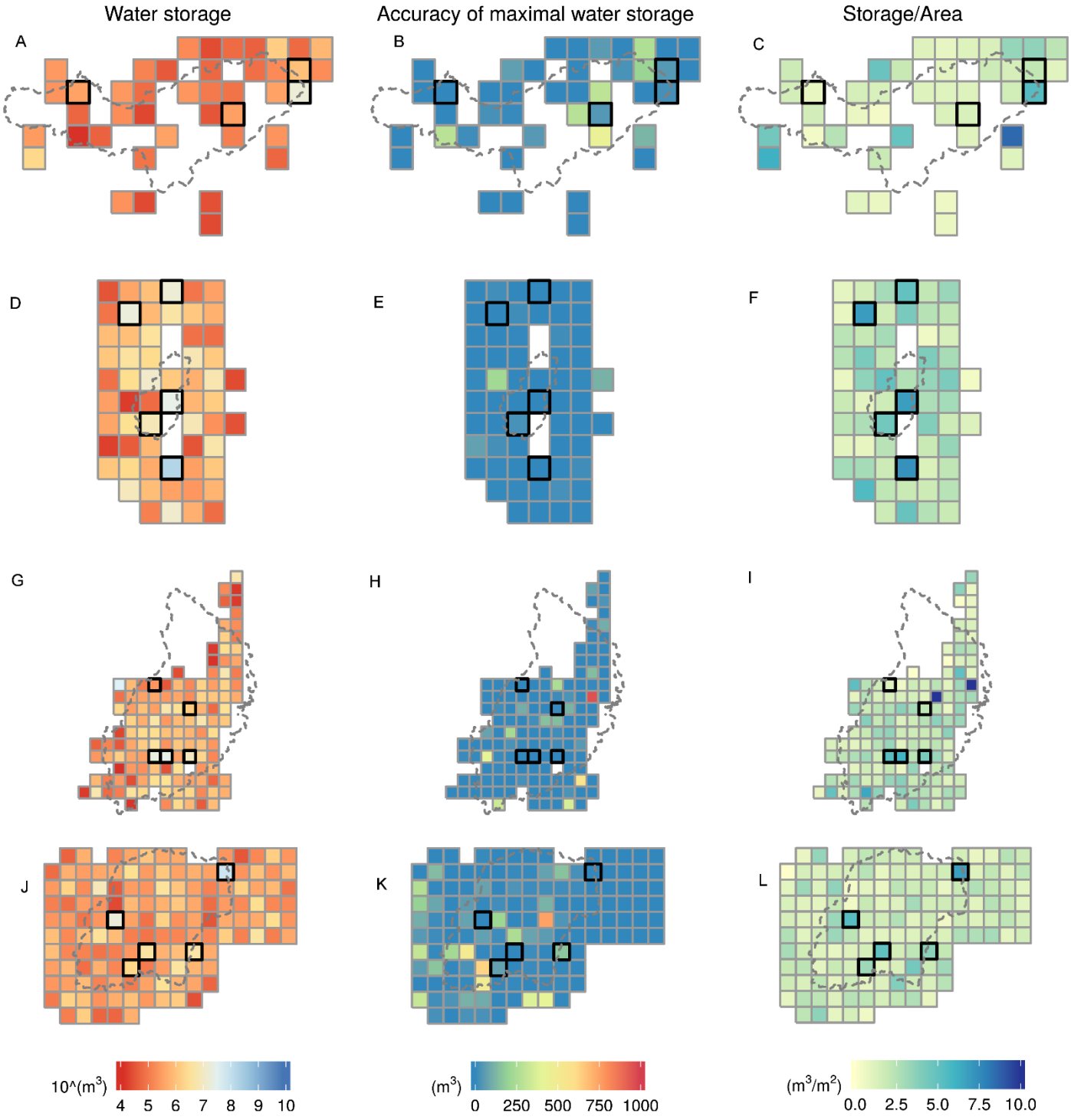

Figure 4.3 The spatial distribution of maximal surface water storage, area, and the ratio of maximal water storage and area in the 5×5 km grids over the four regions. The gaps in the grids indicate that no reservoir's centroid falls in those grid cells. Black squares indicate the cells selected to show the temporal variation of local surface water storage.

4.3.3 Temporal variation of surface water storage

4.3.3.1 Temporal variations of precipitation deficit and surface soil moisture

The four regions have similar precipitation deficits (i.e. precipitation - evaporation) over the period of 2009-2017 (Figure 4.4 A). The Bengue region presented the smallest soil moisture, and the other three regions had similar and higher soil moisture than the Bengue region (Figure 4.4 B). The change directions of the precipitation deficit and the soil moisture were well synchronized (Figure 4.4 A-B). Two significant drops took places in the precipitation deficit and soil moisture in all the four regions in 2005-2007 and 2012-2015. In addition, both the precipitation deficit and the soil moisture presented a drastic sub-drop in 2010. The soil moisture in the four regions showed faster recoveries than the precipitation deficit. For example, after the drop at 2012, the precipitation deficit remained very low and even showed further decreased in 2016, but the soil moisture in all the four regions tended to resume already in 2013, and in 2017 it nearly reached its magnitude during 2009-2013.

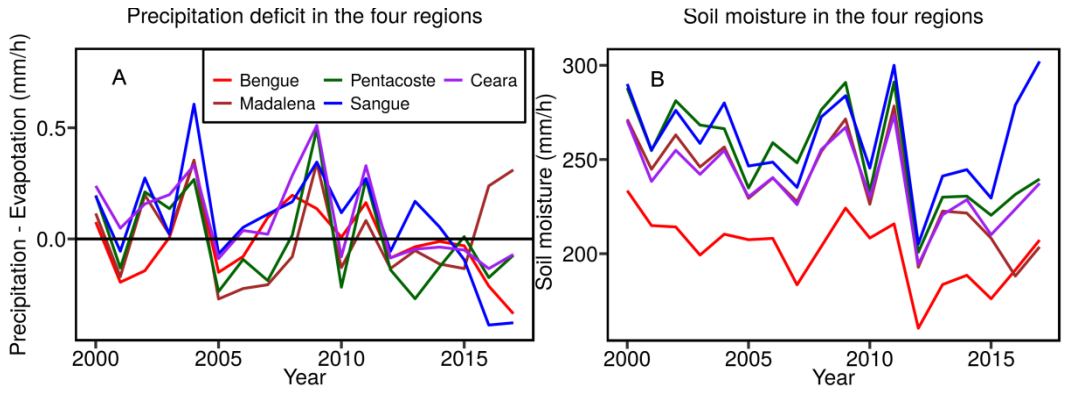

Figure 4.4 Temporal variations in the annual mean precipitation deficit (A) and the annual mean soil moisture (B) in the four regions in the period of 2009-2017.

4.3.3.2 Temporal variation of overall surface water storage in the regions

From 2009 to 2017, the total number, area and storage of water bodies decreased continuously in the Madalena, Pentecoste, and Sangue regions, but with slightly different trajectories.

In Bengue, the total number of water body reached the minimum in 2013 and resumed in 2014. Surface water area and storage showed continuous decrease, slightly fluctuated in 2016, and

increased in 2017 (Figure 4.5). Surface water storage showed a slight increase in 2010. In total, the amount of the surface water lost in the region during last eight years was 220 ha by area and 12 hm^3 by volume. The reservoirs 10-50 ha responded to the precipitation deficit increase in 2013/2014.

In the Madalena region, the number of water body showed an overall decrease from 2009 to 2017, and a fluctuation in 2014. In 2017, the number of the reservoirs resumed to approximately 150. The area and storage of surface water showed drastic and continuous decreases in the period 2009-2016, and then a slight resilience in 2016/2017. From 2009 to 2017, this region lost surface water of approximately 6 000 ha by area and approximately 300 hm^3 by volume.

In Pentecoste, the number, area and storage of surface water bodies showed continuous decreases until 2017, and the decreases accelerated from 2010. From 2009 to 2017 the total water loss in this region was approximately 4 000 ha by area, and approximately 200 hm^3 by volume (Figure 4.5).

In the Sangue region (Figure 4.5), the number, area and storage of surface water showed first slight increases in 2011, and then continuous decreased. From 2016 to 2017, there was a slight increase in the number and area, but not in water storage. By the year of 2017, the loss of surface water in the region was approximately 6 000 ha by area and approximately 110 hm^3 by volume.

In summary, the changes of the reservoirs numbers in the four regions were mainly reflected by the reservoirs < 10 ha, and the reservoirs >10 ha, particularly those > 50 ha, reflect the changes in the water surface and the storage in the four regions.

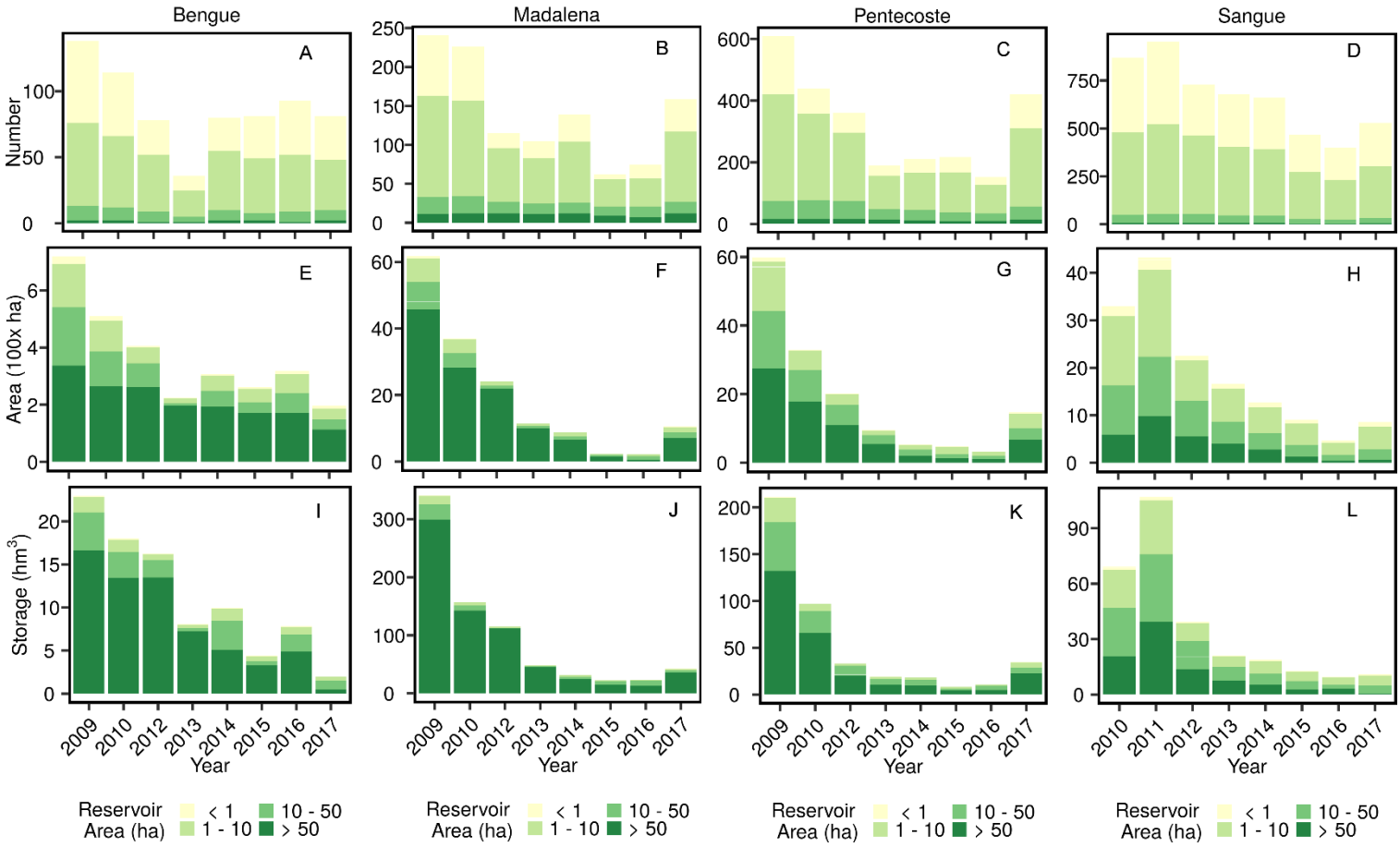

Figure 4.5 Temporal variations in the total number, area and storage of water bodies in the four regions.

4.3.3.3 Spatial heterogeneity of temporal variation of surface water storage

The overall variation of surface water storage in the four representative regions in the period 2009-2017 showed that 2010, 2013, and 2015 could be the critical years in the temporal dynamics of surface water in NE Brazil (Figure 4.5). Therefore, the surface water storages in the three years were selected to show their spatial characteristics in the four regions (Figure 4.6) and indicate the spatial characteristics of surface water storage variation in NE Brazil.

In the Bengue region, while the overall surface water storage decreased in the period of 2009-2017 (Figure 4.6), the reservoirs in the upstream of the region dried up first (Figure 4.6 A-C). Dramatic decrease were shown from 2011 to 2013. From 2013 to 2015 the surface water storage showed slight spatial change (Figure 4.5 B-C). Some small reservoirs in the midstream and upstream which were empty in 2013 were refilled in 2015. Meanwhile, the surface water

storage in the reservoir at the outlet showed a significant drop between 2010 and 2015 (Figure 4.6 A-C).

In the Madalena region, from 2010 to 2013 the dry-up appeared mainly in the reservoirs in the upper and middle reach. Most of the reservoirs in the upper and middle reaches experienced decrease-and-refill process. Some small reservoirs in the upper and middle streams were refilled in 2015. Barely some surface water presented in the lower reach of the region in 2015. All the large reservoirs undertook significant water loss and present their minimal surface water storages in 2015. Large reservoirs undertook remarkable water loss. Some relatively large reservoirs in the catchment even become empty by 2015.

In the Pentecoste region, as the overall surface water storage decrease during the period of 2009-2017 (Figure 4.5 C, F and I), dry-up presented in reservoirs in the upstream of the catchment in 2013 and intensified in 2015. A few small reservoirs which were dry in 2013 were refilled with little water in 2015 (Figure 4.6 D-F). Significant decrease of surface water storage took place in all the reservoirs during the period, particularly in the largest one (Figure 4.6 D-F).

Very drastic loss of surface water took place in the entire Sangue region in the period of 2010-2013 (Figure 4.6 J-L). From 2013 to 2015 the surface water storage in the region remained very little (Figure 4.6 K-L). The region presented fewer empty reservoirs than other three regions, as only a few areas at the upstream of the catchment presented no water in 2015.

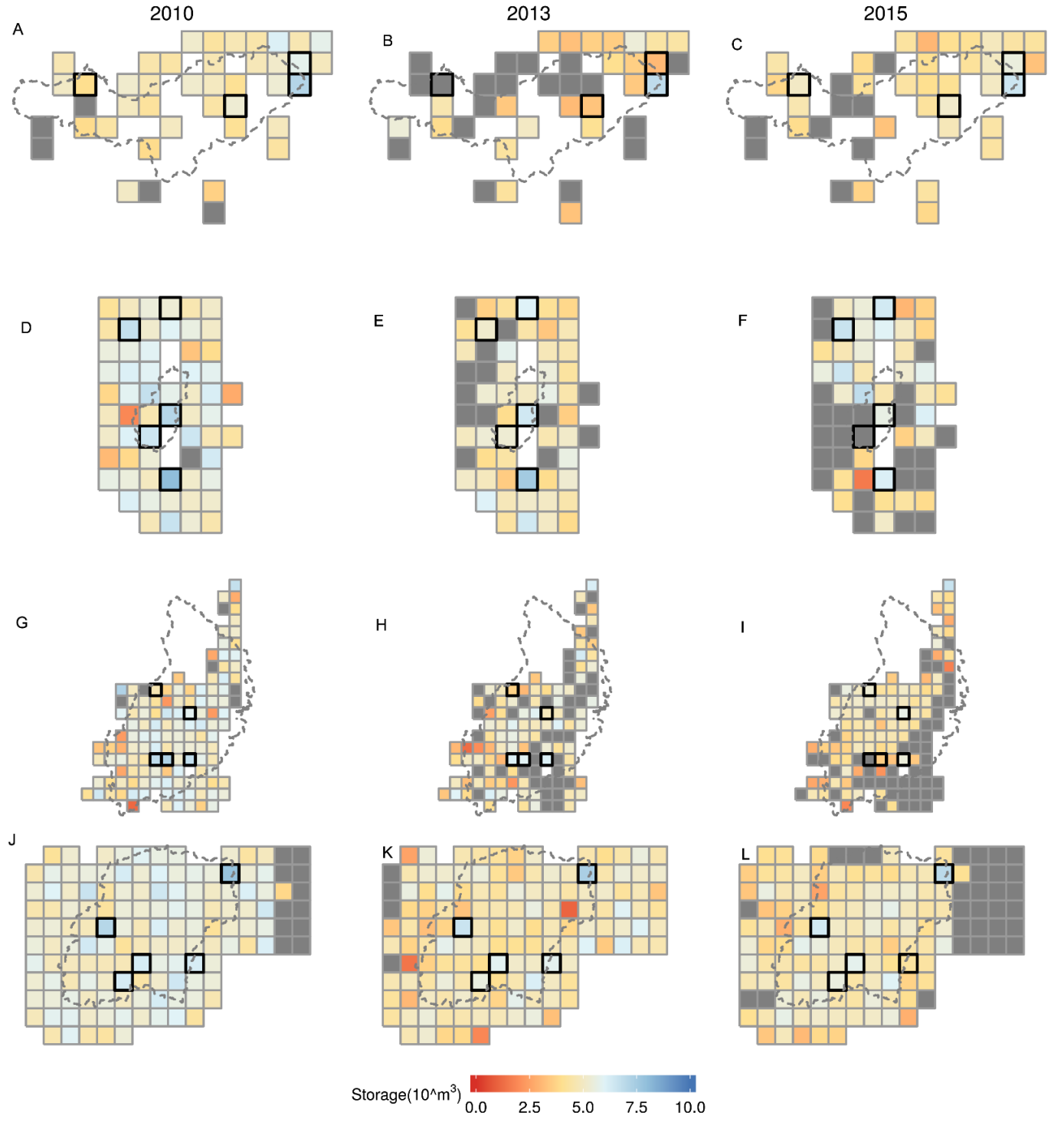

Figure 4.6 The spatial distributions of surface water storages in the four regions in 2010, 2013 and 2015. Gray grid cells indicate that no surface water appeared in that grid cells in the corresponding years

Figure 4.7 shows the change trajectories of the surface water storage along the time series in the highlighted grid cells in Figure 4.3. The surface water storage in the areas selected from

Bengue region have relatively small storages and responded to the decrease in precipitation deficit in the region in 2012/2013. Some reservoirs even dried up in 2013 and were refilled in 2015/2016 (Figure 4.7 A and E). In Madalena region the surface water storages in individual reservoirs have decreased since 2009, and the decrease rate accelerated in 2013 (Figure 4.7 B and F). A few reservoirs in the region slightly responded to the increase in the precipitation deficit from 2014/2015 and showed increased surface water storage (Figure 4.7). All the reservoirs in the grid cells selected from the Pentecoste region showed decreased surface water storage (Figure 4.7 C and G). From 2010, the decrease rates of surface water storage in the large reservoirs in the region accelerated in 2010. The surface water storage in the small reservoirs (< 10 ha) remained rather stable or decreased slowly (Figure 4.7 G). From 2016 on, gentle increases presented both in the small and the large reservoirs which were in the middle stream of the catchment from 2016 on (Figure 4.7 C). The surface water storage in the grid cells selected from Sangue region showed slight increases from 2009 to 2011 and drastic decreases from 2011 (Figure 4.7).

The slightly different trajectories (Figure 4.7) indicate the heterogeneous interactions between the reservoirs recharge and local water depletion. The large reservoirs supporting the nearby towns showed dramatic and continuous decreases and responded to the increases in the local precipitation deficit. Small reservoirs responded instantly to the local precipitation deficit variations.

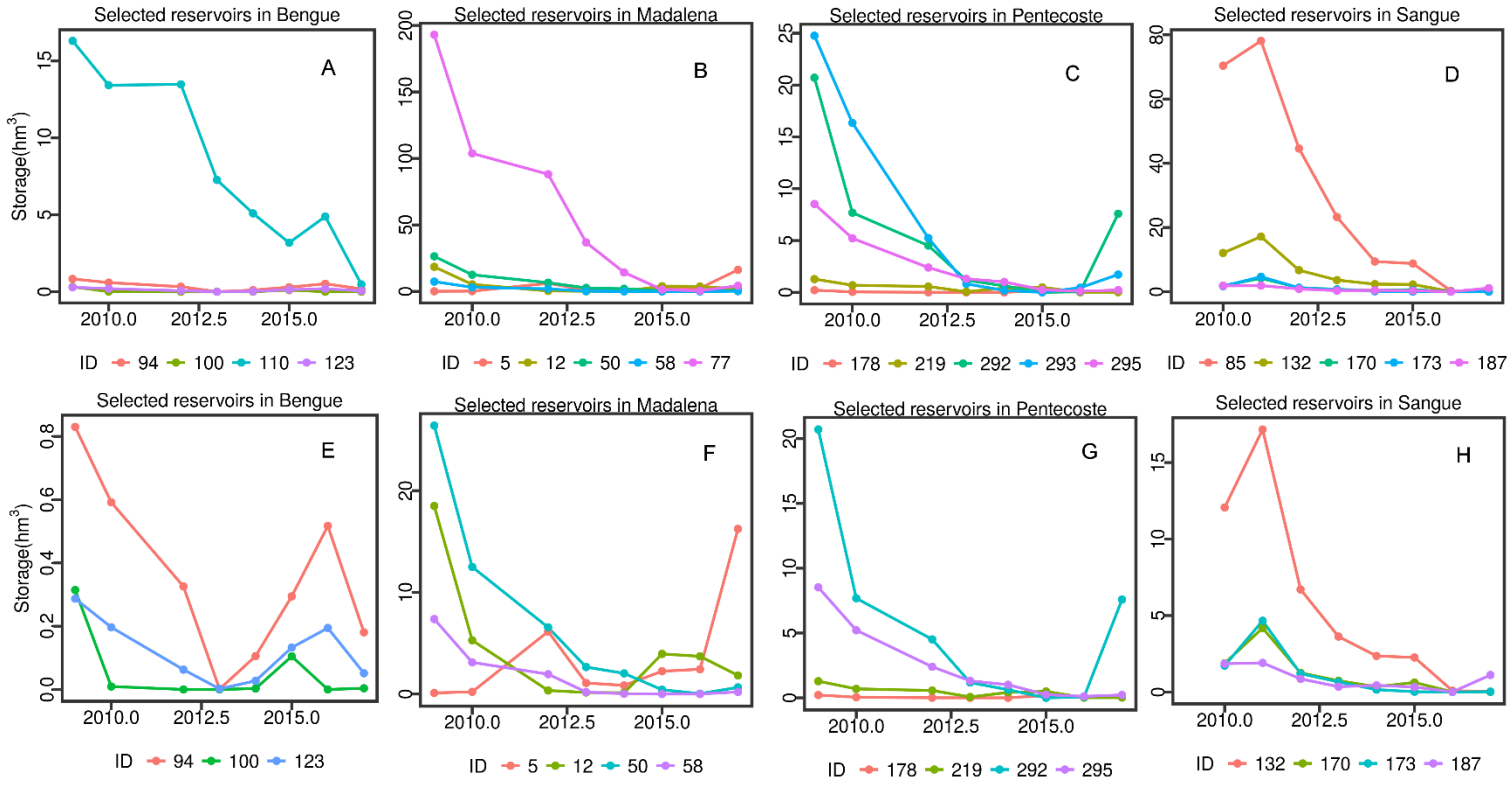

Figure 4.7 The change trajectory of the water storage in reservoirs in the grids indicted in Figure 4.3 in the four regions. ID in the legend means the position of the cell in the grid covering the region. The grid in the top left has the smallest grid ID and the bottom right has the largest one. The sub-figures E-H present the zoom-ins of sub-figures A-D, and focus on the small reservoirs

4.3.3.4 The year of minimum surface water storage

As the reservoirs in the four regions took different trajectories (Figure 4.7), the year of minimum surface storage in each subset are depicted (Figure 4.8), regardless the seasonal variation. When extracting the year of the minimal surface water storage for the reservoirs in the grid cells, if the reservoirs in the grid cells had reached their minima more than once, including dry-up, the first occurrence was taken.

In Bengue region most of the reservoirs which are small than 10 ha reached the (first) storage minimum in 2012/2013, and these at the outlets and a few in the catchment presented the storage minima in 2017 (Figure 4.8 A). The majority of the reservoirs in the upper reach of Madalena region presented their storage minima in 2012/2013, and those in the downstream showed their minima in 2015/2016 (Figure 4.8 B), following the change trend of overall

surface water storage in Figure 4.5. In the mapped area of the Pentecoste region, the minimal storage occurred in all the years in the times series, without clear spatial clustering (Figure 4.8 C). In Sangue region, the reservoirs in middle stream and the boundary areas of the catchment presented storage minima in 2012/2013. The rest of the region reached their minima in the surface water storage in 2016/2017 (Figure 4.8 D) when the precipitation deficit in the region showed its minimum of the past eight years (Figure 4.4).

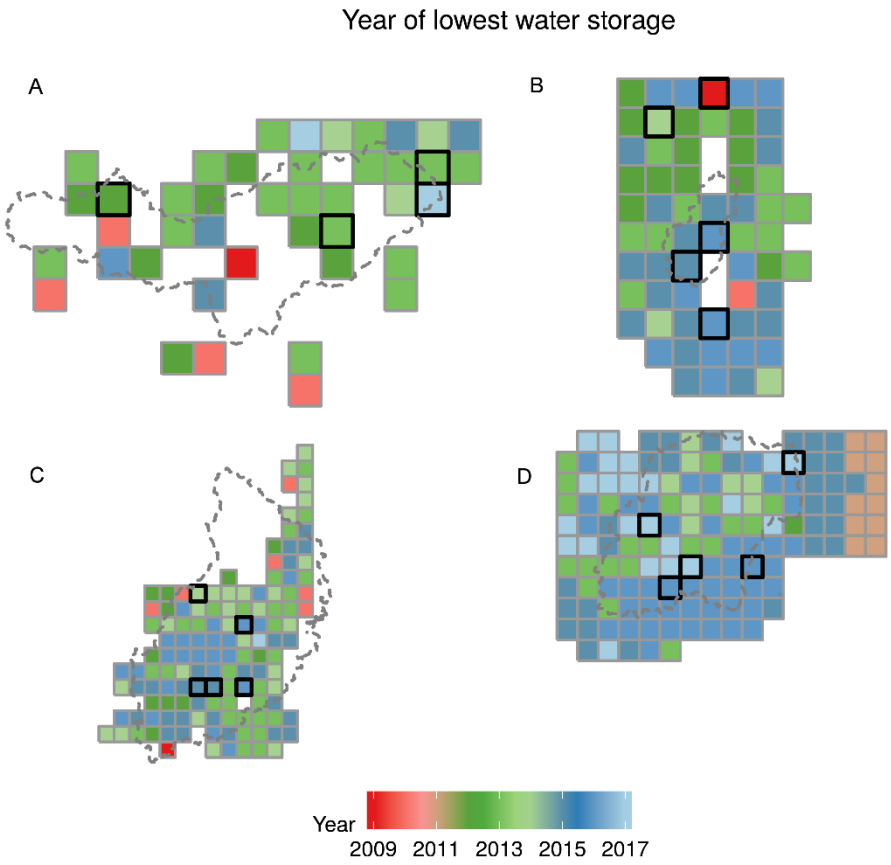

Figure 4.8 The year of lowest surface water storage in the four regions

4.3.3.5 The change rate of surface water storage

The surface water storages in the four regions have shown overall decreases in the period of 2009-2017, with few exceptional areas in the Madalena and Bengue regions (Figure 4.9). Moreover, the decrease trend presented spatial heterogeneity, suggesting unevenly distributed water depletion stress. The water loss in the areas where large reservoirs are located was the

most significant and up to -10^8m^3/year (Figure 4.9). It suggests that large reservoirs undertake more water extraction pressure than other reservoirs. In contrast, small reservoirs show less significant water loss over the time series. For most the areas, the change rate of surface water storage from 2009 to 2017 lies at approximately -10^5 m^3/year in the spatial range of 5×5 km (Figure 4.9). A few areas in the upper/middle reaches of Bengue, Madalena and Pentecoste regions where mainly the small reservoirs were constructed even showed increased surface water storages (Figure 4.9 A-C).

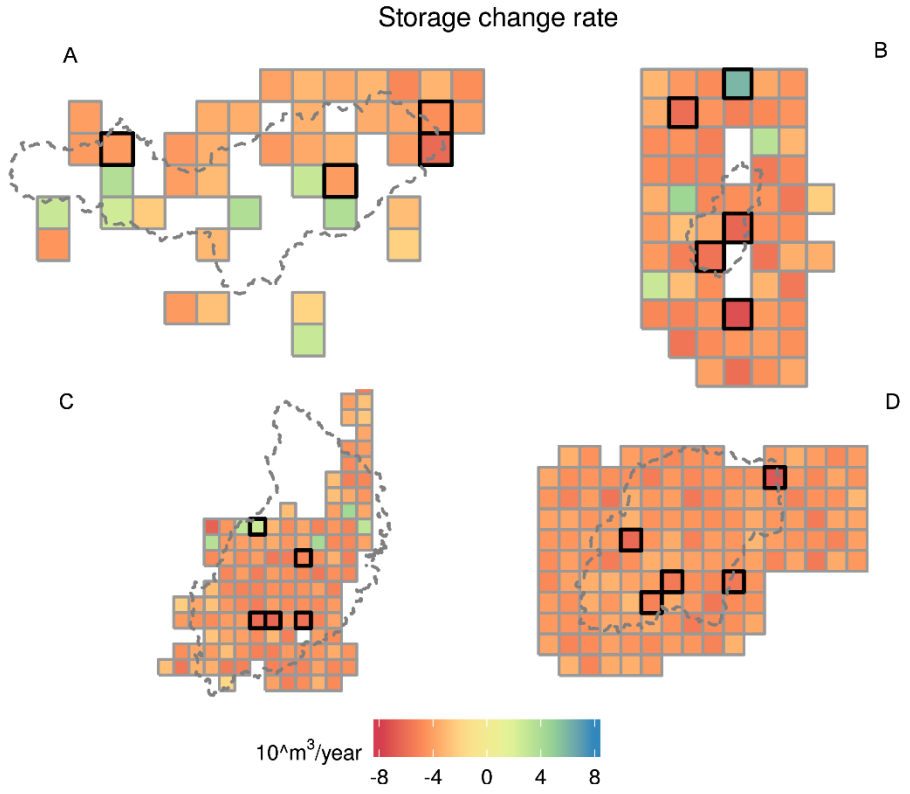

Figure 4.9 The spatial distribution of water storage changes in the regions. The signs in the legend define the change direction, namely, -10 means the surface water storage decreased by 10^{10} m^3/year and 10 means it increased by 10^{10} m^3/year.

4.3.4 Validation surface water storage with in-situ data

The surface water storages derived with remote sensing images are compared to those derived from inventory data and in-situ measurements (Figure 4.10). The surface water storages derived

from annual water masks were attributed to all the days in the dry season, namely, in that year all the days after 1st July have the same surface water storage. The surface water storages of those days correlate to the maximal water surface captured by the RapidEye images in the dry season of that year. Meanwhile, for the first half of the year the surface water storage in the reservoirs were not estimated. During the validation, the surface water storages derived in this study were regarded to be consistent with the results derived from in-situ measurement, if the two results for the same year meet each other in the range of the year.

Overall, in the reservoir Fogareiro, Sousa, and Caracas, the surface water storages derived in this study match well with that obtained from in-situ measurements, and the two results showed the similar patterns (Figure 4.10). For the reservoir Caracas, the remote sensing derived surface water storage can fill the gaps where the in-situ measurements were not available (Figure 4.10 C).

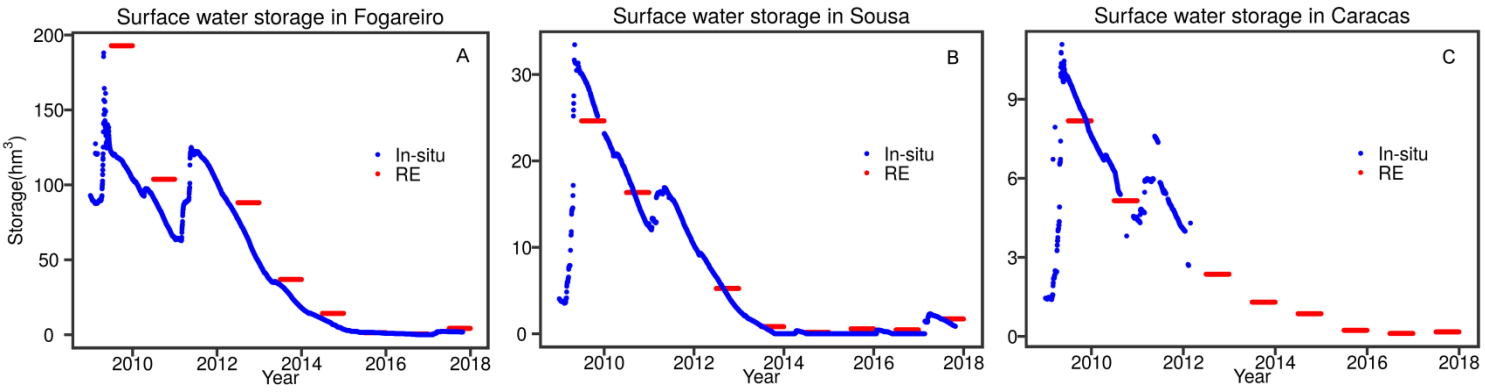

Figure 4.10 Comparison of surface water storage derived in this study with in-situ measurements. The reservoir Fogareiro is in Madalena region, and the reservoir Sousa and Caracas are in the Pentecoste region (Figure 4.1).

4.4 Discussion

4.4.1 TanDEM-X derived DEM and reservoir bathymetry

TanDEM-X data acquired during the low water level were used to generate DEM and represent the bathymetry for reservoirs in four representative regions in NE Brazil. With accuracy of 2-5 m relative, the bathymetry is the best for the reservoirs in the region on such scale in comparison other existing DEMs such as SRTM DEM which was adopted by Avisse et al.

(2017). However, the accuracy were established by referring to the global TanDEM-X DEM whose accuracy is at 10 m for absolute and two meters in relative aspect (Wessel et al., 2018). So the actual accuracy of the bathymetry is possibly better than the established in the study, and potentially can reach the accuracy established by Zhang et al. (2016) for the region Madalena. The large absolute accuracy can be attributed to the SRTM DEM which was used to remove the majority phase of the earth. The relative are probably related to the roughness of the local terrain. The difference between the DEM generated in this study and global DEM can be partly attributed to the land cover (Wessel et al., 2018). As the region is covered by shrubby forest and the TanDEM-X data used for the global DEM product were acquired regardless the time of the year, while the data used for bathymetry representation were derived in the deep dry season when the canopy were open. On the other hand, the baseline of the TanDEM-X used for the DEM generation are very large in comparison to the data used by Zhang et al. (2016), and such yielded DEM are insensitive to the micro-topography around the reservoirs edges. Therefore, the slight topography variation along the reservoirs may have also contributed to the inaccuracy of the DEM generated in this study. Derived from TanDEM-X recently acquired, the reservoirs' bathymetry serves as the most up to date data for these reservoirs. These data of high resolution and accuracy have filled the data gap for the region, ensured the precise estimate on the water storage, as shown in Figure 4.3, and thus provided valuable information for water management in the semiarid northeastern Brazil with high reservoir density.

4.4.2 Bathymetry, surface water storage capacity and spatial-temporal variation of regional reservoirs

In this study we derived the bathymetry for 2 105 reservoirs on regional scale. This data set has enabled to extract the water storage and depict its variations on spatio-temporal scale. Based on this bathymetric data, the potential water storage capacities in the representative regions Bengue, Madalena, Pentecoste and Sangue were estimated to be 26.00, 358.92, 218.94, 190.07 hm^3, respectively (Table 4.3). These data were derived purely from remote sensing data of high resolutions and accuracies. The surface water storages estimated in the study were of high confidence as they were directly derived from the high accuracy topography inside the

reservoirs instead of the surrounding topography as Messager et al. (2016) did. Covering reservoirs smaller than 10 km^2 whose surface water storage have been poorly estimated by Messager et al. (2016), this study provided detailed and complete inventory data for the reservoirs in the regions.

In comparison to those studies only focusing on the volumetric variation in a few large lakes (Duan and Bastiaanssen, 2013; Gao et al., 2012; Zhang et al., 2014), this study derived nearly decadal variation of surface water storage for 2 105 reservoirs of various sizes distributed in four regions of total area of approximately 10 000 km^2 (Figure 4.1, Figure 4.3 and Figure 4.4). The results from this study can be directly used for validating/optimizing hydrological modelling etc. Instead of the total water storage derived from GRACE data which include wet soil and potential ground water (Melo et al., 2016), this study yielded surface water storage. These data sets are the first unprecedented results on such scale for the regional and local water authorities. They can potentially improve the water management for the region and provide insight for the surface water storage characteristic in the entire dryland in NE Brazil.

The validation of the surface water storage with that obtained from in-situ measurements demonstrated the reliably of the surface water storage derived in the study (Figure 4.10). It also implied the potential of future remote sensing monitoring of the reservoirs in the representative areas (Figure 4.10 C).

4.4.3 Controlling factors of the surface water storage change

4.4.3.1 Climate

The surface water storage in NE Brazil had dropped since 2010. The similar trends were also found from the total water storage derived from GRACE data in the reservoirs in southern Brazil (Melo et al., 2016).This result indicates that the drought from 2010 to 2017 was probably a continent-wise drought. The same drought was also noticed in Amazon region revealed by the total water storage deficit (Thomas et al., 2014). Humphrey et al. (2017) used total water storage change derived from GRACE data and found that there is a sub-decadal water storage

variation corresponding to the climate on the global scale.

In this study, the climatological changes in the four representative regions were depicted with the local precipitation deficit (Figure 4.4 A). The precipitation deficit showed significant overall decrease from 2009 to 2017, with slight increase in 2014-2015. The overall surface water storages in the four regions have decreased from 2009 to 2017. Majority of areas in the region presented the minimal surface water storage 2015 (Figure 4.5 and Figure 4.7), which indicates the water scarcity in 2015 is the most severe in the region in the period of 2009-2017. Small reservoirs (< 10 ha) and a few relatively large ones (> 10 ha) constructed in the middle or upper stream also responded to the increase of precipitation deficit in 2016/2017 (Figure 4.7 B, C, F and G). Very likely, the overall surface water storage in the entire NE Brazil also responded in the same manner to the precipitation deficit changes (Figure 4.4 A). In Sangue, the number, area, and storage of reservoirs slightly increased in 2011 (Figure 4.5). No RapidEye images were acquired for the regions Bengue, Madalena, and Pentecoste in 2011. However, if the data were available for the three regions in 2011, the surface water storage there would probably show similar change directions, as the precipitation deficit in the three regions also show similar fluctuations (Figure 4.4).

4.4.3.2 Land use

Weng et al. (2017) found that land use/cover change impact the water availability in Amazon region. The land cover in NE Brazil is mainly Caatinga, the shrub forest, with very sparse farming fields distributed in between (Bullock et al., 1995). However, the federal state Ceará in NE Brazil is hardly farm industry oriented. Field observation found that the existing fields are small patches used by individual households for self-supply. They are often distributed on the exposed reservoirs bottom due to the terrain and barren soil outside of the reservoirs. Therefore, we do not regard significant impact from the land use to the water consumption heterogeneity in the four representative regions.

4.4.3.3 Human activities

The large reservoirs were mainly constructed in the vicinity of the towns which demand large amount of water (Figure 4.1). According to the federal census, there is no significant growth in the population in the four regions (IBGE, 2015). Therefore, the contribution of population growth to the continuously decreased surface water storage is regarded to be ignorable for the four regions.

In the four regions the large number of small ones (< 10 ha) do not contribute significantly to the regional surface water storage (Table 4.3 and Figure 4.5). In contrast, the few large reservoirs (> 10 ha), particularly those > 50 ha, provide more than 90% of the surface water storage (Table 4.3 and Figure 4.5). However, with the high spatial density, wide distribution in the region and small storage/area ratios (Table 4.3, Figure 4.5 and Figure 4.6), small reservoirs probably have contributed to and maintained the surface soil moisture. For example, reservoirs density the Bengue region is the least (Table 4.3), so is the soil moisture in this region (Figure 4.4 B), while the other three regions are of similar reservoir densities as well as soil moisture (Table 4.3 and Figure 4.4 B). This may also explain why the soil moisture recovered so swiftly in the region, while the precipitation deficit remained very low from 2012 in the region (Figure 4.4).

The small reservoirs of high densities in the upstream collect the runoff, and reduce the refill of the large reservoirs downstream, particularly to the large reservoirs downstream and outlets of the regions (Figure 4.3). This phenomenon is more significant in dry years than year of normal precipitation deficit, as very often there is no overflow from small reservoirs. However, the water demand from the nearby towns/settlements remain the same all the years and the water extraction from the reservoir stay constant, regardless the precipitation deficit. This caused the accelerated decrease in the surface water storage in these water bodies in the dry years (Figure 4.5 and Figure 4.7).

In addition, the inhabitants in the regions are supported by different reservoirs. Those in the

towns rely on the large reservoirs which are often situated at the outlets of the catchments. While the inhabitants in the scatters settlements in the rural area are supported by those relatively small reservoirs. As the relatively small reservoirs dry up due to the limited recharge from precipitation and runoff, the water consumption of the remote settlements is supplied by the large reservoirs through mobile water tanks. Therefore, the overlaid effect of decreased regional precipitation deficit and the concentrated water demand from the nearby settlements/towns accelerated the decrease in surface water storage of large reservoirs.

Therefore, the variations of the total surface storage in the representative regions are controlled by overall precipitation deficit in the regions. The small reservoirs (< 10 ha) and a few large reservoirs (> 10 ha) constructed in the upstream responded to the short-term variation in the regional precipitation deficit. The intensive water withdrawal from the large reservoirs in the dry season caused accelerated decrease in the surface water storage in these reservoirs.

4.5 Conclusion and outlooks

4.5.1 Conclusions

The bathymetry of high accuracy was derived for 2 105 reservoirs, regardless of the reservoir size. The bathymetry enabled the derivation of annual surface water storage in the four regions from 2009 to 2017.

Nearly decadal surface water storage changes were derived for the reservoirs in the four representative regions of densely impoundments in NE Brazil. From 2009 to 2017, the surface water storages in the four regions constantly decreased by an average rate of 10^5 m^3/year in the spatial unit of 5×5 km. The four representative regions, very likely the NE Brazil region as well, have suffered from constant drought during this period.

Small reservoirs (< 10 ha) account for a large portion of the overall water body population but contributed marginally to the regional water surface and storage. Wide-spread small reservoirs secured the soil moisture.

The responses of surface water storage in different reservoirs have shown high spatial

heterogeneity, as a result of different water consumption pressure. Overall change trend of regional precipitation deficit determined the variation of total surface water storage in the regions. The small reservoirs and a few large reservoirs in the upstream responded instantly to the short-term variation in the regional precipitation deficit in the dry season. Larger reservoir at the outlets of the regions undertake overlaid water extraction both from the nearby towns and remote settlements and showed accelerated decrease in surface water storage.

4.5.2 Outlook

The study derived the variation of surface water storage for four representative regions on annual frequency due to the limitation of data availability. In the future, incorporating high resolution data from SAR sensor e.g. Sentinel-1 constellations could yield inter annual or seasonal surface water storage for the region. For delineation of water surface in vegetated reservoirs over wide spread regions and along time series, the method developed by Zhang et al., (2018) can be used. In addition, US-French SMOT (to be launched in 2020) will provide both water surface and levels for rivers of 100 m wide and open water bodies of size 250×250 m (Lettenmaier et al., 2015). With those data sets the surface storage in the representative regional can also be derived along time.

5. Conclusions and outlooks

5.1 Conclusions

- Single-pass TanDEM-X data can yield DEMs of resolution 10 m and accuracy of 1 m (both absolute and relative). If derived from of TanDEM-X data acquired from low water, such DEMs can represent reservoirs bathymetry with high credibility.
- In the respect of texture index GLCM variance, different types of scattering in the vegetated reservoirs cluster with distinct statistical characteristics which can be derived based on their spatial independence. The spatial abundance of the sub-populations dominated by different types of backscattering can be derived by linearly unmixing the GLCM variance of the SAR texture images without any input training data.
- The uniform threshold determined based on the sub-populations dominated by each type of backscattering can effectively delineate the water surface beneath canopy. The accuracies of such derived effective water surfaces are 77%-95%. This method can delineate the effective inundation independent of training data for time series data and show high transferability to other study areas or mapping time.
- For the 2 105 reservoirs in four regions of total area of 10 000 km^2 the bathymetry and storage capacity were derived. The spatio-temporal distribution of surface water storage was revealed for the four representative regions on annual frequency from 2009 to 2017. The surface water storage in the four regions decreased in a rate of 10^5 m^3/year from 2009 to 2015 and increased slightly from 2016 to 2017 the water storage. The year 2015 was the driest year in the last eight years for NE Brazil. It is the first time the surface water storage has been established on spatio-temporal scale. The data derived in the study can effective support the regional water management and hydrological modeling/validation for the mapped regions.

5.2 Outlook

5.2.1 Toward mapping water surface beneath canopy independent of training data

The wet soil caused by precipitation is the vital factor that affects the water surface derived in chapter 3. Therefore, in further investigation is necessary in this respect to mitigate the effect of wet soil. Among all the possible approaches, considering the multiple temporal effect of the bare soil would be one option. As rainfalls only take place randomly, surface wetness of the bare soil would decrease in a few days, particularly in region of high evapotranspiration like NE Brazil and become unable to produce high backscattering in next visit of the same SAR sensors. For the future mapping of water surface in this case Sentinel-1 data is a strong candidate.

5.2.2 Future missions and deriving surface water storage in an extended time span

In chapter 4, I adopted the time series of RapidEye images to delineate the water surface, instead of other operationally available data such as Landsat and Sentinel-1 data. This is because of the following reasons: 1) Despite its global coverage, high resolution, and long mapping history, Landsat archive cannot ensure complete annual or monthly water surface on the regional scale due to the long revisit time (Table 1.1). Inspections on the monthly water mask provided by Pekel et al. (2016) showed that there were always some water area not mapped due to clouds/haze impediment, even in the dry season. 2) Sentinel-1 data archive covers the region only 2015-present, and the period of 2015-2017 coincides with the deep drought in the region, as shown in chapter 4. However, future water surfaces consisting of the open water and the water surface beneath the vegetation can be delineated from Sentinel-1 data set on 12 days frequency. Such derived water surface areas can potentially be used to extract the surface water storage in the four regions on sub-monthly or seasonal frequency. Alternatively, the US French Surface Water Ocean Topography (SWOT) (launch planned in 2020) will provide a very good opportunity for monitoring surface water storage of high resolution. This mission aims to provide the terrestrial water storage in global scale on

sub-monthly, seasonal, and annual time scales (Rodríguez, 2016). This mission will derive both water level and water surface for rivers wider than 100 m and lakes of area larger than 250 m^2 using a Ku-band radar instrument (Rodríguez, 2016). The dynamic surface water storage on the regional scale will be characterized on real time scale.

References

Adams, J.B., Sabol, D.E., Kapos, V., Filho, R.A., Roberts, D., Smith, M.O., Gillespie, A.R., 1995. Classification of Multispectral Images Based on Fractions and Endmembers: Applications to Land-Cover Change in the Brazilian Amazon. Remote Sens. Environ.

AghaKouchak, A., Farahmand, A., Melton, F.S., Teixeira, J., Anderson, M.C., Wardlow, B.D., Hain, C.R., 2015. Remote sensing of drought: Progress, challenges and opportunities. Rev. Geophys. 53, 1–29. https://doi.org/10.1002/2014RG000456.Received

Agostinho, A.A., Gomes, L.C., Santos, N.C.L., Ortega, J.C.G., Pelicice, F.M., 2015. Fish assemblages in Neotropical reservoirs: Colonization patterns, impacts and management. Fish. Res. https://doi.org/http://dx.doi.org/10.1016/j.fishres.2015.04.006

Ahamed, A., Bolten, J.D., 2017. A MODIS-based automated flood monitoring system for southeast asia. Int. J. Appl. Earth Obs. Geoinf. 61, 104–117. https://doi.org/10.1016/j.jag.2017.05.006

Alpers, W., Hennings, I., 1984. A theory of the imaging mechanism of underwater bottom topography by real and synthetic aperture radar. J. Geophys. Res. Ocean. 89, 10529–10546. https://doi.org/10.1029/JC089iC06p10529

Alsdorf, D., Melack, J., Dunne, T., Mertes, L., Hess, L., Smith, L., 2000. Interferometric radar measurements of water level changes on the Amazon flood plain. Nature 404, 174–7. https://doi.org/10.1038/35004560

Alsdorf, D.E., Lettenmaier, D.P., 2003. Tracking fresh water from space. Science (80-.). 301, 1491–1494. https://doi.org/10.1126/science.1089802

Alsdorf, D.E., Rodriguez, E., Lettenmaier, D.P., 2007. Measuring surface water from space. Rev. Geophys. 45, 1–24. https://doi.org/10.1029/2006RG000197.1.INTRODUCTION

Alsdorf, D.E., Rodriguez, E., Lettenmaier, D.P., Rodrı´guez, E., Lettenmaier, D.P., Rodríguez, E., Lettenmaier, D.P., 2007. Measuring surface water from space. Rev. Geophys. 45, 1–24. https://doi.org/10.1029/2006RG000197

Amitrano, D., Martino, G. Di, Iodice, A., Ruello, G., Ciervo, F., Papa, M.N., 2014a. Effectiveness of high-resolution SAR for water resource management in low- income semi-arid countries. Int. J. Remote Sens. 35, 70–88. https://doi.org/10.1080/01431161.2013.862605

Amitrano, D., Martino, G., Iodice, A., Mitidieri, F., Papa, M., Riccio, D., Ruello, G., 2014b. Sentinel-1 for Monitoring Reservoirs: A Performance Analysis. Remote Sens. 6, 10676–10693. https://doi.org/10.3390/rs61110676

Arsen, A., Crétaux, J.F., Berge-Nguyen, M., del Rio, R.A., 2013. Remote sensing-derived bathymetry of Lake Poopó. Remote Sens. 6, 407–420. https://doi.org/10.3390/rs6010407

Asner, G.P., Heidebrecht, K.B., 2002. Spectral unmixing of vegetation, soil and dry carbon cover in arid regions: Comparing multispectral and hyperspectral observations. Int. J. Remote Sens. 23, 3939–3958. https://doi.org/10.1080/01431160110115960

Avisse, N., Tilmant, A., Müller, M.F., Zhang, H., 2017. Monitoring small reservoirs storage from satellite remote sensing in inaccessible areas. Hydrol. Earth Syst. Sci. 1–23.

https://doi.org/10.5194/hess-2017-373

Ayana, E.K., Philpot, W.D., Melesse, A.M., Steenhuis, T.S., 2015. Assessing the potential of MODIS/Terra version 5 images to improve near shore lake bathymetric surveys. Int. J. Appl. Earth Obs. Geoinf. 36, 13–21. https://doi.org/10.1016/j.jag.2014.10.016

Bamler, R., Hartl, P., 1998. Synthetic aperture radar interferometry. Inverse Probl. 1, 0–54. https://doi.org/10.1088/0266-5611/14/4/001

Ban, Y., Jacob, A., Gamba, P., 2014. Spaceborne SAR data for global urban mapping at 30m resolution using a robust urban extractor. ISPRS J. Photogramm. Remote Sens. 103, 28–37. https://doi.org/10.1016/j.isprsjprs.2014.08.004

Barros Grace, V., Mas-Pla, J., Oliveira Novais, T., Sacchi, E., Zuppi, G.M., 2008. Hydrological mixing and geochemical processes characterization in an estuarine/mangrove system using environmental tracers in Babitonga Bay (Santa Catarina, Brazil). Cont. Shelf Res. 28, 682–695. https://doi.org/https://doi.org/10.1016/j.csr.2007.12.006

Bastviken, D., Tranvik, L.J., Downing, J.A., Crill, P.M., Enrich-Prast, A., 2011. Freshwater methane emissions offset the continental carbon sink. Science (80-.). 331, 50. https://doi.org/10.1126/science.1196808

Bazi, Y., Bruzzone, L., Melgani, F., 2005. An unsupervised approach based on the generalized Gaussian model to automatic change detection in multitemporal SAR images. IEEE Trans. Geosci. Remote Sens. 43, 874–886. https://doi.org/10.1109/TGRS.2004.842441

Becker, J.J., Sandwell, D.T., Smith, W.H.F., Braud, J., Binder, B., Depner, J., Fabre, D., Factor, J., Ingalls, S., Kim, S.-H., Ladner, R., Marks, K., Nelson, S., Pharaoh, A., Trimmer, R., Von Rosenberg, J., Wallace, G., Weatherall, P., 2009. Global bathymetry and elevation at 30 arc seconds resolution: SRTM30_PLUS. Mar. Geod. 32, 355–371. https://doi.org/10.1080/01490410903297766

Bell, P.S., 1999. Shallow water bathymetry derived from an analysis of X-band marine radar images of waves. Coast. Eng. 37, 513–527. https://doi.org/10.1016/S0378-3839(99)00041-1

Bian, J., Li, A., Zhang, Z., Zhao, W., Lei, G., Yin, G., Jin, H., Tan, J., Huang, C., 2017. Monitoring fractional green vegetation cover dynamics over a seasonally inundated alpine wetland using dense time series HJ-1A/B constellation images and an adaptive endmember selection LSMM model. Remote Sens. Environ. 197, 98–114. https://doi.org/https://doi.org/10.1016/j.rse.2017.05.031

Biemans, H., Haddeland, I., Kabat, P., Ludwig, F., Hutjes, R.W.A., Heinke, J., Von Bloh, W., Gerten, D., 2011. Impact of reservoirs on river discharge and irrigation water supply during the 20th century. Water Resour. Res. 47, 1–15. https://doi.org/10.1029/2009WR008929

Birkett, C.M., 2000. Synergistic remote sensing of Lake Chad: Variability of basin inundation. Remote Sens. Environ. 72, 218–236. https://doi.org/10.1016/S0034-4257(99)00105-4

Birkett, C.M., 1998. Contribution of the TOPEX NASA radar altimeter to the global monitoring of large rivers and wetlands 34, 1223–1239.

Birkett, C.M., 1994. Radar altimetry: A new concept in monitoring lake level changes. Eos, Trans. Am. Geophys. Union 75, 273. https://doi.org/10.1029/94EO00944

Birkett, C.M., Mertes, L.A.K., Dunne, T., Costa, M.H., Jasinski, M.J., 2002. Surface water dynamics in the Amazon Basin: Application of satellite radar altimetry. J. Geophys. Res. Atmos. 107. https://doi.org/10.1029/2001JD000609

Bourgeau-Chavez, L.L., Kasischke, E.S., Brunzell, S.M., Mudd, J.P., Smith, K.B., Frick, a. L., 2001. Analysis of space-borne SAR data for wetland mapping in Virginia riparian ecosystems. Int. J. Remote Sens. 22, 3665–3687. https://doi.org/10.1080/01431160010029174

Brando, V.E., Anstee, J.M., Wettle, M., Dekker, A.G., Phinn, S.R., Roelfsema, C., 2009. A physics based retrieval and quality assessment of bathymetry from suboptimal hyperspectral data. Remote Sens. Environ. 113, 755–770. https://doi.org/10.1016/j.rse.2008.12.003

Braun, A., Fotopoulos, G., 2007. Assessment of SRTM, ICESat, and Survey Control Monument Elevations in Canada. Photogramm. Eng. Remote Sens. 73, 1333–1342. https://doi.org/10.14358/PERS.73.12.1333

Brusch, S., Held, P., Lehner, S., Rosenthal, W., Pleskachevsky, A., 2011. Underwater bottom topography in coastal areas from TerraSAR-X data. Int. J. Remote Sens. 32, 4527–4543. https://doi.org/10.1080/01431161.2010.489063

Bullock, S.H., Mooney, H.A., Medina, E., 1995. Seasonla dry tropical forests. Cambridge University press, Cambridge.

Bwangoy, J.R.B., Hansen, M.C., Roy, D.P., Grandi, G. De, Justice, C.O., 2010a. Wetland mapping in the Congo Basin using optical and radar remotely sensed data and derived topographical indices. Remote Sens. Environ. 114, 73–86. https://doi.org/10.1016/j.rse.2009.08.004

Bwangoy, J.R.B., Hansen, M.C., Roy, D.P., Grandi, G. De, Justice, C.O., B.Bwangoy, Jean-Robert C.Hansen, M., P.Roy, D., DeGrandi, Gianfranco O.Justice, C., 2010b. Wetland mapping in the Congo Basin using optical and radar remotely sensed data. Remote Sens. Environ. 114, 73–86. https://doi.org/10.1016/j.rse.2009.08.004

Capon, S.J., 2003. Plant community responses to wetting and drying in a large arid floodplain. River Res. Appl. 19, 509–520. https://doi.org/10.1002/rra.730

Carter, 1982. Application of remote senisng to wetlands, in: Remote Sensing for REsource Management.

Češljar, G., Stević, S., 2015. Small reservoirs and their sustainable role in fires protection of forest resources. Renew. Sustain. Energy Rev. 47, 496–503. https://doi.org/10.1016/j.rser.2015.03.071

COGERH, 2018. COGERH [WWW Document]. URL https://www.cogerh.com.br/

Cohen, J., Riihimäki, H., Pulliainen, J., Lemmetyinen, J., Heilimo, J., 2016. Implications of boreal forest stand characteristics for X-band SAR flood mapping accuracy. Remote Sens. Environ. 186, 47–63. https://doi.org/10.1016/j.rse.2016.08.016

Colloff, M.J., Baldwin, D.S., 2010. Resilience of floodplain ecosystems in a semi-arid environment. Rangel. J. 32, 305–314. https://doi.org/10.1071/RJ10015

Conners, R.W., Trivedi, M.M., Harlow, C.A., 1984. Segmentation of a high-resolution urban scene using texture operators. Comput. Vision, Graph. Image Process. 25, 273–310. https://doi.org/10.1016/0734-189X(84)90197-X

Costa, B.M., Battista, T.A., Pittman, S.J., 2009. Comparative evaluation of airborne LiDAR and ship-based multibeam SoNAR bathymetry and intensity for mapping coral reef ecosystems. Remote Sens. Environ. 113, 1082–1100. https://doi.org/http://dx.doi.org/10.1016/j.rse.2009.01.015

Crosetto, M., 2002. Calibration and validation of SAR interferometry. ISPRS J. Photogramm. Remote Sens. 29, 26–29.

Curran., P.J., 1985. Principles of Remote Sensing. London: Longman GRoup Limited, London. https://doi.org/10.1080/01431168508948322

da Silva, S.J., Calmant, S., Seyler, F., Rotunno Filho, O.C., Cochonneau, G., Mansur, W.J., 2010. Water levels in the Amazon basin derived from the ERS 2 and ENVISAT radar altimetry missions. Remote Sens. Environ. 114, 2160–2181. https://doi.org/10.1016/j.rse.2010.04.020

Danklmayer, A., Doring, B.J., Schwerdt, M., Chandra, M., 2009. Assessment of Atmospheric Propagation Effects in SAR Images. IEEE Trans. Geosci. Remote Sens. 47, 3507–3518. https://doi.org/10.1109/TGRS.2009.2022271

De Loor, G.P., Loor, G. De, 1981. The observation of tidal patterns, currents, and bathymetry with SLAR imagery of the sea. IEEE J. Ocean. Eng. 6, 124–129. https://doi.org/10.1109/JOE.1981.1145501

Dekker, A.G., Phinn, S.R., Anstee, J., Bissett, P., Brando, V.E., Casey, B., Fearns, P., Hedley, J., Klonowski, W., Lee, Z.P., Lynch, M., Lyons, M., Mobley, C., Roelfsema, C., 2011. Intercomparison of shallow water bathymetry, hydro-optics, and benthos mapping techniques in Australian and Caribbean coastal environments. Limnol. Oceanogr. Methods 9, 396–425. https://doi.org/10.4319/lom.2011.9.396

Dell'Acqua, F., Gamba, P., 2003. Texture-based characterization of urban environments on satellite SAR images. IEEE Trans. Geosci. Remote Sens. https://doi.org/10.1109/TGRS.2002.807754

Dellepiane, S., Bo, G., Mom, S., Buck, C., 2000a. SAR images and interferometric coherence for flood monitoring, in: Geoscience and Remote Sensing Symposium, 2000. Proceedings. IGARSS 2000. IEEE 2000 International. Honolulu, HI, p. 2608–2610 (vol.6).

Dellepiane, S., Bo, G., Monni, S., Buck, C., 2000b. SAR images and interferometric coherence for flood monitoring. IGARSS 2000. IEEE 2000 Int. Geosci. Remote Sens. Symp. Tak. Pulse Planet Role Remote Sens. Manag. Environ. Proc. (Cat. No.00CH37120) 6, 2608–2610. https://doi.org/10.1109/IGARSS.2000.859656

Dierssen, H.M., Zimmerman, R.C., Leathers, R. a., Downes, T.V., Davis, C.O., 2003. Ocean color remote sensing of seagrass and bathymetry in the Bahamas Banks by high resolution

airborne imagery. Limnol. Oceanogr. 48, 444–455. https://doi.org/10.4319/lo.2003.48.1_part_2.0444

Dietze, E., Hartmann, K., Diekmann, B., IJmker, J., Lehmkuhl, F., Opitz, S., Stauch, G., Wünnemann, B., Borchers, A., 2012. An end-member algorithm for deciphering modern detrital processes from lake sediments of Lake Donggi Cona, NE Tibetan Plateau, China. Sediment. Geol. 243–244, 169–180. https://doi.org/10.1016/j.sedgeo.2011.09.014

Dobson, M.C., Ulaby, F.T., Pierce, L.E., Sharik, T.L., Bergen, K.M., Kellndorfer, J., Kendra, J.R., Li, E., Lin, Y.C., Nashashibi, A., Sarabandi, K., Member, S., Siqueira, P., 1995. Estimation of Forest Biophysical Characteristics in Northem Michigan with SIR-C / X-SAR. IEEE Trans. Geosci. Remote Sens. 33.

Donchyts, G., Baart, F., Winsemius, H., Gorelick, N., Kwadijk, J., van de Giesen, N., 2016. Earth's surface water change over the past 30 years. Nat. Clim. Chang. 6, 810–813. https://doi.org/10.1038/nclimate3111

Dronova, I., Gong, P., Wang, L., Zhong, L., 2015. Mapping dynamic cover types in a large seasonally flooded wetland using extended principal component analysis and object-based classification. Remote Sens. Environ. 158, 193–206. https://doi.org/10.1016/j.rse.2014.10.027

Duan, Z., Bastiaanssen, W.G.M., 2013. Estimating water volume variations in lakes and reservoirs from four operational satellite altimetry databases and satellite imagery data. Remote Sens. Environ. 134, 403–416. https://doi.org/10.1016/j.rse.2013.03.010

Duque, S., Balss, U., Rossi, C., Fritz, T., Balzer, W., 2012. TanDEM-X Payload Ground Segment: CoSSC Generation and Interferometric Considerations. Ger. Aerosp. Cent. 31.

Durden, S.L., Morrissey, L.A., Livingston, G.P., 1995. Microwave Backscatter and Attenuation Dependence on Leaf Area Index for Flooded Rice Fields. IEEE Trans. Geosci. Remote Sens. 33, 807–810. https://doi.org/10.1109/36.387599

E, D.C., Zhou, C.X., Liao, M.S., 2004. Application of SAR interferometry on DEM generation of the Grove Mountains. Photogramm. Eng. Remote Sensing 70, 1145–1149. https://doi.org/10.14358/PERS.70.10.1145

E, D.C., Zhou, C.X., Liao, M.S., 2004. Application of SAR Interferometry on DEM Generation of the Grove Mountains. Photogramm. Eng. Remote Sens. 70, 1145–1149. https://doi.org/10.14358/PERS.70.10.1145

Ehsani, N., Vörösmarty, C.J., Fekete, B.M., Stakhiv, E.Z., 2017. Reservoir operations under climate change: Storage capacity options to mitigate risk. J. Hydrol. 555, 435–446. https://doi.org/10.1016/j.jhydrol.2017.09.008

Eilander, D., Annor, F., Iannini, L., van de Giesen, N., 2014. Remotely Sensed Monitoring of Small Reservoir Dynamics: A Bayesian Approach. Remote Sens. 6, 1191–1210. https://doi.org/10.3390/rs6021191

Esch, T., Marconcini, M., Felbier, A., Roth, A., Heldens, W., Huber, M., Schwinger, M., Taubenbock, H., Muller, A., Dech, S., 2013. Urban footprint processor-Fully automated processing chain generating settlement masks from global data of the TanDEM-X mission.

IEEE Geosci. Remote Sens. Lett. 10, 1617–1621. https://doi.org/10.1109/LGRS.2013.2272953

ESRI, 2011. ArcGIS Desktop: Release 10.

Evans, T.L., Costa, M., 2013. Landcover classification of the Lower Nhecolândia subregion of the Brazilian Pantanal Wetlands using ALOS/PALSAR, RADARSAT-2 and ENVISAT/ASAR imagery. Remote Sens. Environ. 128, 118–137. https://doi.org/10.1016/j.rse.2012.09.022

Farr, T.G., Rosen, P. a., Caro, E., Crippen, R., 2007. The Shuttle Radar Topography Mission. Rev. Geophys. 1–33. https://doi.org/10.1029/2005RG000183.1.INTRODUCTION

Feng, L., Hu, C., Chen, X., Cai, X., Tian, L., Gan, W., 2012. Assessment of inundation changes of Poyang Lake using MODIS observations between 2000 and 2010. Remote Sens. Environ. 121, 80–92. https://doi.org/10.1016/j.rse.2012.01.014

Feng, L., Hu, C., Chen, X., Li, R., Tian, L., Murch, B., 2011. MODIS observations of the bottom topography and its inter-annual variability of Poyang Lake. Remote Sens. Environ. 115, 2729–2741. https://doi.org/10.1016/j.rse.2011.06.013

Feng, L., Hu, C., Chen, X., Song, Q., 2014. Influence of the Three Gorges Dam on total suspended matters in the Yangtze Estuary and its adjacent coastal waters: Observations from MODIS. Remote Sens. Environ. 140, 779–788. https://doi.org/10.1016/j.rse.2013.10.002

Ferrazzoli, P., Guerriero, L., 1995. Radar sensitivity to tree geometry and woody volume: a model analysis. IEEE Trans. Geosci. Remote Sens. 33, 360–371. https://doi.org/10.1109/36.377936

Feurer, D., Bailly, J.S., Puech, C., Le Coarer, Y., Viau, A.A., 2008. Very-high-resolution mapping of river-immersed topography by remote sensing. Prog. Phys. Geogr. 32, 403–419. https://doi.org/10.1177/0309133308096030

Fluet-Chouinard, E., Lehner, B., Rebelo, L.-M., Papa, F., Hamilton, S.K., 2015. Development of a global inundation map at high spatial resolution from topographic downscaling of coarse-scale remote sensing data. Remote Sens. Environ. 158, 348–361. https://doi.org/10.1016/j.rse.2014.10.015

Ford, J.P., Cimino, J.B., Elachi, C., 1983. Space Shuttle Columbia Views the World with Imaging Radar: The SIR-A Experiment. JPL Publ. 82–95.

Frappart, F., Seyler, F., Martinez, J.-M., León, J.G., Cazenave, A., 2005. Floodplain water storage in the Negro River basin estimated from microwave remote sensing of inundation area and water levels. Remote Sens. Environ. 99, 387–399. https://doi.org/10.1016/j.rse.2005.08.016

Fritz, T., 2012. TanDEM-X Ground Segment-TanDEM-X Experimental Product Description. Distribution 3–192.

Fritz, T., Eineder, M., 2013. TerraSAR-X Ground Segment Basic Product Specification Document. https://doi.org/10.1088/1751-8113/44/8/085201

Gala, T.S., Melesse, A.M., 2012. Monitoring prairie wet area with an integrated LANDSAT

ETM+, RADARSAT-1 SAR and ancillary data from LIDAR. Catena 95, 12–23. https://doi.org/10.1016/j.catena.2012.02.022

Gao, H., 2015. Satellite remote sensing of large lakes and reservoirs: from elevation and area to storage. Wiley Interdiscip. Rev. Water 2, 147–157. https://doi.org/10.1002/wat2.1065

Gao, H., Birkett, C., Lettenmaier, D.P., 2012. Global monitoring of large reservoir storage from satellite remote sensing. Water Resour. Res. 48, 1–12. https://doi.org/10.1029/2012WR012063

Gholizadeh, M., Melesse, A., Reddi, L., 2016. A Comprehensive Review on Water Quality Parameters Estimation Using Remote Sensing Techniques. Sensors 16, 1298. https://doi.org/10.3390/s16081298

Goblirsch, W., Pasquali, P., 1996. Algorithms for Calculation of Digital Surface Models from the Unwrapped Interferometric Phase. Proc. Int. Geosci. Remote Sens. Symp. 656–658.

Goldstein, R.M., Werner, C.L., 1998. Radar interferogram filtering for geophysical applications. Geophys. Res. Lett. 25, 4035. https://doi.org/10.1029/1998GL900033

Gonzalez-Dugo, V., Zarco-Tejada, P.J., Fereres, E., 2014. Applicability and limitations of using the crop water stress index as an indicator of water deficits in citrus orchards. Agric. For. Meteorol. 198–199, 94–104. https://doi.org/10.1016/j.agrformet.2014.08.003

González, J., Bachmann, M., 2010. Development of the TanDEM-X calibration concept: analysis of systematic errors. IEEE Trans. Geosci. Remote Sens. Remote Sens. 48, 716–726.

Gorelick, N., Hancher, M., Dixon, M., Ilyushchenko, S., Thau, D., Moore, R., 2017. Google Earth Engine: Planetary-scale geospatial analysis for everyone. Remote Sens. Environ. 202, 18–27. https://doi.org/https://doi.org/10.1016/j.rse.2017.06.031

Gruber, A., Wessel, B., Huber, M., Roth, A., 2012. Operational TanDEM-X DEM calibration and first validation results. ISPRS J. Photogramm. Remote Sens. 73, 39–49. https://doi.org/10.1016/j.isprsjprs.2012.06.002

Gstaiger, V., Huth, J., Gebhardt, S., Wehrmann, T., Kuenzer, C., 2012. Multi-sensoral and automated derivation of inundated areas using TerraSAR-X and ENVISAT ASAR data. Int. J. Remote Sens. 33, 7291–7304. https://doi.org/10.1080/01431161.2012.700421

Guenther, G.C., Cunningham, a G., Larocque, P.E., Reid, D.J., Service, N.O., Highway, E., Spring, S., 2000. Meeting the Accuracy Challenge in Airborne Lidar Bathymetry. EARSeL eProceedings 1, 1–27.

Gunnison, D., 1985. Microbial Processes in Reservoirs. Boston, Lancaster.

Hagensieker, R., Roscher, R., Rosentreter, J., Jakimow, B., Waske, B., 2017. Tropical land use land cover mapping in Pará (Brazil) using discriminative Markov random fields and multi-temporal TerraSAR-X data. Int. J. Appl. Earth Obs. Geoinf. 63, 244–256. https://doi.org/https://doi.org/10.1016/j.jag.2017.07.019

Hall, A.C., Schumann, G.J.-P., Bamber, J.L., Bates, P.D., 2011. Tracking water level changes of the Amazon Basin with space-borne remote sensing and integration with large scale hydrodynamic modelling: A review. Phys. Chem. Earth, Parts A/B/C 36, 223–231.

https://doi.org/10.1016/j.pce.2010.12.010

Haralick, R., Dinstein, I., Shanmugam, K., 1973. Textural features for image classification.

Heine, I., Francke, T., Rogass, C., Medeiros, P.H.A., Bronstert, A., Foerster, S., 2014. Monitoring Seasonal Changes in the Water Surface Areas of Reservoirs Using TerraSAR-X Time Series Data in Semiarid Northeastern Brazil. IEEE J. Sel. Top. Appl. EARTH Obs. Remote Sens. 7, 3190–3199.

Henry, J.B.B., Chastanet, P., Fellah, K., Desnos, Y.-. L., 2006. Envisat multi-polarized ASAR data for flood mapping. Int. J. Remote Sens. 27, 1921–1929. https://doi.org/10.1080/01431160500486724

Hess, L.L., Melack, J.M., Simonett, D.S., 1990. Radar detection of flooding beneath the forest canopy : a review. Int. J. Remote Sens. 11, 1313–1325. https://doi.org/10.1080/01431169008955095

Hess, L.L., Melacka, J.M., Novob, E.M.L.M., Barbosac, C.C.F., Gasti, M., 2003. Dual-season mapping of wetland inundation and vegetation for the central Amazon basin. Remote Sens. Environ. 87, 404–428. https://doi.org/10.1016/j.rse.2003.04.001

Hess, L.L.L.L., Melack, J.M.J.M., Filoso, S., Wang，Yong, Wang, Y.W.Y., 1995. Delineation of Inundated Area and Vegetation Along the Amazon Floodplain with the SIR-C Synthetic Aperture Radar. IEEE transections gescience Remote snesing 33, 896–904. https://doi.org/10.1109/36.406675

Hoffer, R.M., 1978. Biological and Physical considerations in Applying Computer-aided analysis techniques to Remote sensor data approach, in: In Remote Sensing: The Quantitative Approach,. avis Mc Graw-Hill.; U.S.A.

Horritt, M.S., Mason, D.C., Cobby, D.M., Davenport, I.J., Bates, P.D., 2003. Waterline mapping in flooded vegetation from airborne SAR imagery. Remote Sens. Environ. 85, 271–281. https://doi.org/10.1016/S0034-4257(03)00006-3

Horritt, M.S., Mason, D.C., Luckman, A.J., 2001. Flood boundary delineation from Synthetic Aperture Radar imagery using a statistical active contour model. Int. J. Remote Sens. 22, 2489–2507. https://doi.org/10.1080/01431160116902

Hostache, R., Matgen, P., Wagner, W., 2012. Change detection approaches for flood extent mapping: How to select the most adequate reference image from online archives? Int. J. Appl. Earth Obs. Geoinf. 19, 205–213. https://doi.org/10.1016/j.jag.2012.05.003

Huang, Peng, Y., Lang, M., Yeo, I.-Y., McCarty, G., 2014. Wetland inundation mapping and change monitoring using Landsat and airborne LiDAR data. Remote Sens. Environ. 141, 231–242. https://doi.org/10.1016/j.rse.2013.10.020

Huber, M., Wessel, B., Kosmann, D., Felbier, A., Schwieger, V., Habermeyer, M., Wendleder, A., Roth, A., 2009. Ensuring globally the TanDEM-X height accuracy: Analysis of the reference data sets ICESat, SRTM and KGPS-tracks, in: EEE International Geoscience and Remote Sensing Symposium,2009. https://doi.org/10.1109/IGARSS.2009.5418204

Humphrey, V., Gudmundsson, L., Seneviratne, S.I., 2017. A global reconstruction of climate-driven subdecadal water storage variability. Geophys. Res. Lett. 44, 2300–2309.

https://doi.org/10.1002/2017GL072564

IBGE, 2015. Instituto Brasileiro de Geografia e Estatística [WWW Document]. URL http://www.ibge.gov.br/english/

Immerzeel, W.W., Droogers, P., de Jong, S.M., Bierkens, M.F.P., 2009. Large-scale monitoring of snow cover and runoff simulation in Himalayan river basins using remote sensing. Remote Sens. Environ. 113, 40–49. https://doi.org/10.1016/j.rse.2008.08.010

Infoterra an EADS Astrium company, 2008. Radiometric Calibration of TerraSAR-X Data, Beta Naught and Sigma Naught Coefficient Calculation. TerraSAR-X Serv. 1–16.

INMET, 2018. Climatology standards of Brazil [WWW Document]. URL http://www.inmet.gov.br/portal/index.php?r=home/page&page=imprensa_analises_semanais

Jain, S.K., Saraf, A.K., Goswami, A., Ahmad, T., 2006. Flood inundation mapping using NOAA AVHRR data. Water Resour. Manag. 20, 949–959. https://doi.org/10.1007/s11269-006-9016-4

James, A.L., Roulet, N.T., 2006. Investigating the applicability of end-member mixing analysis (EMMA) across scale: A study of eight small, nested catchments in a temperate forested watershed. Water Resour. Res. 42, 1–17. https://doi.org/10.1029/2005WR004419

Jay, S., Guillaume, M., 2014. A novel maximum likelihood based method for mapping depth and water quality from hyperspectral remote-sensing data. Remote Sens. Environ. 147, 121–132. https://doi.org/10.1016/j.rse.2014.01.026

Jiang, L., Nielsen, K., Andersen, O.B., Bauer-Gottwein, P., 2017. CryoSat-2 radar altimetry for monitoring freshwater resources of China. Remote Sens. Environ. 200, 125–139. https://doi.org/10.1016/j.rse.2017.08.015

Jin, H., Huang, C., Lang, M.W., Yeo, I.-Y., Stehman, S. V., 2017. Monitoring of wetland inundation dynamics in the Delmarva Peninsula using Landsat time-series imagery from 1985 to 2011. Remote Sens. Environ. 190, 26–41. https://doi.org/10.1016/j.rse.2016.12.001

Karila, K., Vastaranta, M., Karjalainen, M., Kaasalainen, S., 2015. Tandem-X interferometry in the prediction of forest inventory attributes in managed boreal forests. Remote Sens. Environ. 159, 259–268. https://doi.org/10.1016/j.rse.2014.12.012

Kasischke, E.S., Bourgeau-Chavez, L.L., Rober, A.R., Wyatt, K.H., Waddington, J.M., Turetsky, M.R., 2009. Effects of soil moisture and water depth on ERS SAR backscatter measurements from an Alaskan wetland complex. Remote Sens. Environ. 113, 1868–1873. https://doi.org/10.1016/j.rse.2009.04.006

Kasischke, E.S., Smith, K.B., Bourgeau-Chavez, L.L., Romanowicz, E. a., Brunzell, S., Richardson, C.J., 2003. Effects of seasonal hydrologic patterns in south Florida wetlands on radar backscatter measured from ERS-2 SAR imagery. Remote Sens. Environ. 88, 423–441. https://doi.org/10.1016/j.rse.2003.08.016

Kim, J.-W., Lu, Z., Jones, J.W., Shum, C.K., Lee, H., Jia, Y., 2014. Monitoring Everglades freshwater marsh water level using L-band synthetic aperture radar backscatter. Remote

Sens. Environ. 150, 66–81. https://doi.org/10.1016/j.rse.2014.03.031

Kim, J.-W., Lu, Z., Lee, H., Shum, C.K., Swarzenski, C.M., Doyle, T.W., Baek, S.-H., 2009. Integrated analysis of PALSAR/Radarsat-1 InSAR and ENVISAT altimeter data for mapping of absolute water level changes in Louisiana wetlands. Remote Sens. Environ. 113, 2356–2365. https://doi.org/10.1016/j.rse.2009.06.014

Kim, J.W., Lu, Z., Gutenberg, L., Zhu, Z., 2017. Characterizing hydrologic changes of the Great Dismal Swamp using SAR/InSAR. Remote Sens. Environ. 198, 187–202. https://doi.org/10.1016/j.rse.2017.06.009

Kittler, J., Illingworth, J., 1986. Minimum error thresholding. Pattern Recognit. 19, 41–47. https://doi.org/10.1016/0031-3203(86)90030-0

Klemenjak, S., Waske, B., Valero, S., Chanussot, J., 2012. Automatic Detection of Rivers in High-Resolution SAR Data. IEEE J. Sel. Top. Appl. Earth Obs. Remote Sens. 5, 1364–1372. https://doi.org/10.1109/JSTARS.2012.2189099

Koblinsky, C.J., Clarke, R.T., Brenner, A.C., Frey, H., 1993. Measurement of river level variations with satellite altimetry. Water Resour. Res. 29, 1839–1848. https://doi.org/10.1029/93WR00542

Koltun, G.F., 2001. Hydrologic Considerations for Estimation of Storage-Capacity Requirements of Impounding and Side-Channel Reservoirs Used for Water Supply in Ohio. Columbus, Ohio.

Krieger, G., Moreira, A., Fiedler, H., Hajnsek, I., Werner, M., Younis, M., Zink, M., 2007. TanDEM-X : A Satellite Formation for High-Resolution SAr Interferometry. IEEE Trans. Geosci. Remote Sens. 45, 3317–3341. https://doi.org/10.1109/TGRS.2007.900693

Krohn, M.D., Milton, N.M., Segal, B., 1983. SEASAT synthetic aperture radar (SAR) response to lowland vegetation types in eastern Maryland and Virginia. J. Geodyn. 88, 1937–1952.

Kubanek, J., Westerhaus, M., Schenk, A., Aisyah, N., Brotopuspito, K.S., Heck, B., 2015. Volumetric change quantification of the 2010 Merapi eruption using TanDEM-X InSAR. Remote Sens. Environ. 164, 16–25. https://doi.org/10.1016/j.rse.2015.02.027

Lafon, V., Froidefond, J.M., Lahet, F., Castaing, P., 2002. SPOT shallow water bathymetry of a moderately turbid tidal inlet based on field measurements. Remote Sens. Environ. 81, 136–148. https://doi.org/http://dx.doi.org/10.1016/S0034-4257(01)00340-6

Lang, M.W., Kasischke, E.S., 2008. Using C-band synthetic aperture radar data to monitor forested wetland hydrology in Maryland's coastal plain, USA. IEEE Trans. Geosci. Remote Sens. 46, 535–546. https://doi.org/10.1109/TGRS.2007.909950

Lang, M.W., McCarty, G.W., 2009. Lidar intensity for improved detection of inundation below the forest canopy. Wetlands 29, 1166–1178. https://doi.org/10.1672/08-197.1

Lang, M.W., Townsend, P. a., Kasischke, E.S., 2008. Influence of incidence angle on detecting flooded forests using C-HH synthetic aperture radar data. Remote Sens. Environ. 112, 3898–3907. https://doi.org/10.1016/j.rse.2008.06.013

Lawson, C.L., Hanson., R., 1974. Solving least squares problems. Prentice Hall, Englewood Cliffs, New Jersey.

Lee, H., Yuan, T., Jung, H.C., Beighley, E., 2015. Mapping wetland water depths over the central Congo Basin using PALSAR ScanSAR, Envisat altimetry, and MODIS VCF data. Remote Sens. Environ. 159, 70–79. https://doi.org/10.1016/j.rse.2014.11.030

Lee, J.S., 1980. Digital image enhancement and noise filtering by use of local statistics. IEEE Trans. Pattern Anal. Mach. Intell. 2, 165–168. https://doi.org/10.1109/TPAMI.1980.4766994

Lee, Y.K., Park, J.W., Choi, J.K., Oh, Y., Won, J.S., 2012. Potential uses of TerraSAR-X for mapping herbaceous halophytes over salt marsh and tidal flats. Estuar. Coast. Shelf Sci. 115, 366–376. https://doi.org/10.1016/j.ecss.2012.10.003

Lee, Z., Carder, K.L., Mobley, C.D., Steward, R.G., Patch, J.S., 1999. Hyperspectral remote sensing for shallow waters: 2. Deriving bottom depths and water properties by optimization. Appl. Opt. 38, 3831–3843. https://doi.org/10.1364/AO.38.003831

Lee, Z., Carder, K.L., Mobley, C.D., Steward, R.G., Patch, J.S., 1998. Hyperspectral remote sensing for shallow waters. I. A semianalytical model. Appl. Opt. 37, 6329–6338. https://doi.org/10.1364/AO.37.006329

Lee, Z., Casey, B., Arnone, R., Weidemann, A., Parsons, R., Montes, M.J., Gao, B.-C., Goode, W., Davis, C., Dye, J., 2007. Water and bottom properties of a coastal environment derived from Hyperion data measured from the EO-1 spacecraft platform. J. Appl. Remote Sens. 1, 011502. https://doi.org/10.1117/1.2822610

Legleiter, C.J., Roberts, D.A., 2005. Effects of channel morphology and sensor spatial resolution on image-derived depth estimates. Remote Sens. Environ. 95, 231–247. https://doi.org/10.1016/j.rse.2004.12.013

Lettenmaier, D.P., Alsdorf, D., Dozier, J., Huffman, G.J., Pan, M., Wood, E.F., 2015. Inroads of remote sensing into hydrologic science during the WRR era. Water Resour. Res. 51, 7309–7342. https://doi.org/10.1002/2015WR017616.Received

Li, L., Chen, Y., Xu, T., Liu, R., Shi, K., Huang, C., 2015a. Super-resolution mapping of wetland inundation from remote sensing imagery based on integration of back-propagation neural network and genetic algorithm. Remote Sens. Environ. 164, 142–154. https://doi.org/10.1016/j.rse.2015.04.009

Li, L., Chen, Y., Yu, X., Liu, R., Huang, C., 2015b. Sub-pixel flood inundation mapping from multispectral remotely sensed images based on discrete particle swarm optimization. ISPRS J. Photogramm. Remote Sens. 101, 10–21. https://doi.org/10.1016/j.isprsjprs.2014.11.006

Li, N., Wang, R., Liu, Y., Du, K., Chen, J., Deng, Y., 2014. Robust river boundaries extraction of dammed lakes in mountain areas after Wenchuan Earthquake from high resolution SAR images combining local connectivity and ACM. ISPRS J. Photogramm. Remote Sens. 94, 91–101. https://doi.org/10.1016/j.isprsjprs.2014.04.020

Lillesand, T.M., Kiefer, R.W., Chipman, J.W., 2008. Remote Sensing and Image Interpretation, 6th ed.

Lima Neto, I.E., Wiegand, M.C., de Araújo, J.C., 2011. Sediment redistribution due to a dense

reservoir network in a large semi-arid Brazilian basin. Hydrol. Sci. J. 56, 319–333. https://doi.org/10.1080/02626667.2011.553616

Lucas, R.M., Mitchell, A.L., Rosenqvist, A.K.E., 2007. The potential of L-band SAR for quantifying mangrove characteristics and change : case studies from the tropics. Aquat. Conserv Mar. Freshw. Ecosyst 264, 245–264. https://doi.org/10.1002/aqc

Lyzenga, D.R., 1985. Shallow-water bathymetry using combined lidar and passive multispectral scanner data. Int. J. Remote Sens. 6, 115–125. https://doi.org/10.1080/01431168508948428

Lyzenga, Da.R., 1978. Passive remote sensing techniques for mapping water depth and bottom features. Appl. Opt. 17, 379–383.

M.Kampes, B., 2006. Radar Inteferometry, in: Remote Sensing and Digital Image Processing. p. 17.

Maillard, P., Bercher, N., Calmant, S., 2015. New processing approaches on the retrieval of water levels in Envisat and SARAL radar altimetry over rivers: A case study of the São Francisco River, Brazil. Remote Sens. Environ. 156, 226–241. https://doi.org/http://dx.doi.org/10.1016/j.rse.2014.09.027

Maritorena, S., Morel, A., Gentili, B., 1994. Diffuse reflectance of oceanic shallow waters: Influence of water depth and bottom albedo. Limnol. Oceanogr. 39, 1689–1703. https://doi.org/10.4319/lo.1994.39.7.1689

Marti-Cardona, B., Dolz-Ripolles, J., Lopez-Martinez, C., 2013. Wetland inundation monitoring by the synergistic use of ENVISAT/ASAR imagery and ancilliary spatial data. Remote Sens. Environ. 139, 171–184. https://doi.org/10.1016/j.rse.2013.07.028

Marti-Cardona, B., Lopez-Martinez, C., Dolz-Ripolles, J., Bladè-Castellet, E., 2010. ASAR polarimetric, multi-incidence angle and multitemporal characterization of Doñana wetlands for flood extent monitoring. Remote Sens. Environ. 114, 2802–2815. https://doi.org/10.1016/j.rse.2010.06.015

Martinis, S., Kersten, J., Twele, A., 2015a. A fully automated TerraSAR-X based flood service. ISPRS J. Photogramm. Remote Sens. 104, 203–212. https://doi.org/10.1016/j.isprsjprs.2014.07.014

Martinis, S., Kuenzer, C., Wendleder, A., Huth, J., Twele, A., Roth, A., Dech, S., 2015b. Comparing four operational SAR-based water and flood detection approaches. Int. J. Remote Sens. 36, 3519–3543. https://doi.org/10.1080/01431161.2015.1060647

Martone, M., Bräutigam, B., Rizzoli, P., Gonzalez, C., Bachmann, M., Krieger, G., 2012. Coherence evaluation of TanDEM-X interferometric data. ISPRS J. Photogramm. Remote Sens. 73, 21–29. https://doi.org/10.1016/j.isprsjprs.2012.06.006

Marzano, F.S., Mori, S., Chini, M., Pulvirenti, L., Pierdicca, N., Montopoli, M., Weinman, J.A., 2011. Potential of high-resolution detection and retrieval of precipitation fields from X-band spaceborne synthetic aperture radar over land. Hydrol. Earth Syst. Sci. 15, 859–875. https://doi.org/10.5194/hess-15-859-2011

Mason, D.C., Trigg, M., Garcia-Pintado, J., Cloke, H.L., Neal, J.C., Bates, P.D., 2016.

Improving the TanDEM-X Digital Elevation Model for flood modelling using flood extents from Synthetic Aperture Radar images. Remote Sens. Environ. 173, 15–28. https://doi.org/10.1016/j.rse.2015.11.018

McFeeter, S.K., 1996. The use of the Normalized Difference Water Index (NDWI) in the delineation of open water features. Int. J. Remote Sens. 17, 1425–1432. https://doi.org/10.1080/01431169608948714

Medina, C.E., Gomez-Enri, J., Alonso, J.J., Villares, P., 2008. Water level fluctuations derived from ENVISAT Radar Altimeter (RA-2) and in-situ measurements in a subtropical waterbody: Lake Izabal (Guatemala). Remote Sens. Environ. 112, 3604–3617. https://doi.org/10.1016/j.rse.2008.05.001

Melo, D.D.C.D., Scanlon, B.R., Zhang, Z., Wendland, E., Yin, L., 2016. Reservoir storage and hydrologic responses to droughts in the Paraná River basin, south-eastern Brazil. Hydrol. Earth Syst. Sci. 20, 4673–4688. https://doi.org/10.5194/hess-20-4673-2016

Melrose, R.T., Kingsford, R.T., Milne, a. K., 2012. Using radar to detect flooding in arid wetlands and rivers. Int. Geosci. Remote Sens. Symp. 5242–5245. https://doi.org/10.1109/IGARSS.2012.6352427

Messager, M.L., Lehner, B., Grill, G., Nedeva, I., Schmitt, O., 2016. Estimating the volume and age of water stored in global lakes using a geo-statistical approach. Nat. Commun. 7, 1–11. https://doi.org/10.1038/ncomms13603

Michailovsky, C.I., Bauer-Gottwein, P., 2014. Operational reservoir inflow forecasting with radar altimetry: the Zambezi case study. Hydrol. Earth Syst. Sci. 18, 997–1007. https://doi.org/10.5194/hess-18-997-2014

Mohammadi, A., Costelloe, J.F., Ryu, D., 2017. Application of time series of remotely sensed normalized difference water, vegetation and moisture indices in characterizing flood dynamics of large-scale arid zone floodplains. Remote Sens. Environ. 190, 70–82. https://doi.org/10.1016/j.rse.2016.12.003

Moreira, A., Krieger, G., Hajnsek, I., Hounam, D., Werner, M., Riegger, S., Settelmeyer, E., 2004. TanDEM-X : A TerraSAR-X Add-On Satellite for Single-Pass SAR Interferometry, in: Geoscience and Remote Sensing Symposium, 2004. IGARSS '04. Proceedings. 2004 IEEE International. IEEE, pp. 1000–1003. https://doi.org/10.1109/IGARSS.2004.1368578

Moreira, A., Krieger, G., Hajnsek, I., Hounam, D., Werner, M., Riegger, S., Settelmeyer, E., 2004. TanDEM-X: a TerraSAR-X add-on satellite for single-pass SAR interferometry. IGARSS 2004. 2004 IEEE Int. Geosci. Remote Sens. Symp. 2, 2–5. https://doi.org/10.1109/IGARSS.2004.1368578

Morris, C.S., Gill, K., Navy, U.S., 1994. Variation of Great Lakes water levels derived from Geosat altimetry A technique for using satellite radar altimetry data to estimate the temporal Great Lakes data from the first 2 years Exact Repeat Mission. Water Resour. Res. 30, 1009–1017.

Mouw, C.B., Greb, S., Aurin, D., DiGiacomo, P.M., Lee, Z., Twardowski, M., Binding, C., Hu, C., Ma, R., Moore, T., Moses, W., Craig, S.E., 2015. Aquatic color radiometry remote

sensing of coastal and inland waters: Challenges and recommendations for future satellite missions. Remote Sens. Environ. 160, 15–30. https://doi.org/http://dx.doi.org/10.1016/j.rse.2015.02.001

Munyaneza, O., Wali, U.G., Uhlenbrook, S., Maskey, S., Mlotha, M.J., 2009. Water level monitoring using radar remote sensing data: Application to Lake Kivu, central Africa. Phys. Chem. Earth, Parts A/B/C 34, 722–728. https://doi.org/10.1016/j.pce.2009.06.008

Nico, G., Pappalepore, M., Pasquariello, G., Refice, a., Samarelli, S., 2000. Comparison of SAR amplitude vs. coherence flood detection methods - a GIS application. Int. J. Remote Sens. 21, 1619–1631. https://doi.org/10.1080/014311600209931

Novo, E.M.L.D.M., Costa, M.P.D.F.D.F., Mantovani, J.E., De Moraes Novo, E.M.L., Costa, M.P.D.F.D.F., Mantovani, J.E., 1998. RADARSAT Exploratory Survey on Macrophyte Biophysical Parameters in Tropical Reservoirs. Can. J. Remote Sens. 24, 367–375. https://doi.org/10.1080/07038992.1998.10874701

Nyoungui, A.N., Tonye, E., Akono, A., 2002. Evaluation of speckle filtering and texture analysis methods for land cover classification from SAR images. Int. J. Remote Sens. 23, 1895–1925. https://doi.org/10.1080/01431160110036157

O'Grady, D., Leblanc, M., 2014. Radar mapping of broad-scale inundation: Challenges and opportunities in Australia. Stoch. Environ. Res. Risk Assess. 28, 29–38. https://doi.org/10.1007/s00477-013-0712-3

Ormsby, J.P., Blanchard, B.J., Blanchard, A.J., 1985. Detection of lowland flooding using active microwave systems. Photogramm. Eng. Remote Sensing 51, 317–328.

Otsu, N., 1979. A Threshold Selection Method from Gray-Level Histograms. IEEE Trans. Syst. Man. Cybern. 9, 62–66. https://doi.org/10.1109/TSMC.1979.4310076

Ouma, Y.O., Tateishi, R., 2006. A water index for rapid mapping of shoreline changes of five East African Rift Valley lakes: an empirical analysis using Landsat TM and ETM+ data. Int. J. Remote Sens. 27, 3153–3181. https://doi.org/10.1080/01431160500309934

Pacheco, A., Horta, J., Loureiro, C., Ferreira, Ferreira, Ó., 2015. Retrieval of nearshore bathymetry from Landsat 8 images: A tool for coastal monitoring in shallow waters. Remote Sens. Environ. 159, 102–116. https://doi.org/http://dx.doi.org/10.1016/j.rse.2014.12.004

Palanques, A., Grimalt, J., Belzunces, M., Estrada, F., Puig, P., Guillén, J., 2014. Massive accumulation of highly polluted sedimentary deposits by river damming. Sci. Total Environ. 497–498, 369–381. https://doi.org/10.1016/j.scitotenv.2014.07.091

Palmer, S.C.J., Kutser, T., Hunter, P.D., 2015. Remote sensing of inland waters: Challenges, progress and future directions. Remote Sens. Environ. 157, 1–8. https://doi.org/10.1016/j.rse.2014.09.021

Papa, F., Prigent, C., Aires, F., Jimenez, C., Rossow, W.B., Matthews, E., 2010. Interannual variability of surface water extent at the global scale, 1993-2004. J. Geophys. Res. Atmos. 115, 1–17. https://doi.org/10.1029/2009JD012674

Pekel, J.-F., Cottam, A., Gorelick, N., Belward, A.S., 2016. High-resolution mapping of global

surface water and its long-term changes. Nature 540, 418–422. https://doi.org/10.1038/nature20584

Pekel, J.-F., Vancutsem, C., Bastin, L., Clerici, M., Vanbogaert, E., Bartholomé, E., Defourny, P., 2014. A near real-time water surface detection method based on HSV transformation of MODIS multi-spectral time series data. Remote Sens. Environ. 140, 704–716. https://doi.org/10.1016/j.rse.2013.10.008

Penatti Costa, N., Ribeiro de Almeida, T.I., Guimaraes Ferreira, L., Arantes, A.E., Coe, M.T., 2015. Satellite-based hydrological dynamics of the world's largest continuous wetland. Remote Sens. Environ. 170, 1–13. https://doi.org/10.1016/j.rse.2015.08.031

Peng, D., Guo, S., Liu, P., Liu, T., 2006. Reservoir Storage Curve Estimation Based on Remote Sensing Data. J. Hydrol. Eng. 11, 165–172. https://doi.org/10.1061/(ASCE)1084-0699(2006)11:2(165)

Peter, S.J., de Araújo, J.C., Araújo, N. a. M.M., Herrmann, H.J., 2014. Flood avalanches in a semiarid basin with a dense reservoir network. J. Hydrol. 512, 408–420. https://doi.org/10.1016/j.jhydrol.2014.03.001

Philpot, W.D., 1989. Bathymetric mapping with passive multispectral imagery. Appl. Opt. 28, 1569–1578. https://doi.org/10.1364/AO.28.001569

Pope, K.O., Rejmankova, E., Paris, J.F., Woodruff, R., 1997. Detecting Seasonal Flooding Cycle of the Yucatan Peninsula with SIR-C Polarmetric Radar Imagery. Remote Sens. Environ. 59, 157–166.

Pope, K.O., Rejmankova, E., Paris, J.F., Woodruff, R., 1997. Detecting seasonal flooding cycles in marshes of the Yucatan Peninsula with SIR-C polarimetric radar imagery. Remote Sens. Environ. 59, 157–166. https://doi.org/10.1016/S0034-4257(96)00151-4

Pope, K.O., Sheffner, E.J., Linthicum, K.J., Bailey, C.L., Logan, T.M., Kasischke, E.S., Birney, K., Njogu, A.R., Roberts, C.R., 1992. Identification of central Kenyan Rift Valley Fever virus vector habitats with landsat TM and evaluation of their flooding status with airborne imaging radar. Remote Sens. Environ. 40, 185–196. https://doi.org/https://doi.org/10.1016/0034-4257(92)90002-2

Postel, S.L., 2000. Entering an Era of Water Scarcity : The Challenges Ahead. Ecol. Appl. 10, 941–948.

Prigent, C., Papa, F., Aires, F., Rossow, W.B., Matthews, E., 2007. Global inundation dynamics inferred from multiple satellite observations, 1993-2000. J. Geophys. Res. Atmos. 112, 1993–2000. https://doi.org/10.1029/2006JD007847

Proctor, C., He, Y., Robinson, V., 2013. Texture augmented detection of macrophyte species using decision trees. ISPRS J. Photogramm. Remote Sens. 80, 10–20.

Pulvirenti, L., Chini, M., Pierdicca, N., Guerriero, L., Ferrazzoli, P., 2011. Flood monitoring using multi-temporal COSMO-SkyMed data: Image segmentation and signature interpretation. Remote Sens. Environ. 115, 990–1002. https://doi.org/10.1016/j.rse.2010.12.002

Pulvirenti, L., Marzano, F.S., Pierdicca, N., Mori, S., Chini, M., 2014. Discrimination of Water

Surfaces, Heavy Rainfall, and Wet Snow Using COSMO-SkyMed Observations of Severe Weather Events. IEEE Trans. Geosci. Remote Sens. 52, 858–869. https://doi.org/10.1109/TGRS.2013.2244606

Pulvirenti, L., Pierdicca, N., Chini, M., Guerriero, L., 2013. Monitoring flood evolution in vegetated areas using cosmo-skymed data: The tuscany 2009 case study. IEEE J. Sel. Top. Appl. Earth Obs. Remote Sens. 6, 1807–1816. https://doi.org/10.1109/JSTARS.2012.2219509

Ramsey, E.W., 1995. Monitoring flooding in coastal wetlands by using radar imagery and ground-based measurements. Int. J. Remote Sens. 16, 2495–2502. https://doi.org/10.1080/01431169508954571

Ran, L., Lu, X.X., 2012. Delineation of reservoirs using remote sensing and their storage estimate: An example of the Yellow River basin, China. Hydrol. Process. 26, 1215–1229. https://doi.org/10.1002/hyp.8224

Refice, A., Capolongo, D., Pasquariello, G., Daaddabbo, A., Bovenga, F., Nutricato, R., Lovergine, F.P., Pietranera, L., 2014. SAR and InSAR for flood monitoring: Examples with COSMO-SkyMed data. IEEE J. Sel. Top. Appl. Earth Obs. Remote Sens. 7, 2711–2722. https://doi.org/10.1109/JSTARS.2014.2305165

Reichert, K., Nieto, J.C., Dittmer, J., 1998. WaMoS II:an operational wave monitoring system., in: Proceedings of the Oceanology'98 Conference. Brighton, England, England, pp. 455–462.

Richards, J.A., Woodgate, P.W., Skidmore, A.K., 1987. An explanation of enhanced radar backscattering from flooded forests. Int. J. Remote Sens. 8, 1093–1100. https://doi.org/10.1080/01431168708954756

Roberts, D.A., Gardner, M., Church, R., Ustin, S., Scheer, G., Green, R.O., 1998. Mapping chaparral in the Santa Monica Mountains using multiple endmember spectral mixture models. Remote Sens. Environ. 65, 267–279. https://doi.org/10.1016/S0034-4257(98)00037-6

Rodell, M., Houser, P.R., Jambor, U., Gottschalck, J., Mitchell, K., Meng, C.-J., Arsenault, K., Cosgrove, B., Radakovich, J., Bosilovich, M., Entin, J.K., Walker, J.P., Lohmann, D., Toll, D., 2004. The Global Land Data Assimilation System. Bull. Am. Meteorol. Soc. 85, 381–394. https://doi.org/10.1175/BAMS-85-3-381

Rodríguez, E., 2016. Surface Water and Ocean Topography Mission (SWOT§) Project Science Requirements Document.

Rodriguez, E., Martin, J.M., 1992. Theory and design of interferometric synthetic aperture radars. IEE Proc. F Radar Signal Process. 139, 147. https://doi.org/10.1049/ip-f-2.1992.0018

Rodriguez, E., Morris, C.S., Belz, J.E., Rodríguez, E., Morris, C.S., Belz, J.E., 2006. A global assessment of the SRTM performance. Photogramm. Eng. Remote Sensing 72, 249–260. https://doi.org/10.14358/PERS.72.3.249

Romeiser, R., Hirsch, O., Gade, M., 2000. Remote sensing of surface currents and bathymetric

features in the German Bight by along-track SAR interferometry, in: Proceedings of IGARSS 2000. IEEE, Honolulu, pp. 1081–1083.

Rosen, P.A., Hensley, S., Joughin, I.R., Li, F.K., MADSEN, S.N., Rodriguez, E.E., Goldstein, R.M., 2000. Synthetic aperture radar interferometry. Proc. IEEE 88, 333–382. https://doi.org/10.1109/5.838084

Rosenqvist, A., Forsberg, B.R., Pimentel, T., Rauste, Y.A., Richey, J.E., 2002. The use of speceborne radar data to model inundation patterns and trace gas emissions in the central amazpn floodplain. Int. J. Remote Sens. 23, 1303–1328.

Roshier, D.A., Robertson, A.I., Kingsford, R.T., 2002. Responses of waterbirds to flooding in an arid region of Australia and implications for conservation. Biol. Conserv. 106, 399–411. https://doi.org/10.1016/S0006-3207(01)00268-3

Rossi, C., Erten, E., 2015. Paddy-Rice Monitoring Using TanDEM-X. IEEE Trans. Geosci. Remote Sens. 53, 900–910.

Rossi, C., Minet, C., Fritz, T., Eineder, M., Bamler, R., 2016. Temporal monitoring of subglacial volcanoes with TanDEM-X - Application to the 2014-2015 eruption within the Bárdarbunga volcanic system, Iceland. Remote Sens. Environ. 181, 186–197. https://doi.org/10.1016/j.rse.2016.04.003

Sahoo, A.K., Pan, M., Troy, T.J., Vinukollu, R.K., Sheffield, J., Wood, E.F., 2011. Reconciling the global terrestrial water budget using satellite remote sensing. Remote Sens. Environ. 115, 1850–1865. https://doi.org/http://dx.doi.org/10.1016/j.rse.2011.03.009

Sandidge, J.C., Holyer, R.J., 1998. Coastal bathymetry from hyperspectral observations of water radiance. Remote Sens. Environ. 65, 341–352. https://doi.org/10.1016/S0034-4257(98)00043-1

Santoro, M., Wegmüller, U., Lamarche, C., Bontemps, S., Defourny, P., Arino, O., 2015. Strengths and weaknesses of multi-year Envisat ASAR backscatter measurements to map permanent open water bodies at global scale. Remote Sens. Environ. 171, 185–201. https://doi.org/10.1016/j.rse.2015.10.031

Sarker, M.L.R., Nichol, J., Iz, H.B., Ahmad, B.B., Rahman, A.A., 2013. Forest Biomass Estimation Using Texture Measurements of High-Resolution Dual-Polarization C-Band SAR Data. IEEE Trans. Geosci. Remote Sens. 51, 3371–3384. https://doi.org/10.1109/TGRS.2012.2219872

Scheffler, D., Hollstein, A., Diedrich, H., Segl, K., Hostert, P., 2017. AROSICS: An Automated and Robust Open-Source Image Co-Registration Software for Multi-Sensor Satellite Data. Remote Sens. 9.

Schilling, M.F., Watkins, A.E., Watkins, W., 2002. Is Human Height Bimodal? Am. Stat. 56, 223–229. https://doi.org/10.1198/00031300265

Schlaffer, S., Chini, M., Giustarini, L., Matgen, P., 2017. Probabilistic mapping of flood-induced backscatter changes in SAR time series. Int. J. Appl. Earth Obs. Geoinf. 56, 77–87. https://doi.org/10.1016/j.jag.2016.12.003

Schlaffer, S., Matgen, P., Hollaus, M., Wagner, W., 2015. Flood detection from multi-temporal

SAR data using harmonic analysis and change detection. Int. J. Appl. Earth Obs. Geoinf. 38, 15–24. https://doi.org/10.1016/j.jag.2014.12.001

Schlund, M., von Poncet, F., Hoekman, D.H., Kuntz, S., Schmullius, C., 2013. Importance of bistatic SAR features from TanDEM-X for forest mapping and monitoring. Remote Sens. Environ. 151, 16–26. https://doi.org/10.1016/j.rse.2013.08.024

Shi, C., Wang, L., 2014. Incorporating spatial information in spectral unmixing: A review. Remote Sens. Environ. 149, 70–87. https://doi.org/10.1016/j.rse.2014.03.034

Shoshany, M., Svoray, T., Curran, P.J., Foody, G.M., Perevolotsky, A., 2000. The relationship between ERS-2 SAR backscatter and soil moisture: generalization from a humid to semi-arid transect. Int. J. Remote Sens. 21, 2337–2343. https://doi.org/10.1080/01431160050029620

Shuchman, R.A., Lyzenga, D.R., Meadows, G.A., 1985. Synthetic aperture radar imaging of ocean-bottom topography via tidal-current interactions: theory and observations. Int. J. Remote Sens. 6, 1179–1200. https://doi.org/10.1080/01431168508948271

Silva, T.S.F., Costa, M.P.F., Melack, J.M., Novo, E.L.M., 2008. Remote sensing of aquatic vegetation: theory and applications. EnvironMonit Assess 140, 131–145.

Singh, A., Seitz, F., Schwatke, C., 2012. Inter-annual water storage changes in the Aral Sea from multi-mission satellite altimetry, optical remote sensing, and GRACE satellite gravimetry. Remote Sens. Environ. 123, 187–195. https://doi.org/10.1016/j.rse.2012.01.001

SIRH/Ce, 2015. Electronic atlas of water resources of Ceará (Atlas Eletrônico dos Recursos Hídricos do Ceará) [WWW Document]. URL http://atlas.srh.ce.gov.br/

Small, D., 1998. Generation of Digital Elevation Models through Spaceborne SAR Interferometry. Dep. Geogr. University of Zurich.

Smith, L.C., 1997. satellite remote sensing of river inundation area,stage and discharge:a review. Hydrol. Process. 11, 1427–1439.

Smith, L.C., Pavelsky, T.M., 2009. Remote sensing of volumetric storage changes in lakes. EARTH Surf. Process. LANDFORMS 34, 1353–1358. https://doi.org/10.1002/esp

Smith, S. V., Renwick, W.H., Bartley, J.D., Buddemeier, R.W., 2002. Distribution and significance of small, artificial water bodies across the United States landscape. Sci. Total Environ. 299, 21–36. https://doi.org/10.1016/S0048-9697(02)00222-X

Sneed, W.A., Hamilton, G.S., 2007. Evolution of melt pond volume on the surface of the Greenland Ice Sheet. Geophys. Res. Lett. 34, 4–7. https://doi.org/10.1029/2006GL028697

Song, C., Huang, B., Ke, L., 2013. Modeling and analysis of lake water storage changes on the Tibetan Plateau using multi-mission satellite data. Remote Sens. Environ. 135, 25–35. https://doi.org/10.1016/j.rse.2013.03.013

Song, C., Huang, B., Ke, L., Richards, K.S., 2014. Remote sensing of alpine lake water environment changes on the Tibetan Plateau and surroundings: A review. ISPRS J. Photogramm. Remote Sens. 92, 26–37. https://doi.org/10.1016/j.isprsjprs.2014.03.001

Stasolla, M., Gamba, P., 2008. Spatial indexes for the extraction of formal and informal human

settlements from high-resolution SAR images. IEEE J. Sel. Top. Appl. Earth Obs. Remote Sens. 1, 98–106. https://doi.org/10.1109/JSTARS.2008.921099

Sugunan, V.V., 1997. Fiseheries Management of small water bodies in seven coutries in Africa, Asia and Latin America. Rome.

Szekielda, K.-H., 1988. Satellite monitoring of the earth. Wiley.

TanDEM-X ground segment, 2013. TanDEM-X Products Specification Document [WWW Document]. URL https://tandemx-science.dlr.de/pdfs/TD-GS-PS-0021_DEM-Product-Specification_v3.0.pdf

TanDEM-X ground segment, 2012. TanDEM-X Experimental Product Description [WWW Document]. URL https://tandemx-science.dlr.de/pdfs/TD-GS-PS-3028_TanDEM-X-Experimental-Product-Description_1.2.pdf

TanDEM-X payload ground segment, 2012. CoSSC Generation and Interferometric Considerations [WWW Document]. URL https://tandemx-science.dlr.de/pdfs/TD-PGS-TN-3129_CoSSCGenerationInterferometricConsiderations_1.0.pdf

Thomas, A.C., Reager, J.T., Famiglietti, J.S., Rodell, M., 2014. A GRACE-based water storage deficit approach for hydrological drought characterization. Geophys. Res. Lett. 41, 1537–1545. https://doi.org/10.1002/2014GL059323

Thomas, R.F., Kingsford, R.T., Lu, Y., Cox, S.J., Sims, N.C., Hunter, S.J., 2015. Mapping inundation in the heterogeneous floodplain wetlands of the Macquarie Marshes, using Landsat Thematic Mapper. J. Hydrol. 524, 194–213. https://doi.org/10.1016/j.jhydrol.2015.02.029

Toeyrae, J., Pietroniro, A., Martz, L.W., 2001. Multisensor hydrologic assessment of a freshwater wetland. Remote Sens. Environ. 75, 162–173. https://doi.org/10.1016/S0034-4257(00)00164-4

Townsend, P.A., 2001. Mapping Seasonal Flooding in Forested Wetlands Using Multi-Temporal Radarsat SAR. Photogramm. Eng. Remote Sens. 67, 857–864.

Tranvik, L.J., Downing, J.A., Cotner, J.B., Loiselle, S.A., Striegl, R.G., Ballatore, T.J., Dillon, P., Finlay, K., Fortino, K., Knoll, L.B., Kortelainen, P.L., Kutser, T., Larsen, S., Laurion, I., Leech, D.M., McCallister, S.L., McKnight, D.M., Melack, J.M., Overholt, E., Porter, J.A., Prairie, Y., Renwick, W.H., Roland, F., Sherman, B.S., Schindler, D.W., Sobek, S., Tremblay, A., Vanni, M.J., Verschoor, A.M., von Wachenfeldt, E., Weyhenmeyer, G.A., 2009. Lakes and reservoirs as regulators of carbon cycling and climate. Limnol. Oceanogr. 54, 2298–2314. https://doi.org/10.4319/lo.2009.54.6_part_2.2298

Troch, P.A., 1996. Retrieving soil moisture over bare soil from ERS 1 synthetic aperture radar data: Sensitivity analysis based on a theoretical surface scattering model and field data. Water Resour. Res. 32, 653–661.

Tropical Rainfall Measuring Mission (TRMM), 2018. TRMM (TMPA/3B43) Rainfall Estimate

L3 1 month 0.25 degree x 0.25 degree V7, Greenbelt, MD, Goddard Earth Sciences Data and Information Services Center (GES DISC) [WWW Document]. URL https://disc.gsfc.nasa.gov/datacollection/TRMM_3B43_7.html (accessed 2.2.18).

Tulbure, M.G., Broich, M., 2013. Spatiotemporal dynamic of surface water bodies using Landsat time-series data from 1999 to 2011. ISPRS J. Photogramm. Remote Sens. 79, 44–52. https://doi.org/10.1016/j.isprsjprs.2013.01.010

Uhlmann, S., Kiranyaz, S., 2014. Classification of dual- and single polarized SAR images by incorporating visual features. ISPRS J. Photogramm. Remote Sens. 90, 10–22. https://doi.org/10.1016/j.isprsjprs.2014.01.005

Ulaby, F.T., Long, D.G., 2014. Miacrowave Radar and Radiometric Remote sensing. The Universisty of Michigan press, Ann Arbor.

Ustin, S.L., 2004. Remote sensing for natural resource management and environmental monitoring, in: Ustin, S.L. (Ed.), Manual of Remote Sensning. merican Society for Photogrammetry and Remote Sensing, New Jersey, p. 361.

Valenzuela, G.R., 1978. Theories for the interaction of electromagnetic and oceanic waves: A review. Boundary-Layer Meteorol. 13, 61–85.

Van Dijk, a. I.J.M., Renzullo, L.J., 2011. Water resource monitoring systems and the role of satellite observations. Hydrol. Earth Syst. Sci. 15, 39–55. https://doi.org/10.5194/hess-15-39-2011

Verpoorter, C., Kutser, T., Seekell, D.A., Tranvik, L.J., 2014. A global inventory of lakes based on high-resolution satellite imagery. Geophys. Res. Lett. 41, 6396–6402. https://doi.org/10.1002/2014GL060641

Vignudelli, S., Cipollini, P., Gommenginger, C., Snaith, H., Coelho, H., Fernandes, J., Gomez-enri, J., Martin-puig, C., Woodworth, P., Dinardo, S., 2009. The COASTALT Project : Towards an Operational use of Satellite Altimetry in the Coastal Zone 0–5.

Vogelzang, J., Wensink, G.J., De Loor, G.P., Peters, H.C., Pouwels, H., 1992. Sea bottom topography with X-band SLAR: the relation between radar imagery and bathymetry. Int. J. Remote Sens. 13, 1943–1958. https://doi.org/10.1080/01431169208904242

Voormansik, K., Praks, J., Antropov, O., Jagomagi, J., Zalite, K., 2014. Flood mapping with terraSAR-X in forested regions in estonia. IEEE J. Sel. Top. Appl. Earth Obs. Remote Sens. 7, 562–577. https://doi.org/10.1109/JSTARS.2013.2283340

Vörösmarty, C.J., Sahagian, D., 2000. Anthropogenic Disturbance of the Terrestrial Water Cycle. Bioscience 50, 753. https://doi.org/10.1641/0006-3568(2000)050[0753:ADOTTW]2.0.CO;2

Wang, L., Dronova, I., Gong∗, P., Yang, W., Li, Y., Liu, Q., 2012. A new time series vegetation–water index of phenological–hydrological trait across species and functional types for Poyang Lake wetland ecosystem. Remote Sens. Environ. 125, 49–63.

Wang, Y., Hess, L.L., Filoso, S., Melack, J.M., 1995. Understanding the radar backscattering from flooded and nonflooded Amazonian forests: Results from canopy backscatter modeling. Remote Sens. Environ. 54, 324–332.

https://doi.org/10.1016/0034-4257(95)00140-9

Ward, D.P., Petty, a., Setterfield, S. a., Douglas, M.M., Ferdinands, K., Hamilton, S.K., Phinn, S., 2014. Floodplain inundation and vegetation dynamics in the Alligator Rivers region (Kakadu) of northern Australia assessed using optical and radar remote sensing. Remote Sens. Environ. 147, 43–55. https://doi.org/10.1016/j.rse.2014.02.009

Warnken, K., Santschi, P., 2004. Biogeochemical behavior of organic carbon in the Trinity River downstream of a large reservoir lake in Texas, USA. Sci. Total Environ. 329, 131–44. https://doi.org/10.1016/j.scitotenv.2004.02.017

Wdowinski, S., Kim, S.-W., Amelung, F., Dixon, T.H., Miralles-Wilhelm, F., Sonenshein, R., 2008. Space-based detection of wetlands' surface water level changes from L-band SAR interferometry. Remote Sens. Environ. 112, 681–696. https://doi.org/10.1016/j.rse.2007.06.008

Wechsler, S., 2006. Uncertainties associated with digital elevation models for hydrologic applications: a review. Hydrol. Earth Syst. Sci. Discuss. 3, 2343–2384. https://doi.org/10.5194/hessd-3-2343-2006

Wedler, E., Kessler, R., 1981. Interpretation ofvegetative cover in wetlands using four- channel SAR imagery., in: Technical Papers of the American Society of Photoqrammetry, ASP-ACSM Convention. Washington, D.C, D.C, pp. 111–124.

Wegmüller, U., Santoro, M., Werner, C., Strozzi, T., Wiesmann, A., Lengert, W., 2009. DEM generation using ERS–ENVISAT interferometry. J. Appl. Geophys. 69, 51–58. https://doi.org/10.1016/j.jappgeo.2009.04.002

Weichelt, H., Rosso, P., Marx, A., Reigber, S., Douglass, K., Heynen, M., 2014. The RapidEye Red Edge Band.

Wendleder, A., Wessel, B., Roth, A., Breunig, M., Martin, K., Wagenbrenner, S., 2013. TanDEM-X water indication mask: Generation and first evaluation results. IEEE J. Sel. Top. Appl. Earth Obs. Remote Sens. 6, 171–179. https://doi.org/10.1109/JSTARS.2012.2210999

Werner, C., Wegmüller, U., Strozzi, T., Wiesmann, A., 2000. Gamma SAR and Interferometric Processing Software, in: Proceedings of ERS-ENVISAT Symposium. Gothenburg, Sweden.

Wessel, B., Huber, M., Wohlfart, C., Marschalk, U., Kosmann, D., Roth, A., 2018. Accuracy assessment of the global TanDEM-X Digital Elevation Model with GPS data. ISPRS J. Photogramm. Remote Sens. 139, 171–182. https://doi.org/10.1016/j.isprsjprs.2018.02.017

Westerhoff, R.S., Kleuskens, M.P.H., Winsemius, H.C., Huizinga, H.J., Brakenridge, G.R., Bishop, C., 2013. Automated global water mapping based on wide-swath orbital synthetic-aperture radar. Hydrol. Earth Syst. Sci. 17, 651–663. https://doi.org/10.5194/hess-17-651-2013

Williamson, A.G., Arnold, N.S., Banwell, A.F., Willis, I.C., 2017. A Fully Automated Supraglacial lake area and volume Tracking ("FAST") algorithm: Development and application using MODIS imagery of West Greenland. Remote Sens. Environ. 196, 113–

133. https://doi.org/10.1016/j.rse.2017.04.032

Wilusz, D.C., Zaitchik, B.F., Anderson, M.C., Hain, C.R., Yilmaz, M.T., Mladenova, I.E., 2017. Monthly flooded area classification using low resolution SAR imagery in the Sudd wetland from 2007 to 2011. Remote Sens. Environ. 194, 205–218. https://doi.org/10.1016/j.rse.2017.03.005

Wolski, P., Murray-hudson, M., Thito, K., Cassidy, L., 2017. Keeping it simple : Monitoring flood extent in large data-poor wetlands using MODIS SWIR data. Int. J. Appl. Earth Obs. Geoinf. 57, 224–234. https://doi.org/10.1016/j.jag.2017.01.005

Xie, C., Xu, J., Shao, Y., Cui, B., Goel, K., Zhang, Y., Yuan, M., 2015. Long term detection of water depth changes of coastal wetlands in the Yellow River Delta based on distributed scatterer interferometry. Remote Sens. Environ. 164, 238–253. https://doi.org/http://dx.doi.org/10.1016/j.rse.2015.04.010

Xu, H., 2006. Modification of normalised difference water index (NDWI) to enhance open water features in remotely sensed imagery. Int. J. Remote Sens. 27, 3025–3033. https://doi.org/10.1080/01431160600589179

Yoon, G.-W., Kim, S.-W., Lee, Y.-W., Won, J.-S., 2013. Measurement of the water level in reservoirs from TerraSAR-X SAR interferometry and amplitude images. Remote Sens. Lett. 4, 446–454. https://doi.org/10.1080/2150704X.2012.747708

Yuan, T., Lee, H., Jung, H.C., Aierken, A., Beighley, E., Alsdorf, D.E., Tshimanga, R.M., Kim, D., 2017. Absolute water storages in the Congo River floodplains from integration of InSAR and satellite radar altimetry. Remote Sens. Environ. 201, 57–72. https://doi.org/10.1016/j.rse.2017.09.003

Zalite, K., Voormansik, K., Olesk, A., Noorma, M., Reinart, A., 2013. Effects of Inundated Vegetation on X-Band HH-VV Backscatter and Phase Difference. IEEE J. Sel. Top. Appl. Earth Obs. Remote Sens. 7, 1402–1406. https://doi.org/10.1109/JSTARS.2013.2279552

Zhang, C., 2015. Applying data fusion techniques for benthic habitat mapping and monitoring in a coral reef ecosystem. ISPRS J. Photogramm. Remote Sens. 104, 213–223. https://doi.org/10.1016/j.isprsjprs.2014.06.005

Zhang, J., Xu, K., Yang, Y., Qi, L., Hayashi, S., Watanabe, M., 2006. Measuring water storage fluctuations in Lake Dongting, China, by Topex/Poseidon satellite altimetry. Environ. Monit. Assess. 115, 23–37. https://doi.org/10.1007/s10661-006-5233-9

Zhang, S., Foerster, S., Medeiros, P., de Araújo, J.C., Motagh, M., Waske, B., 2016. Bathymetric survey of water reservoirs in north-eastern Brazil based on TanDEM-X satellite data. Sci. Total Environ. 571, 575–593. https://doi.org/10.1016/j.scitotenv.2016.07.024

Zhang, S., Foerster, S., Medeiros, P., de Araújo, J.C., Waske, B., 2018. Effective water surface mapping in macrophyte-covered reservoirs in NE Brazil based on TerraSAR-X time series. Int. J. Appl. Earth Obs. Geoinf. 69, 41–55. https://doi.org/https://doi.org/10.1016/j.jag.2018.02.014

Zhang, S., Gao, H., Naz, B.S., 2014. Monitoring reservoir storage in South Asia from

multisatellite remote sensing. Water Resour. Res. 50, 8927– 8943. https://doi.org/:10.1002/2014WR015829

Zhao, L., Yang, J., Li, P., Zhang, L., 2014. Seasonal inundation monitoring and vegetation pattern mapping of the Erguna floodplain by means of a RADARSAT-2 fully polarimetric time series. Remote Sens. Environ. 152, 426–440. https://doi.org/10.1016/j.rse.2014.06.026

Zhao, X., Stein, A., Chen, X.L., 2011. Monitoring the dynamics of wetland inundation by random sets on multi-temporal images. Remote Sens. Environ. 115, 2390–2401. https://doi.org/10.1016/j.rse.2011.05.002

Zhao, X., Stein, A., Zhang, X., Feng, L., Chen, X., 2014. Variation analysis of lake extension in space and time from MODIS images using random sets. Int. J. Appl. Earth Obs. Geoinf. 30, 86–97. https://doi.org/10.1016/j.jag.2014.01.003

Zhu, Z., Woodcock, C.E., 2012. Object-based cloud and cloud shadow detection in Landsat imagery. Remote Sens. Environ. 118, 83–94. https://doi.org/10.1016/j.rse.2011.10.028

Zwally, H.J., Schutz, B., Abdalati, W., Abshire, J., Bentley, C., Brenner, A., Bufton, J., Dezio, J., Hancock, D., Harding, D., Herring, T., Minster, B., Quinn, K., Palm, S., Spinhirne, J., Thomas, R., 2002. ICESat's laser measurements of polar ice, atmosphere, ocean, and land. J. Geodyn. 34, 405–445. https://doi.org/10.1016/S0264-3707(02)00042-X

References

Acknowledgement

Writing at the point of finishing my 4.5 years' study in GFZ Potsdam and nearly 6 years in Germany, I deeply appreciate all the people who have supported, helped, and companied me during this very long journey.

My doctoral study in Germany has been supported by China Scholarships Council (CSC 201204910215). So I would like to thank Prof. Hucai Zhang for his support during my application for the scholarship.

Saskia Foerster is my primary supervisor based in GFZ. During my PhD study, Saskia is the first one I went whenever I needed help. She has always been very supportive. She impressed me with her research attitude and hardworking spirit. Meanwhile, I also appreciate that she has left me freedom and space to investigate and experiment by myself, and tolerate the differences between us. I would like to thank her for her trust, patience, and endeavor for support in any sense she thinks necessary. I genuinely thank her for her supervision, support and encouragement.

I appreciate al lot the efficient and insightful supervision I have received from Prof. Bjoern Waske. I have greatly benefited from his academic advice and suggestions and his excellent scientific writing skills. His continuous help and support ensured the completion of my PhD and greatly encouraged my own development in science. From my standpoint in this relation, I could not expect more than what he offered.

Particular thanks are given to Professor Axel Bronstert and his team for very constructive discussions and appreciation of my work, and that has motivated and encouraged me a lot. I would like to than Jose Carlos, Pedro, for their very instant and efficient support to our field work in any time need. Specific thanks go to Goerge, Thiago, Tatiana, Christine, Leonardo, Eder and other many Brazilian colleagues for their support during our field campaigns in Madalena, Ceará. Their friendly company and thorough support in the tough work environments have made the field campaigns one of the most memorial experiences during my

study.

In my PhD study, I also received a lot of help from my colleagues. Arlena has offered me her very considerate help and support in the initial stage of my stay in Potsdam. I thank Daniel Scheffler and Robert Behling for sharing their codes for data preprocessing which have saved a lot time and efforts for me. I am very grateful that I am a member of SAR round table in GFZ, as I have benefited a lot from the interactive discussions with them. Genuine gratitude is paid to the round table members including but not limited to Iris, Julia, Christin, Sabrina, Henriette, Jackie and Felix. I would like to thank Sophia, Iris, Katharina, Claudia and Katrin for the daily communication and company during the lunch breaks, and particular Sophia for in the most of the time during my PhD. Thanks also go to Ola, Robert Milewski, and Darya for their constructive help to my study in Potsdam. All you above are not only colleagues but also friends for me, another precious achievement obtained during my study. My sincere acknowledgments go to our technician Sylvia Magnussen. Thanks to her, I have never bothered with or delayed by any computer related problem. Meanwhile, I always feel welcome with her. I would like to pay particular thanks to Mr Knut Guenter from Section 5.4 in GFZ for instructing me to use TOPCON DGPS and post processing of the data.

My gratitude also goes to Yuanying, Bo, Kanayim, Sinem, Shaoyang, Yaling, Zhihua, Salomon, Bohao, Jordan, Marc, Junzhe, Feifei and other friends for keep me in company and making my life in Germany colorful. In this regard, I would sincerely thank Gregori Locket, Hanna Haedke, Maggie, Martin Schuettig, and Stefan Schimpf and Wei Ding, Shuxin, Lei, Bingfu for their care and support in the very early stage of my stay in Germany. You made my landing in Germany very pleasant.

Finally, I thank my family for all their understanding, encouragement and support throughout all my time. They are the very source of all the courage and power I have gained to overcome any obstacles I have encountered in my life.